



HAL
open science

Plasmonic cavities and optical nanosources

Stephane Derom

► **To cite this version:**

Stephane Derom. Plasmonic cavities and optical nanosources. Other [cond-mat.other]. Université de Bourgogne, 2013. English. NNT: 2013DIJOS060 . tel-01005260

HAL Id: tel-01005260

<https://theses.hal.science/tel-01005260>

Submitted on 12 Jun 2014

HAL is a multi-disciplinary open access archive for the deposit and dissemination of scientific research documents, whether they are published or not. The documents may come from teaching and research institutions in France or abroad, or from public or private research centers.

L'archive ouverte pluridisciplinaire **HAL**, est destinée au dépôt et à la diffusion de documents scientifiques de niveau recherche, publiés ou non, émanant des établissements d'enseignement et de recherche français ou étrangers, des laboratoires publics ou privés.

UNIVERSITÉ DE BOURGOGNE
FACULTÉ DES SCIENCES

Laboratoire Interdisciplinaire Carnot de Bourgogne
Département Nanosciences

**PLASMONIC CAVITIES AND OPTICAL
NANOSOURCES**

Thèse présentée à l'Université de Bourgogne pour obtenir
le grade de Docteur (Mention Physique)

par

Stéphane Derom

Soutenue le 17 Décembre 2013

à L'Amphithéâtre ESIREM à 14h00

devant la commission d'examen composée de :

BONOD	N.	Chargé de Recherche, CNRS, Univ. d'Aix Marseille	Rapporteur
BIGOT	L.	Chargé de Recherche, CNRS, Univ. de Lille 1	Rapporteur
HERMIER	J.-P.	Professeur, Univ. de Versailles	Examineur
SAUVAN	C.	Chargé de Recherche, CNRS, Institut d'optique	Examineur
SAVIOT	L.	Directeur de Recherche, CNRS, Univ. de Bourgogne	Examineur
COLAS DES FRANCS	G.	Professeur, Univ. de Bourgogne	Directeur de thèse

Plasmonic cavities and optical nanosources

Abstract: Optical microcavities exhibit high resonance quality, so that, they are of key interest for the design of low-threshold lasers or for achieving strong coupling regime. But, such systems support modes whose the volume remain diffraction limited.

In this manuscript, we are interested in their plasmonic counterparts because they support confined modes at the subwavelength scale. First, we study an in-plane plasmonic cavity which is the transposition of 1D optical cavity to surface wave. We characterize the cavity by measuring the fluorescence lifetime of dye molecules deposited inside.

Then, we are interested in 3-dimension mode confinement achieved by spherical metal nanoparticles. We discuss on the definition of the mode volume used in cavity quantum electrodynamic and based on the calculation of energy confinement around the particle.

We also simulate the fluorescence enhancement of rare-earth ions embedded inside core-shell plasmonic particles.

Finally, we disturb the photodynamic emission of a single-photon source by putting the extremity of a plasmonic tip nearby the emitter.

Keywords: Plasmonic cavity, Localized surface plasmon, spontaneous emission, time-resolved spectroscopy

Cavités plasmoniques et nanosources optiques

Résumé: Les micro-cavités optiques présentent de hauts facteurs de qualité, c'est pourquoi ces systèmes sont d'un grand intérêt pour la conception de lasers à bas seuil, ou encore, pour l'étude du régime de couplage fort. En revanche, ces systèmes sont soumis à la limite de diffraction de la lumière, et donc les modes qu'ils supportent ont une extension spatiale ne pouvant être en deçà de l'échelle de la longueur d'onde. Dans ce manuscrit de thèse, nous nous intéressons aux systèmes plasmoniques parce qu'ils supportent des modes confinés à l'échelle nanométrique.

En premier lieu, nous étudions une micro-cavité plasmonique planaire, constituée de deux miroirs plasmoniques qui piègent les ondes de surface au sein du système. Nous sondons spatialement les modes de la cavité en mesurant le temps de vie de fluorescence de molécules individuelles dispersées au sein du système.

Puis, nous nous intéressons au confinement en 3 dimensions de modes supportés par des nanoparticules métalliques sphériques. Nous discutons de la définition du volume modal basée sur le calcul du confinement d'énergie autour de la particule.

Ensuite, nous étudions l'exaltation de fluorescence d'ions de terres rares au sein d'une particule plasmonique de configuration coeur-coquille.

Enfin, nous perturbons la photodynamique d'émission d'une source de photon unique en approchant à proximité l'extrémité d'une pointe plasmonique.

Mots clés: Cavité plasmonique, plasmon de surface localisé, émission spontanée, spectroscopie résolue en temps

Remerciements

Ce travail de thèse, financé par le projet PlasTips de l'Agence Nationale de la Recherche, a été réalisé au sein du Département Nanosciences du Laboratoire Interdisciplinaire Carnot de Bourgogne de l'Université de Bourgogne.

Ces trois dernières années d'investissement personnel n'auraient jamais pu aboutir sans l'aide et la présence des personnes qui m'ont accueilli au sein de l'équipe Optique Submicronique et Nano-Capteurs de Dijon. Ainsi, je tiens à formuler mes sentiments les plus amicaux envers celles et ceux que j'ai rencontrés durant ma thèse.

En premier lieu, je tiens à exprimer mes remerciements et ma reconnaissance envers mon directeur de thèse, Gérard Colas des Francs, pour s'être montré d'une extrême disponibilité à mon égard, et, pour l'enseignement très précieux qu'il m'a transmis. Durant cette thèse, j'ai apprécié de pouvoir bénéficier d'une certaine liberté dans mes investigations. J'ai aussi apprécié les qualités humaines de Gérard.

Je remercie Alexandre Bouhelier, qui m'a transmis le goût et l'aplomb nécessaires pour entreprendre les réalisations expérimentales. Je remercie Jean-Claude Weeber de m'avoir fait profiter de son savoir-faire en matière de nano-fabrication et de ses apports théoriques très enrichissants. Merci à Aymeric Leray pour sa participation à nos récents travaux et sa sympathie.

Mes remerciements vont également à Laurent Markey pour m'avoir fait profiter de son expérience, à Juan Arocas pour sa disponibilité et sa bonne humeur. Merci à Yvon Lacroute. Ils m'ont apporté, en plus de leur sympathie, une aide très précieuse pour la manipulation des instruments de nano-fabrication.

Je tiens à saluer chaleureusement Elly Lacroute pour son extrême disponibilité, sa sympathie et pour m'avoir aidé à me dépêtrer de tâches administratives.

Je souhaite adresser mes remerciements à Lucien Saviot, Christophe Sauvan, Jean-Pierre Hermier, Nicolas Bonod et Laurent Bigot, qui m'ont fait l'honneur d'être membres du jury de ma soutenance de thèse. Je remercie particulièrement Nicolas Bonod et Laurent Bigot, qui ont accepté d'être les rapporteurs de ce manuscrit.

Je remercie Erik Dujardin, Aurélien Drezet, Serge Huant, Christian Girard et Sviatlana Viarbitskaya, avec qui j'ai eu l'occasion d'interagir dans le cadre des réunions instructives du projet PlasTips.

Je n'oublierai pas ces moments de convivialité et d'amitié partagés avec des personnes que j'ai rencontrés au sein du laboratoire. Ces moments sont toujours

indispensables durant une thèse. Merci à Pierre Bramant, Antonin Ollagnier, Floriane Leroy, Rémi Vincent, Simon Debrand, Arnaud Stolz, Pauline Vitry, Michael G. Nielsen, Mingxia Song, Thibault Brule, Thomas Bernardin, Sébastien Reymond-Laruinaz, Ece Neslihan Aybeke, Marie-Maxime Mennemanteuil, Yacoub Ould-Agha, Brice de Fonseca, Christophe Harder, Serkan Kaya, Kamal Hammani, David Carriou, Maxime Ewald, Jean Dellinger, Karim Hassan, Arunandan Kumar et Christian Vernoux.

Je veux aussi remercier Alain Dereux, Eric Finot, Eric Lesniewska, Thierry David, Eric Bourillot, Frédéric Chaussard, Hans-Rudolf Jauslin pour leurs enseignements.

Je veux saluer le personnel de l'Atelier de Mécanique Optique et Nanosciences: Jean-Marc Müller, André Javelle et Brice Gourier; le personnel du service électronique : Bernard Sinardet et Stéphane Pernot.

Contents

Introduction	1
1 Cavity and metal enhanced fluorescence	3
1.1 Fluorescence control in optical microcavities	3
1.1.1 Purcell factor	5
1.1.2 Discussion	7
1.1.3 Coupling efficiency (β factor)	7
1.1.4 Optical microcavities	8
1.2 Metal enhanced spectroscopies	9
1.2.1 Surface plasmon polariton: description	10
1.2.2 Fluorescence near a metallic film	12
1.2.3 Surface enhanced spectroscopies	14
1.3 Conclusion	16
2 Single molecule fluorescence control in in-plane plasmonic cavity	19
2.1 Surface plasmon coupled emission near a distributed SPP Bragg reflector (DBR)	20
2.1.1 Surface plasmon coupled emission of fluorescent nanobeads	20
2.1.2 Mirror efficiency	23
2.2 In-plane SPP cavity	26
2.2.1 Decay rate and relaxation channels	26
2.2.2 Single molecule fluorescence lifetime imaging	29
2.3 Conclusion	36
3 Mie Plasmons: Modes Volume, resonance quality and Purcell factor	37
3.1 Quasi-static approximation	38
3.1.1 Dipolar mode	38
3.1.2 Multipolar modes	43
3.1.3 β -factor	47
3.2 Mie plasmon	48
3.2.1 Resonance quality	49
3.2.2 Effective volume	52
3.3 Conclusion	56
4 Luminescent doped plasmonic nanoparticles	57
4.1 Mie description of metal enhanced fluorescence	58
4.1.1 Excitation field and pumping rate	58
4.1.2 Emission rate	61
4.1.3 Fluorescence enhancement in the continuous regime	62
4.2 Effect of the particle size	64

4.2.1	Excitation and emission rate	64
4.2.2	Single molecule metal enhanced fluorescence	65
4.3	Fluorescence of doped core-shell plasmonic particles	66
4.3.1	Average enhancement factor	67
4.3.2	Rare earth doped plasmonic core shell	69
4.4	Conclusion	74
5	Single photon source in a tip-surface junction	77
5.1	Photon anti-bunching near a plasmonic nanostructure.	78
5.2	Nitrogen Vacancy color center in nanodiamonds	79
5.3	Optical addressing of individual NV centers	81
5.3.1	Experimental set-up and methods	81
5.3.2	Photodynamics of NV nanodiamonds	84
5.4	Nanodiamond NV center emission in a tip-surface junction	86
5.4.1	SNOM Tip	87
5.4.2	Tip perturbed single photon source emission	89
5.5	Conclusion	92
	Conclusion and perspectives	93
A	Appendix 1	95
A.1	Effective polarisability associated to n^{th} SPP mode	95
A.2	Effective volumes	96
	Bibliography	97

Introduction

The control of fluorescence emission has been widely studied for decades for improving Lasers and light-emitting diode (LED). Such improvement is possible by coupling emissive materials to an optical cavity. This allows to enhance the spontaneous emission as well as increase its directionality. Optical cavities confine the light thanks to mirrors. This increases the duration of interaction between the emissive materials and the optical modes since it propagates back-and-forth. Microtechnologies and nanotechnologies have paving the way for improving optical cavities for reducing lasing threshold. And, several research groups have found much wider applications. For example, an optical microcavity allows to control the photodynamic of a single photon emitter (as a dye molecule, a quantum dot or a nitrogen vacancy in nano-diamond...) which is key interest for application domains as quantum information.

The key parameters of cavities are their resonance quality and their ability to confine light (modal volume). Optical cavities typically exhibit high quality factors. Nevertheless, bulk-mode cavities are diffraction limited so that their modal volume cannot be below the wavelength scale. On the other hand, noble metal nanostructures have a weak quality factor due to their ohmic losses, but support surface plasmon that have the characteristic to be confined at the nanoscale.

In this thesis manuscript, we study the possibilities that are provided by plasmonic structures for controlling the spontaneous emission. In Chapter 1, we briefly review the key parameters depicting the cavity effects. Then, we introduce the properties of surface plasmon (SPP) supported by a flat metallic film or by metal nanoparticles. We present a brief state of the art of their applications for metal enhanced spectroscopy.

In Chapter 2, we study an in-plane plasmonic cavity that confines surface waves on a metal film (delocalized surface plasmon). We numerically and experimentally characterize the SPP mirror as well as control of spontaneous emission in a planar plasmonic cavity.

On the other hand, we study in Chapter 3 localized surface plasmon (LSP) supported by metal nanoparticles that is intrinsically a 3 dimension confined mode. We investigate the characteristics of each mode: quality resonance and effective volume. In particular, we discuss the definition of the mode volume based on energy confinement which is commonly used in cavity quantum electrodynamic (cQED).

In Chapter 4, we briefly review the mechanisms of the coupling between an emitter and a metal nanoparticle. Then, we extend our study to plasmonic core-shell particles in order to quantitatively determine the fluorescence enhancement achiev-

able by coupling emitters with LSP modes. We first consider Rhodamine 6G dye molecules coupled to a metal particle, and then, the results obtained are compared to the case of rare-earth plasmonic core-shell particles.

Finally in Chapter 5, preliminary experiments are performed for modifying the emission of a single photon emitter by using a deterministic approach: we control a plasmonic tip in order to put it nearby the emitter. In particular, we measure the photodynamics of the emitter placed in the junction between the tip-end and a glass substrate.

Cavity and metal enhanced fluorescence

Contents

1.1	Fluorescence control in optical microcavities	3
1.1.1	Purcell factor	5
1.1.2	Discussion	7
1.1.3	Coupling efficiency (β factor)	7
1.1.4	Optical microcavities	8
1.2	Metal enhanced spectroscopies	9
1.2.1	Surface plasmon polariton: description	10
1.2.2	Fluorescence near a metallic film	12
1.2.3	Surface enhanced spectroscopies	14
1.3	Conclusion	16

In this thesis, we investigate fluorescence modification and control near a plasmonic nanostructure. In addition to surface enhanced fluorescence description and measurement, we discuss of the analogy with cavity quantum electrodynamics description (Purcell factor). It is noteworthy that the original article of E. Purcell also discussed spontaneous emission near a micrometer metallic particle (see Fig. 1.1). We expect from this analogy to permit optimization of the light-matter interaction at the nanoscale. Original nanooptical devices would profit from this concept (plasmon nanolaser, nanooptical logical gates, sensing at the nanoscale,...).

In this chapter, we describe briefly the main concepts involved in the cavity-emitter coupling (section 1.1) and surface enhanced spectroscopy (section 1.2).

1.1 Fluorescence control in optical microcavities

In 1946, E. Purcell proposed to decrease the relaxation time of a nuclear magnetic moment by coupling to a resonant electric circuit (see Fig. 1.1) [Purcell 1946]. More precisely, he demonstrated that the spontaneous emission (invert of the relaxation time) is governed by the quality factor (Q) and modal volume (V) of the resonator.

The Purcell factor $F_p = \gamma/\gamma_0 \propto Q/V$ quantifies the enhancement of the spontaneous emission rate γ compared to its free space value γ_0 . Oppositely, Yablonovitch proposed in 1987 to inhibit spontaneous emission in a photonic crystal since no mode is supported in the band gap [Yablonovitch 1987]. His work was notably motivated by elimination of unwanted spontaneous emission in semiconductor lasers or solar cells. He also discussed the possibility to improve laser emission by restricting the spontaneous emission to a chosen electromagnetic mode. This has opened the way to fluorescence control in optical microcavities with applications as bio-chemical sensing, photovoltaic systems, quantum cryptography, light nanosources... (for a review, see [Benson 2006] and [Bär 2010]).

B10. Spontaneous Emission Probabilities at Radio Frequencies. E. M. PURCELL, *Harvard University*.—For nuclear magnetic moment transitions at radio frequencies the probability of spontaneous emission, computed from

$$A_\nu = (8\pi\nu^2/c^3)h\nu(8\pi^3\mu^2/3h^2) \text{ sec.}^{-1},$$

is so small that this process is not effective in bringing a spin system into thermal equilibrium with its surroundings. At 300°K, for $\nu = 10^7 \text{ sec.}^{-1}$, $\mu = 1$ nuclear magneton, the corresponding relaxation time would be 5×10^{21} seconds! However, for a system coupled to a resonant electrical circuit, the factor $8\pi\nu^2/c^3$ no longer gives correctly the number of radiation oscillators per unit volume, in unit frequency range, there being now *one* oscillator in the frequency range ν/Q associated with the circuit. The spontaneous emission probability is thereby increased, and the relaxation time reduced, by a factor $f = 3Q\lambda^3/4\pi^2V$, where V is the volume of the resonator. If a is a dimension characteristic of the circuit so that $V \sim a^3$, and if δ is the skin-depth at frequency ν , $f \sim \lambda^3/a^2\delta$. For a non-resonant circuit $f \sim \lambda^3/a^3$, and for $a < \delta$ it can be shown that $f \sim \lambda^3/a\delta^2$. If small metallic particles, of diameter 10^{-3} cm are mixed with a nuclear-magnetic medium at room temperature, spontaneous emission should establish thermal equilibrium in a time of the order of minutes, for $\nu = 10^7 \text{ sec.}^{-1}$.

Figure 1.1: Original article of E. Purcell discussing the modification of spontaneous emission of a (magnetic) dipole emitter coupled to a resonator. Reprinted excerpt with permission from E. M. Purcell, *Physical Review* **69**, p.681, 1946. Copyright (1946) by the American Physical Society.

1.1.1 Purcell factor

Here, we propose a phenomenological derivation of the spontaneous decay rate modification by the cavity in order to grasp the main features of the Purcell factor. The modification of the decay rate can be described either within classical Lorentz model of an oscillating dipole or within full quantum description with the Fermi's golden rule.

In both cases, this leads to the following expression for the rate modification in a cavity:

$$\frac{\gamma(\mathbf{r})}{\gamma_0} = \frac{\rho_i(\mathbf{r}, \omega_{em})}{\rho_i^0(\omega_{em})}, \quad (1.1)$$

where γ is the decay rate at position \mathbf{r} in the cavity and γ_0 its free space value. ω_{em} is the emission angular frequency. In this expression, $\rho(\mathbf{r}, \omega_{em})$ is the local density of states (LDOS) of the cavity at the emitter position \mathbf{r} . ρ_i is the partial LDOS (P-LDOS) according to the dipole orientation ($i = x, y, z$).

The free space LDOS is (units $\text{s} \cdot \text{m}^{-3}$)

$$\rho^0(\omega_{em}) = \frac{\omega_{em}^2}{\pi^2 c^3}, \quad (1.2)$$

when considering a specific orientation, the partial LDOS is $\rho_i^0 = \rho^0/3$. Finally, the LDOS is a key parameter to describe spontaneous emission in a cavity.

For a lossless cavity, the LDOS $\rho(\mathbf{r}, \omega)$ can be expressed as

$$\rho(\mathbf{r}, \omega) = \sum_n |\mathbf{E}_n(\mathbf{r}, \omega)|^2 \delta(\omega - \omega_n), \quad (1.3)$$

where \mathbf{E}_n is the normalized electric field related to n^{th} mode at the resonance angular frequency ω_n . For a given orientation i , the p-LDOS expresses

$$\rho_i(\mathbf{r}, \omega) = \sum_n |E_n^i(\mathbf{r}, \omega)|^2 \delta(\omega - \omega_n), \quad (1.4)$$

where E_n^i is the field i^{th} component of \mathbf{E}_n .

In the following, we phenomenologically describe the spectral and spatial shapes of the LDOS in order to propose a simple expression for the decay rate modification.

Spectral shape of the LDOS In case of a lossy cavity, the profile of the mode resonance is assumed to be Lorentzian. Therefore, the dirac function in Eq. 1.4 is replaced by the Lorentzian¹:

$$L(\omega) = \frac{1}{\pi} \frac{\Gamma_n/2}{(\omega - \omega_n)^2 + \Gamma_n^2/4}, \quad (1.5)$$

¹Since the dirac function obeys $\delta(\omega - \omega_n) = \lim_{\Gamma_n \rightarrow 0} L(\omega)$, we recover the lossless case Eq. 1.4 for an ideal cavity.

where $\tau_n = 1/\Gamma_n$ is the n^{th} mode lifetime. Defining the resonance quality factor $Q_n = \omega_n \tau_n$, we can rewrite

$$L(\omega) = \frac{2 Q_n}{\pi \omega_n} \frac{1}{1 + 4 \left(\frac{\omega - \omega_n}{\omega_n}\right)^2 Q_n^2}. \quad (1.6)$$

Spatial shape of the LDOS The electric field is normalized in a such way that

$$\iiint |\mathbf{E}_n|^2 d\mathbf{r} = 1. \quad (1.7)$$

Therefore, \mathbf{E}_n can be defined as a function of the electric field associated to the n^{th} mode \mathcal{E}_n :

$$\mathbf{E}_n = \frac{\mathcal{E}_n}{\iiint |\mathcal{E}_n|^2 d\mathbf{r}}. \quad (1.8)$$

Finally, we assume a dipole emitting at ω_n and located at the n^{th} mode antinode \mathbf{r}_n where the field is maximum [$\mathbf{E}_n(\mathbf{r}_n) = \text{Max}(\mathbf{E}_n)$]. This corresponds to the maximum emission rate,

$$\frac{\gamma_n(\mathbf{r}_n, \omega_n)}{\gamma_0} = \frac{2 Q_n}{\pi \omega_0} \frac{|\mathcal{E}_n^i(\mathbf{r}_n)|^2}{\iiint |\mathcal{E}_n|^2 d\mathbf{r}} \frac{3\pi^2 c^3}{\omega_0^2} \quad (1.9)$$

and

$$\frac{\gamma_n(\mathbf{r}_n, \omega_n)}{\gamma_0} = \frac{3}{4\pi^2} \frac{Q_n}{V_n} \lambda_n^3 \quad (1.10)$$

where we have used $\lambda_n = 2\pi c/\omega_n$. We have also defined the mode effective volume

$$V_n = \frac{\iiint |\mathcal{E}_n|^2 d\mathbf{r}}{\text{Max}(|\mathcal{E}_n^i(\mathbf{r}_n)|^2)} \quad (1.11)$$

that characterizes the electric field confinement.

1.1.1.1 Mode volume expression

Mode confinement is usually defined thanks to energy confinement instead of the electric field confinement. This leads to

$$V_n = \frac{1}{2} \frac{\iiint [\varepsilon_0 \varepsilon |\mathcal{E}(\mathbf{r})|^2 + \mu_0 \mu |\mathcal{H}(\mathbf{r})|^2] d\mathbf{r}}{\text{Max}[\varepsilon_0 \varepsilon |\mathcal{E}|^2]}. \quad (1.12)$$

In a non dispersive medium, the electric and magnetic energy are equal and the effective volume is expressed as a function of the electric field only. The case for a dispersive and absorbing medium is more difficult. In chapter 3, we will discuss the definition of the modal volume for a lossy mode, namely a localized plasmon.

1.1.2 Discussion

The Purcell factor leads to a simple description of light-matter interaction in a cavity. A very interesting point is that it describes the interaction as a function of the cavity mode properties only, independently of the emitter properties. In particular, the highest interaction is achieved for high Q_n/V_n ratio.

This leads to strong effort in order to improve the quality factor of optical microcavity. That is, an increase of the mode lifetime in order to maximize the duration of the interaction. As we will see, it is however at the price of large mode volume. Indeed, the mode volume is diffraction limited, that means that the effective volume $V_{eff} \sim (\lambda/n)^3$. On the contrary, we will demonstrate in this thesis that surface plasmon polariton (SPP) present modal volume below the diffraction limit paving the way towards light-matter interaction at the nanoscale.

Finally, a full treatment of the Purcell factor in a medium of optical index n_1 leads to

$$F_p = \frac{\gamma}{n_1 \gamma_0} = \frac{3}{4\pi^2} \left(\frac{\lambda}{n_1} \right)^3 \frac{Q_n}{V_n} \quad (1.13)$$

and is achieved under the following assumptions:

- γ refers to the coupling to a given mode of the cavity;
- The cavity mode is a bound mode (so that the mode volume can be defined);
- Emission occurs at the cavity resonance;
- The emitter is located at the mode anti-node and oriented along the field polarization;

Generalization of the Purcell factor definition in plasmonic cavities is a challenging task since

- SPP are oftently leaky;
- SPP modes are sustained by dispersive and absorbing medium for which energy definition needs some care;
- in the near field zone, of interest in this work, the electric-field is not linearly polarized so that the dipole moment is not aligned along the electric field.

We will discuss these points in details in chapter 3.

1.1.3 Coupling efficiency (β factor)

So far, we have considered the ideal case of the coupling between an emitter and an individual cavity mode. In reality, the emitter can couple to the other cavity

modes, including leaky ones. The coupling efficiency into the mode of interest is the so-called β -factor:

$$\beta = \frac{\gamma_n}{\gamma} = \frac{\gamma_n}{\gamma_n + \gamma_{other}}. \quad (1.14)$$

In case of single mode cavity, we distinguish the coupling rate to the cavity mode $\gamma_n = \gamma_{cav}$ and leaky modes $\gamma_{other} = \gamma_{leak}$. In general, the leaky rate remains of the order of the initial radiative rate γ_0 so that $\beta \simeq \gamma_{cav}/(\gamma_{cav} + \gamma_0) \simeq F_p/(1 + F_p)$. A Purcell factor $F_p \sim 10$ corresponds to a coupling efficiency $\beta \sim 90\%$. In addition to high emission efficiency, high β -factor is also a key parameter to achieve low threshold laser [Yokoyama 1992].

1.1.4 Optical microcavities

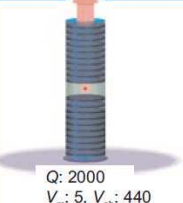
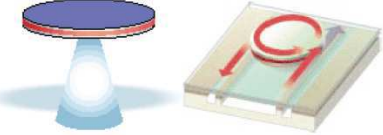
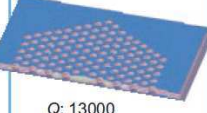
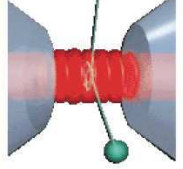
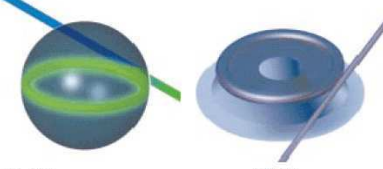
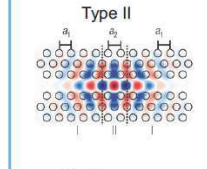
	Fabry-Perot	Whispering gallery	Photonic crystal
High Q	 <p>Q: 2000 V_m: 5, V_{ph}: 440</p>		 <p>Q: 13000 V_m: 1.2, V_{ph}: 200</p>
Ultra-high Q		 <p>Q: 10^9 V_m: 2000, V_{ph}: 30000</p> <p>Q: 10^8 V_m: 6, V_{ph}: 10000</p>	 <p>Q: 10^7 V_m: 2, V_{ph}: 200</p>

Figure 1.2: Overview of the whole performances achievable by optical cavities. The mode volume V_m are in units of λ^3 . The characteristics are provided from the following references. Upper row: micropillar [Gérard 1998], microdisk [Gayral 1999], add/drop filter [Djordjev 2002, Rabiei 2002], photonic crystal cavity [Srinivasan 2003]. Lower row: Fabry-Perot bulk optical cavity [Hood 2000, Buck 2003], microsphere [Vernooy 1998], microtoroid [Armani 2003], type II photonic crystal [Song 2005]. Adapted by permission from Macmillan Publishers Ltd: Nature (Ref. [Vahala 2003]), copyright (2003). Adapted by permission from Macmillan Publishers Ltd: Nature (Ref. [Song 2005]), copyright (2005). Reproduced by permission of The Royal Society of Chemistry from Mario Agio, *Nanoscale*, 2012, 4, 692-706, DOI: 10.1039/C1NR11116G.

Optical cavities are the subject of intensive studies since decades. Figure 1.2 depicts typical Q and V values. Optical microcavities exhibit huge resonance qualities ($Q > 1000$ and up to 10^9) enabling to reach high Purcell factors F_p . Nevertheless, they present the main disadvantage to badly confine optical modes. As shown in

Figure 1.2, the mode confinement is diffraction-limited.

We report in table 1.1 the most recent performances. Optical cavities can enhance drastically the emission ($F_p > 100$) thanks to their high quality factor². Nevertheless, the resonance quality improvements are often achieved at the expense of the mode volume which is diffraction limited. Hence, light matter interaction at the nanoscale necessitates a different paradigm.

Plasmonic nanostructures, that could present strongly subwavelength mode volume are promising in this perspective. It is however at the price of bad quality factor due to important losses as we will discuss in details in the next chapters.

Table 1.1: Report of recent improvements in optical cavities

	Quality factor	Mode volume	Purcell factor	References
Micropillar	7,400	$0.3\mu\text{m}^3$		[Reithmaier 2004]
	22,000	$0.5\mu\text{m}^3$	61	[Press 2007]
	40,000	$1.2\mu\text{m}^3$		[Reitzenstein 2007]
			25	[Varoutsis 2005]
			9	[Santori 2002]
Microtoroid	$4 \cdot 10^8$	$160(\lambda/n)^3$	$2 \cdot 10^5$	[Kippenberg 2004]
Photonic crystals			28	[Laurent 2005]
			10	[Santori 2002]
	40,000	$0.9(\lambda/n)^3$	3,500	[Srinivasan 2004]
	650,000	$1.2(\lambda/n)^3$	40,000	[Song 2005]
	$> 10^6$	$1.2(\lambda/n)^3$	63,000	[Tanabe 2007, Asano 2006]
	$> 10^9$	$1.3(\lambda/n)^3$	$58 \cdot 10^6$	[Tanaka 2008]
	$4.3 \cdot 10^5$		[Grinberg 2012]	

1.2 Metal enhanced spectroscopies

In this section, we briefly summarize the properties of propagating and localized plasmons. We then present a brief state of the art of metal enhanced fluorescence. For a review, the reader is referred to [Fort 2008].

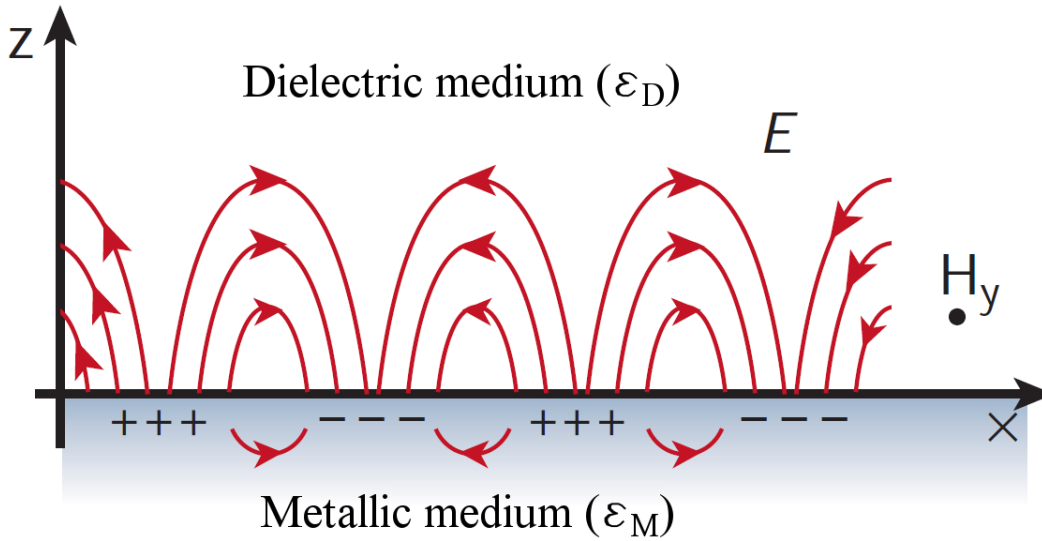


Figure 1.3: Schematic view of a Surface Plasmon-Polariton on a flat metallic film. Adapted by permission from Macmillan Publishers Ltd: Nature (Ref. [Barnes 2003]), copyright (2003).

1.2.1 Surface plasmon polariton: description

1.2.1.1 Delocalized Surface Plasmon mode

A plasmon is a collective oscillation of a free electron gas coupled to an electromagnetic wave [Raether 1988]. Let us consider the simple case of an interface separating two semi-infinite media as illustrated in Figure 1.3. ϵ_D and $\epsilon_M(\omega)$ are the dielectric functions of the dielectric and the metallic medium, respectively. The SPP mode results from coupling a Transverse Magnetic (TM) polarized wave (of wavenumber k_0) to a surface charge density.

The complex constant of propagation of the SPP is

$$\tilde{k}_{spp} = \sqrt{\frac{\epsilon_D \epsilon_M(\omega)}{\epsilon_D + \epsilon_M(\omega)}} k_0. \quad (1.15)$$

The mode propagation constant is then $k_{spp} = \text{Re}(\tilde{k}_{spp})$ whereas its propagation length is $L_{spp} = \frac{1}{2 \text{Im}(\tilde{k}_{spp})}$. In the visible and near-infrared, L_{spp} ranges from few to tens of μm . Note that the mode penetration depth in air is rather low $\delta \sim 100 \text{ nm}$ due to the high k_{spp} value. This transverse confinement is notably at the origin of surface plasmon resonance (SPR) to improve sensing sensibility.

²In case of extremely high Purcell factor, the coupling regime is probably strong coupling (actually if the coupling constant is higher than cavity and emitter decay rates).

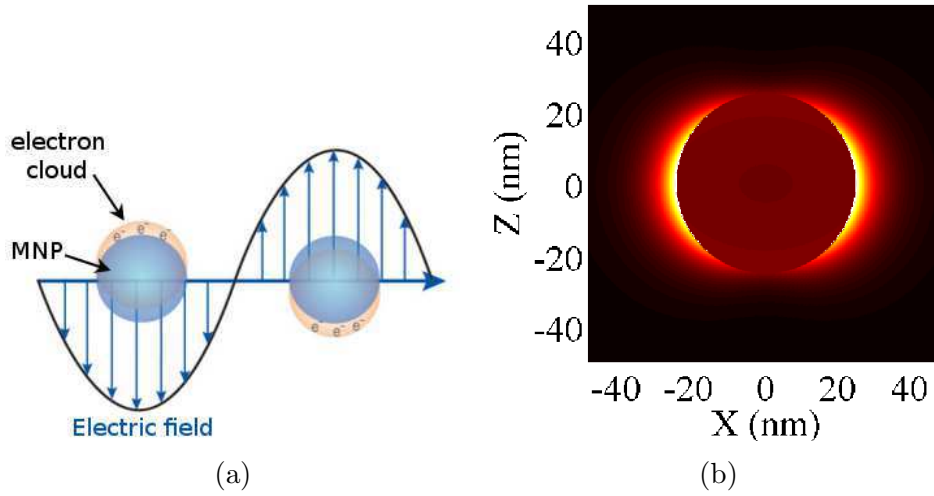


Figure 1.4: a) Schematic view of a Localized Surface Plasmon Polariton. The coupling of an incident electric field with the MNP creates collective oscillations of electrons within the particle. This feature induces a change of the density of charge at the metal surface. b) Dipolar mode intensity profile of a silver nanoparticle ($\lambda = 363$ nm).

1.2.1.2 Localized Surface Plasmon

Let us consider an incident wave illuminating a metal nanoparticle. The electric field induces oscillations of the free electron cloud of the metal (Figure 1.4a). Such mode is called Localized Surface Plasmon Polariton (LSP). The main property of this mode is to be confined at the sub-wavelength scale. This feature involves also a strong enhancement of the field which is scattered by the particle, as depicted on Figure 1.4b: a huge density of electric field intensity occurs near the metal surface. Hence, MNPs are able to convert propagating modes (far field) into a near field mode. That is the reason why such systems are exploited as nanooptical antenna [Bharadwaj 2009].

It is possible to describe the main optical properties of LSP by considering spherical MNPs within the quasi-static approximation. For sphere radius R negligible with respect to the incident wavelength λ_0 , the n^{th} mode polarisability writes

$$\alpha_n = \frac{n(\varepsilon_M - \varepsilon_B)}{(n+1)\varepsilon_B + n\varepsilon_M} R^{2n+1}. \quad (1.16)$$

ε_M and ε_B are the dielectric function of the metallic sphere and the background medium respectively. The n^{th} order polarisability characterizes the optical response of the sphere to an external excitation. In presence of an electric field, the MNP is polarised so that it supports an induced dipole $\mathbf{p} = 4\pi\varepsilon_0\varepsilon_B\alpha_1\mathbf{E}_0$ and, if the incident field varies on the particle dimension, quadrupolar ($n = 2$) or higher mode that obeys

$$\mathbf{p}^{(n)} = \frac{4\pi\varepsilon_0}{(2n-1)!!} \alpha_n \nabla^{n-1} \mathbf{E}_0. \quad (1.17)$$

The mode resonance occurs at the pole of α_n that is:

$$\text{Re} \{ \varepsilon_M(\lambda_n) \} = -\frac{n+1}{n} \varepsilon_B. \quad (1.18)$$

As depicted in Figure 1.5, the higher the order n is, the higher the resonance frequency is, with strong accumulation of high order modes in a limited spectral range.

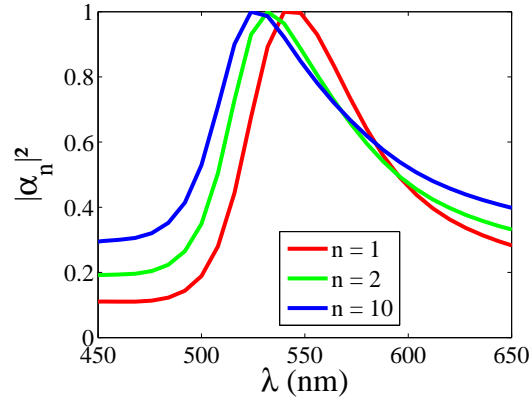


Figure 1.5: Quasi-static polarisability of the n^{th} localized mode supported by a 80 nm silver particle. The background medium dielectric constant is $\varepsilon_B = 2.25$.

1.2.2 Fluorescence near a metallic film

In 1970, K.H. Drexhage reported the coupling between a metallic mirror and an emissive layer [Drexhage 1970]. His results showed influences of the mirror on the fluorescence lifetime at micrometer scale distances. He observed also that emission lifetime decreased dramatically at a close proximity (nanoscale) to the flat metal surface due to non-radiative energy transfer to the metal film [Barnes 1998, Worthing 2001, Moal 2007, Lakowicz 2004].

Fluorescence enhancement near a flat metal film The emission lifetime decrease of an emitter at a close proximity to a metal surface is mainly due to huge absorption by the metal, that leads to fluorescence quenching. Nevertheless, figure 1.6 shows that emission is enhanced at specific distances from the metal surface. This is of great interest for *e.g.* improving DNA chip [Le Moal 2009] or biosensing [Moal 2007].

Fluorescence enhancement is mainly due to the enhancement of the excitation field [Fort 2008]. Additionally, it has been demonstrated that the proximity of metal surface can reduce the blinking of the fluorescence emission [Stefani 2007].

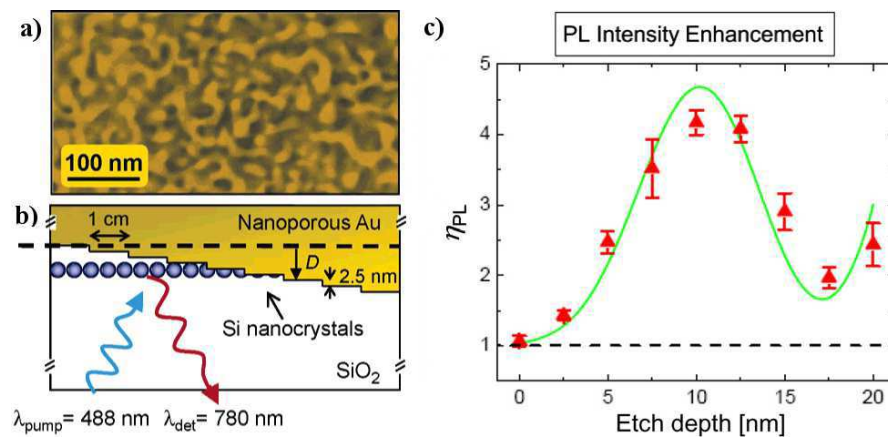


Figure 1.6: a) SEM image of the nanoporous gold surface. b) Schematic cross section of the sample. The distance D between the gold surface and the emitting silicon nanocrystals is set by etching the nanoporous gold giving stairs of 2.5 nm height. Excitation and detection are made from the bottom side of the sample. c) Fluorescence enhancement measured as a function of the etch depth, D (triangles). The solid line is a fit to the data using a model that accounts for the spatial distribution of silicium nanocrystals and the enhanced local field. Adapted with permission from Ref. [Biteen 2005]. Copyright (2005) American Chemical Society.

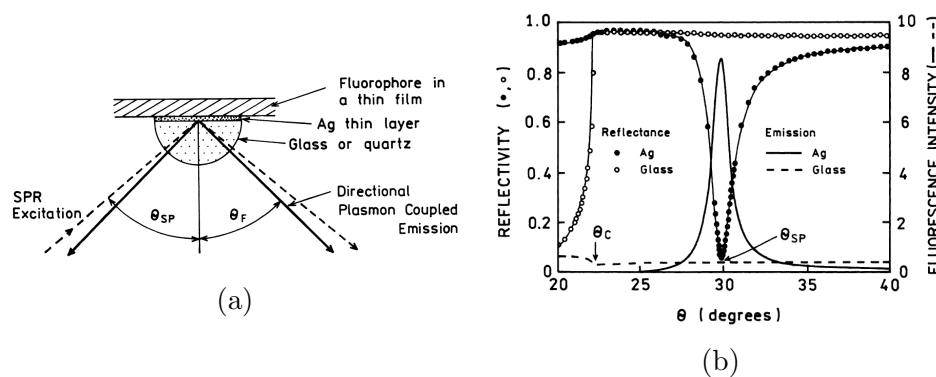


Figure 1.7: a) Schematic view of surface plasmon resonance (SPR, dashed arrows) and of SPCE cone (solid arrows). b) Dotted black curve: reflectivity of a silver nanolayer. Solid curve: Fluorescence intensity measurement of dye molecules above the same metallic layer. Reprinted from Ref. [Lakowicz 2004], Copyright (2004), with permission from Elsevier.

Surface plasmon coupled emission Figure 1.7b depicts the angular resonance θ_{SP} of surface plasmon supported by a flat metal film (black dotted curve). The curve is acquired using the Kretschmann-Raether set-up shown in Fig. 1.7a. Reciprocally, surface plasmon can also be excited by emitting fluorescent materials placed above the film. Lakowicz and coworkers pointed out in 2004 the directionality of surface plasmon coupled emission (SPCE) [Lakowicz 2004, Gryczynski 2004a, Gryczynski 2004b]. It is illustrated by the

solid line on Fig. 1.7b which corresponds to leakage radiation of the excited SPP. SPCE allows direct and easy characterization of the propagating plasmon since it is measured in the k-space (propagation constant) [Grandidier 2010, Drezet 2008]. We will use in chapter 2, SPCE microscopy to characterize a plasmonic mirror.

1.2.3 Surface enhanced spectroscopies

The coupling between an emitter and a plasmonic structure could lead to strong increase of the excitation field and of the emission rate. This leads to enhance the fluorescence signal with applications ranging from sensing to single photon source improvement. We briefly introduce the main achievement for surface enhanced spectroscopies.

Surface Enhanced Raman Spectroscopy (SERS) Surface enhanced Raman spectroscopy relies on both excitation and emission enhancement for a Raman active molecule in close proximity to a MNP. The enhancement factor is of the order of $|E_{loc}|^4/|E_0|^4$ where $|E_{loc}|$ is the local field at the molecule position. Enhancement factors can typically reach order of 10^6 [Moskovits 1985], enabling single-molecule Raman spectroscopy [Nie 1997, Kneipp 1997, Kneipp 1998, Etchegoin 2010, Etchegoin 2011]. Highest enhancement are achieved in coupled MNPs (dimer) which generates a hot spot where the molecules are excited (Figure 1.8).

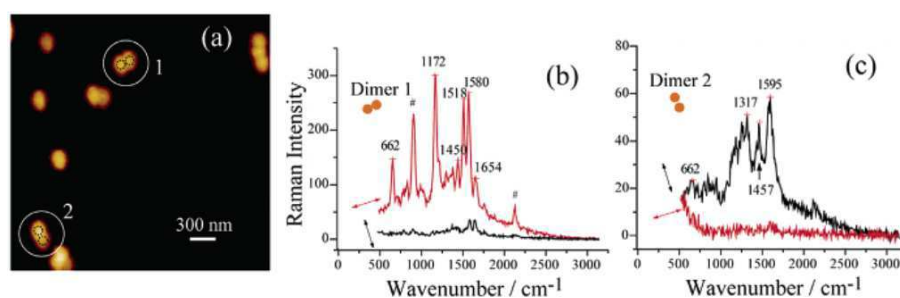


Figure 1.8: a) Topography of distributed gold nanoparticles. (b, c) Near-field Raman spectra on dimers. Strong enhancement is achieved by coupling molecules with the longitudinal mode of a couple of GNPs (dimer). On the other hand, enhancement dramatically decreases by coupling molecules with the transverse mode of the dimer. Adapted with permission from Ref. [Imura 2006]. Copyright (2006) American Chemical Society.

Metal enhanced fluorescence The figure 1.9 represents the emission rate of a single dye molecule coupled to a single gold nanoparticle (GNP) [Anger 2006,

[Kühn 2006]. We observe a typical quenching for small separation distance due to non radiative energy transfer from the excited molecule to the MNP. It is in competition with the field enhancement near the particle surface so that a maximum fluorescence enhancement occurs for $d \approx 5$ nm. This demonstrates the capability to control single molecule emission [Girard 1995, Colas des Francs 2008, Eghlidi 2009, Rolly 2011, Busson 2012a].

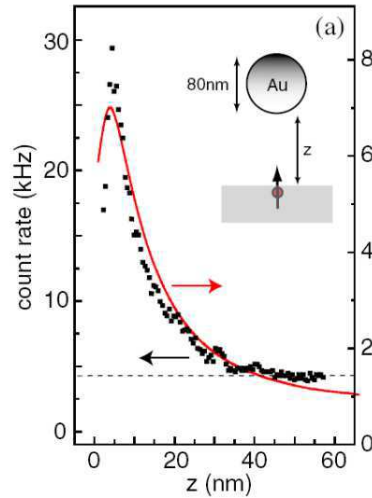


Figure 1.9: Fluorescence intensity as a function of the distance between a dye molecule and a gold nanoparticle. Reprinted figure with permission from P. Anger et al., *Physical Review Letter* **96**, 113002, 2006. Copyright (2006) by the American Physical Society.

Single Photon source emission Since single molecule emission can be controlled by coupling to a nearby MNP, several groups investigate the possibility to accelerate single photon source [Akimov 2007, Schietinger 2009, Celebrano 2010, Marty 2010, Busson 2012b]. As an example, Fig. 1.10 describes a recent work done in the group of Schietinger.

A Nitrogen-Vacancy (NV) in a nanodiamond is used as the color center. The fluorescence intensity decay presented in 1.10(d) shows that the emitter exhibits a fluorescence lifetime that decreases by coupling to the MNP.

The Figure 1.10(e,f) are second order auto correlation functions $g^2(\Delta t)$ where Δt is the lag time between two consecutive photon events. $g^2(\Delta t)$ describes the probability to emit a second photon at time Δt after a first emission. At zero lag time $g^2(0) = 1 - 1/N < 0.5$ which means there is $N = 1$ emitter inside the diamond. The reduction of the dip width demonstrates an acceleration of the single photon emission.

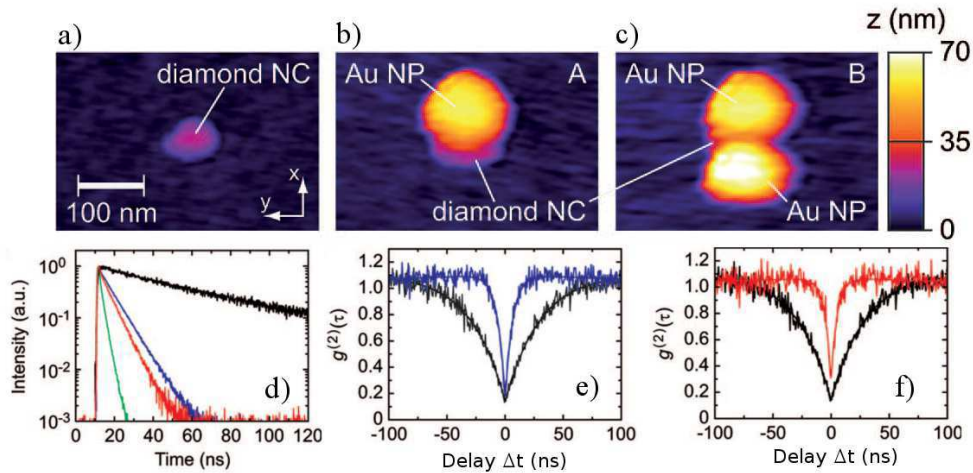


Figure 1.10: a,b,c) AFM topographical pictures of a) a nanodiamond, b) a GNP approached closely to the nanodiamond, c) two GNPs close to the nanodiamond. GNPs nano-manipulations were performed by utilizing an AFM tip. d) Intensity decay of the NV center emission performed before and after GNPs manipulations. e,f) $g^2(\Delta t)$ autocorrelation function of the NV center emission (black curve) and coupled with one GNP (e, blue curve) or two GNPs (f, red curve). Adapted with permission from Ref. [Schietinger 2009]. Copyright (2009) American Chemical Society.

Surface Plasmon laser One of the most challenging applications of LSPs is the design of a SPASER (surface plasmon amplification by stimulated emission of radiation) or plasmon nanolaser [Bergman 2003]. In this system (Fig. 1.11), the laser optical cavity feedback is replaced by a plasmonic nanoparticle [Noginov 2009, Garcia-Vidal 2009, Stockman 2010]. The metal core is surrounded by a gain medium (the dielectric shell is doped with fluorescent molecules). When the gain compensates the SPP losses, the system behaves as a coherent optical nanosources [Protsenko 2005, Noginov 2009, Lu 2012].

1.3 Conclusion

Optical microcavities provide high quality factors so that they can reach high Purcell factors. On the other hand, their plasmonic counterparts provide a sub-wavelength mode volume for achieving high Purcell factors. Surface plasmons are strongly confined modes so that a simple flat film enables fluorescence enhancement.

In the following chapters, we discuss the characteristics of two kinds of plasmonic structures for fluorescence enhancement. The first is a direct transposition of 1D photonic crystal concept to surface plasmon. The second structure is a metal nanoparticle which naturally supports localized surface plasmons, extending the concept of plasmonic cavity to open systems.

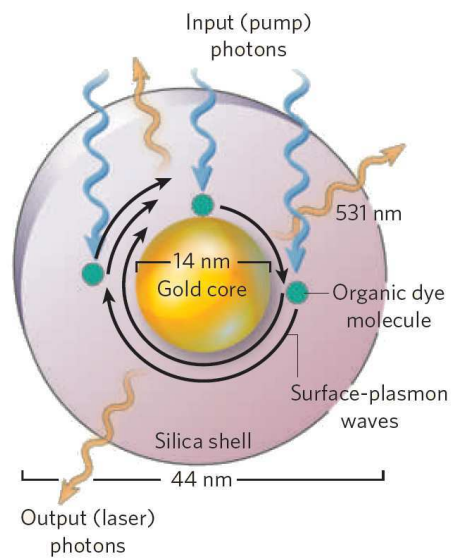


Figure 1.11: Schematic view of core-shell spaser. The gold particle is surrounded by a gain medium (doped with dye molecules). Above the spaser threshold, stimulated emission of LSP occurs, forming a nanolaser. Reprinted by permission from Macmillan Publishers Ltd: Nature (Ref. [Garcia-Vidal 2009]), copyright (2009).

Single molecule fluorescence control in in-plane plasmonic cavity

Contents

2.1	Surface plasmon coupled emission near a distributed SPP Bragg reflector (DBR)	20
2.1.1	Surface plasmon coupled emission of fluorescent nanobeads	20
2.1.2	Mirror efficiency	23
2.2	In-plane SPP cavity	26
2.2.1	Decay rate and relaxation channels	26
2.2.2	Single molecule fluorescence lifetime imaging	29
2.3	Conclusion	36

Optical microcavities support strongly confined modes into which the spontaneous emission of a quantum emitter is mainly redirected. Optical microcavities rely on 3D-confinement of bulk modes to improve light-matter interaction [Vahala 2003]. However, this necessitates to realize for instance complex 3D photonic band gap crystal and leads to challenging nanofabrication processes. Furthermore, as reported in Chapter 1, the mode confinement is diffraction limited. Another possibility is to confine surface waves such as surface plasmon polariton (SPP).

Delocalized surface plasmons are naturally confined at the metal surface so that a planar constraint is sufficient to achieve full 3D mode confinement. In this context, we are interested in planar plasmonic cavities since it is a direct transposition of Fabry-Perot optical microcavities to surface waves.

The studied in-plane plasmonic cavity consists of two SPP distributed Bragg reflectors (DBR) deposited on a flat metal film [Descrovi 2005, Weeber 2007b, Weeber 2007a, Wang 2008, Gong 2009]. The SPP confinement in a planar cavity has been demonstrated by near-field optical microscopy [Weeber 2007b, Weeber 2007a, Wang 2008], and cathodoluminescence [Kuttge 2009]. In addition, the capabilities of SPP cavities for improving solid state

optical sources has been demonstrated [Winter 2008, Gong 2009].

In this chapter, we are interested in the control of single emitter fluorescence in a coplanar plasmonic cavity. To this aim, we first discuss in section 2.1 the effect of a single SPP Bragg reflector on the propagation of a locally excited plasmon. We notably characterize the efficiency of the mirror at the emission wavelength.

In section 2.2, we numerically and experimentally investigate fluorescence decay rate of dye molecules randomly dispersed within a SPP cavity. We measure their fluorescence lifetime as a function of the cavity size and the molecule position inside the cavity. We show that the dye photodynamic is governed by the surface modes confined in the plasmonic cavity, in direct analogy with the emission control obtained by the confinement of bulk mode in one-dimensional (1D) Fabry-Perot cavity.

2.1 Surface plasmon coupled emission near a distributed SPP Bragg reflector (DBR)

2.1.1 Surface plasmon coupled emission of fluorescent nanobeads

Figure 2.1 represents the optical setup, a schematic view of the sample and a scanning electron micrograph of the Bragg mirror. The fabrication of this device is performed by electron-beam lithography [Weeber 2007b]. The ridges constituting the mirror have been first designed on a PMMA coated ITO-doped glass substrate. Then 50 nm of gold were thermally evaporated to form the ridges. Once polymer resist (PMMA) was lifted off, an additional gold film is deposited onto the gold grating. As a result, the SPP Bragg mirror consists of six gold lines grating (period Λ , width $W = 90$ nm and height $h = 50$ nm) above a 50 nm thick gold film. We spin-coated an aqueous suspension of fluorescent polystyrene (PS) particles (*FS02F, BangLaboratories, Inc*, mean diameter 60 nm) onto the sample. The nanobeads have an emission wavelength $\lambda_{em} = 690$ nm (see the spectrum in the inset of Fig. 2.1).

We first imaged the randomly deposited nanoparticles by confocal scanning microscopy with a high numerical aperture ($NA = 1.49$, $100\times$, oil immersion objective) in order to locate fluorescent beads of interest. SPCE is then analyzed by leakage radiation microscopy (LRM) in the Fourier plane as described in Ref. [Grandidier 2010].

For a fluorescent bead located on a bare gold surface, the SPCE is displayed in Fig. 2.2(a). It shows a well-defined effective index $n_{SPP} = k_{SPP}/k_0 = 1.03 \pm 0.01$, in agreement with the calculated one ($n_{SPP} = k_{SPP}/k_0 = 1.034$). This first result indicates that the fluorescent bead constituted of randomly oriented dye molecules

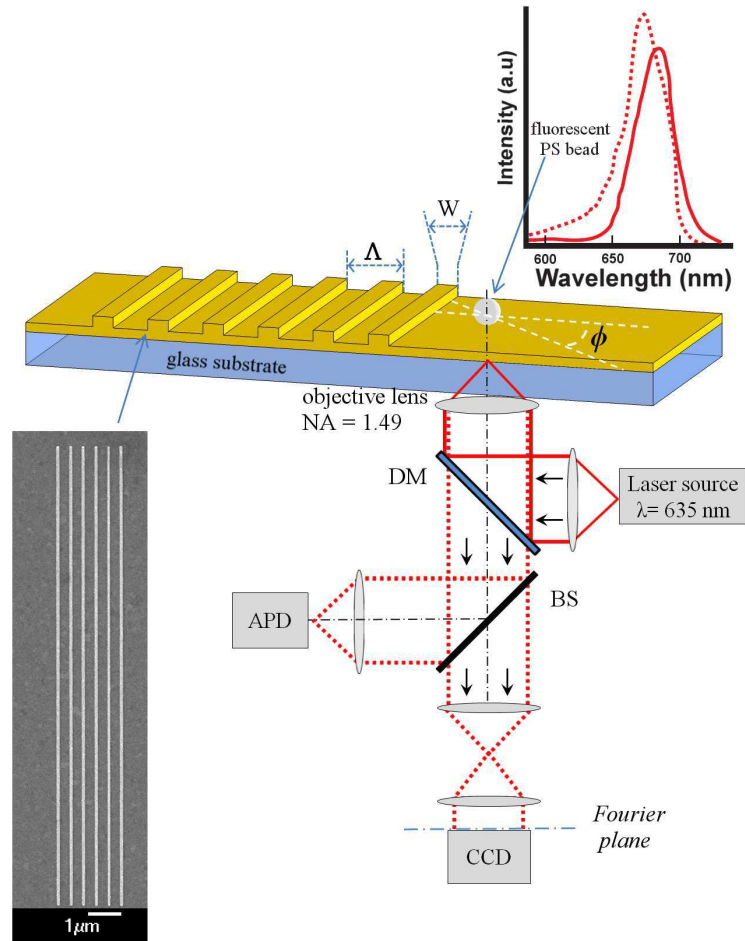


Figure 2.1: Scheme of SPCE leakage radiation microscopy. Fluorescent polystyrene (PS) nanobeads are excited using a 635 nm picosecond pulsed diode laser (*LDH-P-635, Picoquant GmbH*). The top inset depicts the absorption (dotted red curve) and emission (solid red curve) spectrum [Ban] of the doped beads. Their fluorescence signal is filtered using a dichroic mirror and a 665 nm long pass filter. A portion of the fluorescence signal is detected by an APD for scanning confocal microscopy. The rest is recorded in the Fourier plane with a CCD camera. DM: Dichroic mirror. BS: beam splitter. APD: Avalanche Photodiode. CCD: Charge Coupled Device camera (*Andor Technology, Luca^{EM}S 658M*). Bottom inset: Scanning electron micrograph of a plasmonic DBR.

acts as a local isotropic SPP source convenient for investigating the properties of the Bragg mirrors. The recorded signal is different when the bead is located in front of the Bragg mirror as shown in Fig. 2.2(b). Indeed, SPP wavevectors oriented towards the mirror are suppressed whereas the addition of the direct and reflected SPP waves leads to a brighter lobe in the opposite direction. We confirm that this SPCE distribution originates from reflection on the mirror with the simple model illustrated on Fig. 2.3.

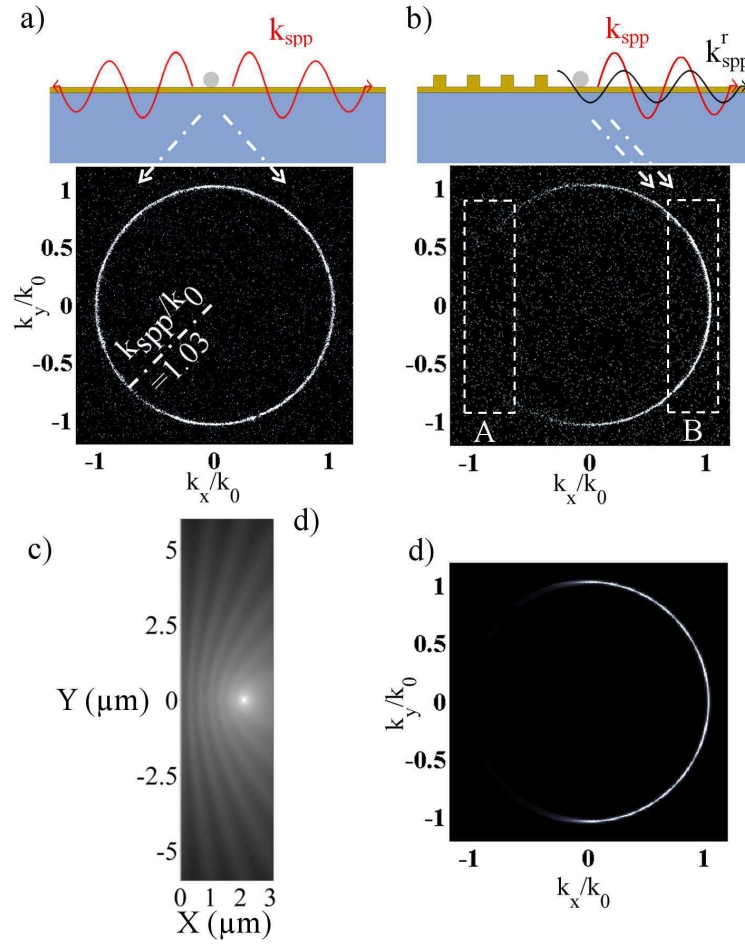


Figure 2.2: a-b) Radiation leakages of the fluorescent signal emitted by the PS nanobead recorded in the Fourier plane. In (b), the bead is in front of the mirror whereas it lies on a flat gold film in (a). The drawings on the top depict the SPP propagation. \mathbf{k}_{SPP} and \mathbf{k}_{SPP}^r refer to the incident and reflected wavevectors, respectively and the corresponding SPP propagation towards and away from the plasmonic mirror are indicated by zones A and B in (b). c and d) Modeling of the image (c, logarithmic scale) and Fourier (d) planes. The fluorescent source is located at $2.1 \mu\text{m}$ to the mirror.

To this aim, the isotropic SPCE from the fluorescent nanobead is described by a transverse magnetic (TM) field

$$\mathbf{H}(\rho) = H_0 e^{ik_{SPP}\rho} e^{-\rho/2L_{SPP}} / \sqrt{\rho} \mathbf{e}_\theta \quad (2.1)$$

where $L_{SPP} = 10.5 \mu\text{m}$ is the SPP propagation length calculated at $\lambda = 690 \text{ nm}$. The plane mirror is modeled considering a secondary source, at the position ρ_S symmetric of the primary source with respect to the mirror plane. We assume an average reflection coefficient [González 2006] $r = 0.2$. The reflected field expresses

$$\mathbf{H}_r(\rho) = r H_0 e^{ik_{SPP}R_S} e^{-R_S/2L_{SPP}} / \sqrt{R_S} \mathbf{e}_\theta \quad (2.2)$$

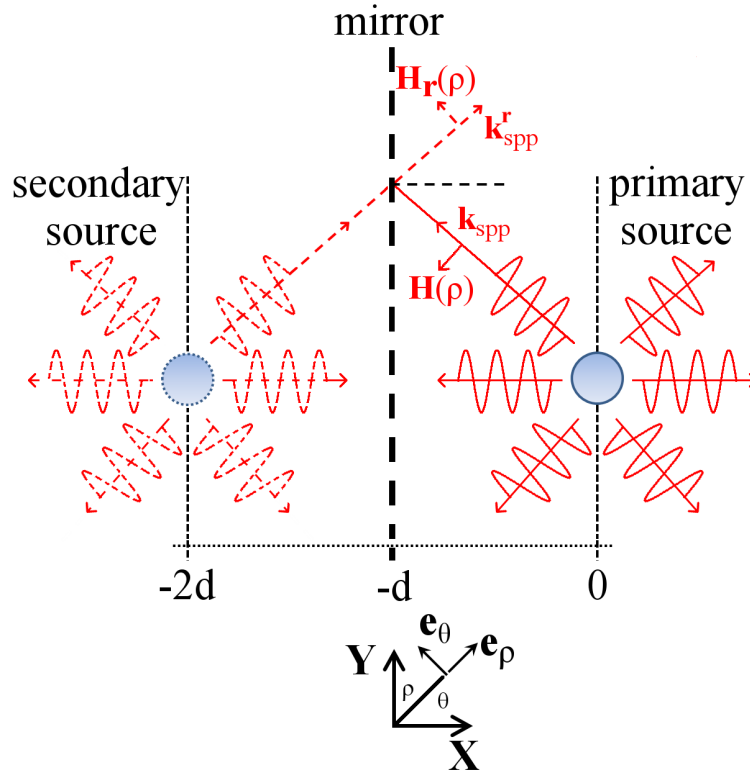


Figure 2.3: Schematic view of the model used for the calculations presented in Fig. 2.2(c,d).

and is computed at a point situated at a distance $R_S = |\boldsymbol{\rho} - \boldsymbol{\rho}_S|$ from the secondary source. Figures 2.2(c) and 2.2(d) show the intensity distribution of the total magnetic field $|\mathbf{H}_{\text{tot}}(\boldsymbol{\rho})|^2 = |\mathbf{H}(\boldsymbol{\rho}) + \mathbf{H}_r(\boldsymbol{\rho})|^2$ and of its Fourier-transform $|\tilde{\mathbf{H}}_{\text{tot}}(k_x, k_y)|^2$, respectively. The intensity of the Fourier-transform $|\tilde{\mathbf{H}}_{\text{tot}}(k_x, k_y)|^2$ calculated in Fig. 2.2(d) reproduces the experimental image recorded in the Fourier plane [Fig. 2.2(b)].

This confirms that the plasmonic mirror efficiently reflects the SPP launched by the fluorescent nanobead. Fourier-plane imaging also reveals that the mirror is efficient for incident angle $\phi \leq 40^\circ$ (see the dark angular sector zone A in Fig. 2.2b), in agreement with a previous study [González 2007].

2.1.2 Mirror efficiency

We now investigate the effect of the grating period Λ . Figure 2.4(a) presents a figure of merit of the DBR. It is defined by the extinction ratio A/B where A and B refer to the SPP signal propagating towards and away from the mirror, respectively. Practically, A and B were estimated by integrating the intensity over the A and B areas indicated in the inset of Fig. 2.4a) that corresponds roughly to the efficient reflection angular zone $\phi \leq 40^\circ$. We observe an almost full extinction for $\Lambda = 333$ nm corresponding to half the SPP wavelength $\lambda_{SPP} = \lambda_{em}/n_{SPP} = 667$ nm, as expected

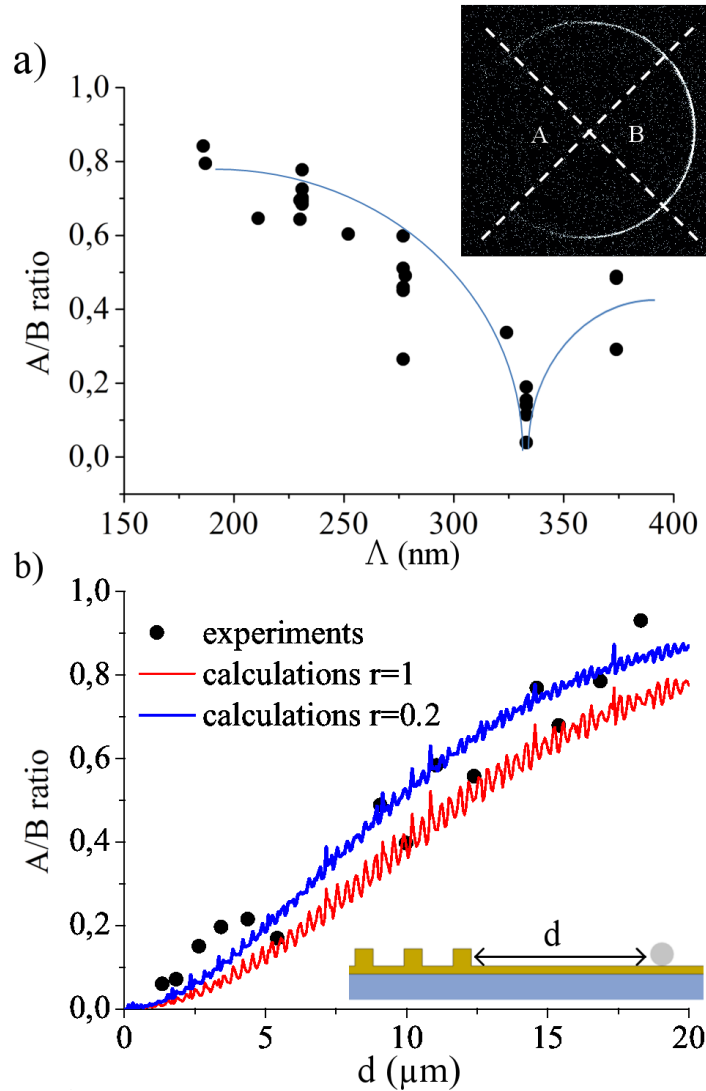


Figure 2.4: a) Extinction ratio A/B as a function of the grating period (the solid line is a guide to the eyes). We have considered beads located at distance less than $d = 5 \mu\text{m}$ to the grating. b) A/B as a function of the bead distance to grating for a fixed period $\Lambda = 333 \text{ nm}$. Scattered points: experimental data, solid red curve: data calculated with Fourier planes simulated such as done in Fig. 2.2(d) ($r = 0.2$). We also consider a perfect mirror ($r = 1$) to clearly see the interference oscillations.

for a SPP propagating at normal incidence. For incident angle ϕ on the mirror, the optimal Bragg mirror period should be [González 2006]

$$\Lambda = \frac{\lambda_{SPP}}{2 \cos(\phi)}, \quad (2.3)$$

that varies from $\Lambda(\phi = \pm 40^\circ) = 435 \text{ nm}$ to $\Lambda(\phi = 0) = 333 \text{ nm}$. However for an incident angle $\phi \neq 0$, the amplitude of the wave impinging on the mirror decreases as $e^{-d/[\cos(\phi)L_{SPP}]}$ so that the main contribution to the reflected signal originates

from normal incidence.

We also plot in fig. 2.4(b) the A/B ratio as a function of the bead distance to the mirror. We observe that the extinction ratio decreases with the distance due to the finite SPP propagation length. The ratio A/B does not significantly change for distances $d \leq 5 \mu\text{m}$ between the bead and the grating, justifying that Fig. 2.4(a) is a measure of the mirror efficiency.

We plot in Fig. 2.4(b) the ratio A/B calculated using the simple model described above and achieve a good agreement with the measured data. We also consider a perfect mirror to clearly see the signal modulation. We check that the period of the small oscillations is $\lambda_{SPP}/2 = 333 \text{ nm}$, due to interference between the forward and backward SPPs. We observe a large dispersion of the measured ratio A/B in Figs. 2.4(a) and 2.4(b) that may be explained by scattering on the gold ridges that is not taken into account in our simple model. The interference signature is also visible by close inspection of the image in the Fourier plane as observed in Fig. 2.5. Indeed, the optical path between the source and the mirror expresses $l = d/\cos(\phi)$, so that it depends on the propagation direction (*i.e.* angle ϕ). This reveals the spatial coherence of the localized nanosource.

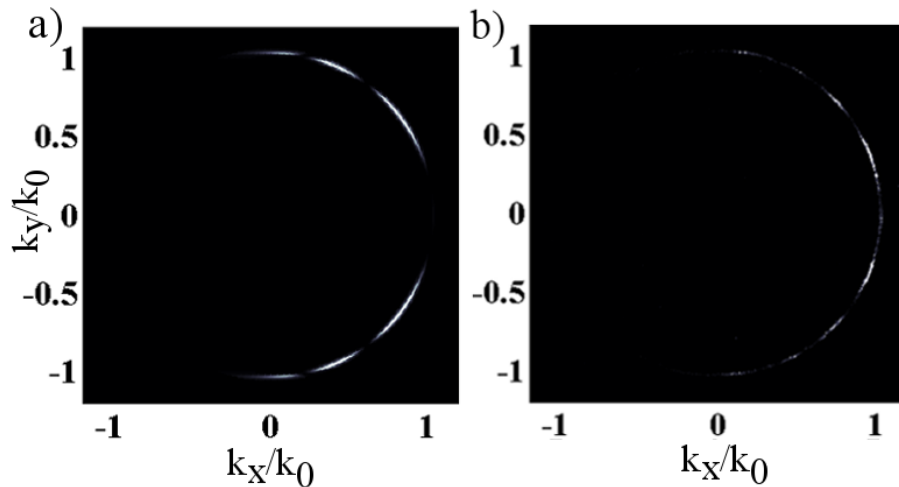


Figure 2.5: a) Simulated Fourier plane of a coherent source placed at 850 nm from a mirror with a reflection coefficient $r = 1$. b) Fourier plane acquired for a fluorescent nanobead placed at 850 nm from a SPP Bragg mirror. Bright and dark lobes appears in the Fourier plane, that originates from interference between SPP and reflected SPP.

The experimental results are further explained on the basis of the intrinsic properties of the Bragg mirror disregarding the local and incoherent nature of the SPP source. Indeed, Fig.2.6(a) shows the reflectivity of a thin gold film textured by an infinitely extended Bragg mirror with parameters identical to the experimental ones. For a

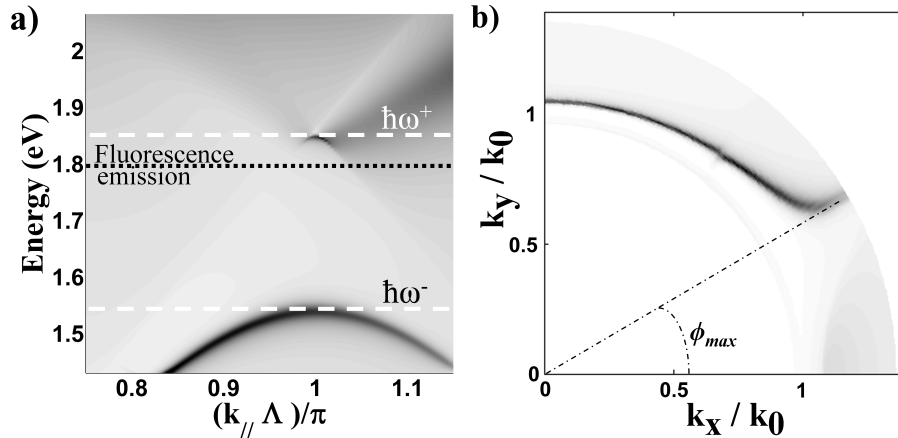


Figure 2.6: a) Calculated reflectivity R of a periodically textured film [gray scale from $R = 0.4$ (black) to $R = 1$ (white)]. The pitch of the grating is $\Lambda = 333$ nm. $\hbar\omega^+$ and $\hbar\omega^-$ denote the upper and the lower boundaries of the energy bandgap open by the textured film. They correspond to free-space wavelengths $\lambda^+ = 675$ nm and $\lambda^- = 790$ nm, respectively. The fluorescence emission frequency is within the bandgap ($R = 0.86$ at fluorescence emission $\hbar\omega_{em} = 1.79$ eV). b) Isofrequency map of the reflectivity computed at the fluorescence emission ($\lambda_{em} = 690$ nm).

plane wave TM polarised with a plane of incidence perpendicular to the lines of the grating, the reflectivity reveals a broad band gap. The emission peak of our beads is located within this band gap, close to the upper band edge of the plasmonic Bloch mode sustained by the Bragg mirror. Indeed, the bandgap width is $\Delta E \approx 0.27$ eV corresponding to free space wavelength range $675 \text{ nm} \leq \lambda \leq 790 \text{ nm}$. This covers the emission spectra of the fluorescent nanobeads (centered at $\lambda_{em} = 690$ nm and with a full width at half maximum $FWHM \approx 35$ nm [Ban], see top inset in Fig. 2.1). Next, we compute the isofrequency reflectivity map of the infinitely extended Bragg mirror at the free space wavelength $\lambda_{em} = 690$ nm (see Fig. 2.6(b)) using the differential method [Weeber 2007b]. We observe an acceptance angle of $\phi \leq 30^\circ$ in reasonable agreement with $\phi \leq 40^\circ$ obtained for the six ridges used experimentally. This demonstrates that the large bandwidth of plasmonic Bragg mirrors is adapted to control emission at room temperature. Relying on these results, we have designed in-plane cavities discussed in the next section.

2.2 In-plane SPP cavity

2.2.1 Decay rate and relaxation channels

Let us now consider an in-plane SPP cavity opened between two plasmonic Bragg mirrors. In this part, we numerically investigate the fluorescence decay rate of single molecules placed in the plasmonic cavity, before the experimental measurements

discussed in the next section. We selected high quantum efficiency dye molecules emitting at $\lambda_{em} = 670$ nm, close to the regime studied in the previous section.

The SPP effective index of a glass/gold (50 nm)/air slab is $n_{SPP} = 1.037$ at this wavelength. The distributed Bragg mirror period is therefore fixed at $\Lambda = \lambda_{em}/(2n_{SPP}) \approx 320$ nm. It consists of six $50 \text{ nm} \times 50 \text{ nm}$ gold ridges. The fluorescence decay of a dipolar emitter located inside the cavity is calculated with the formalism explained in Ref. [Barthes 2011]. For simplicity, the emitter is located at the cavity center, 25 nm above the gold film.

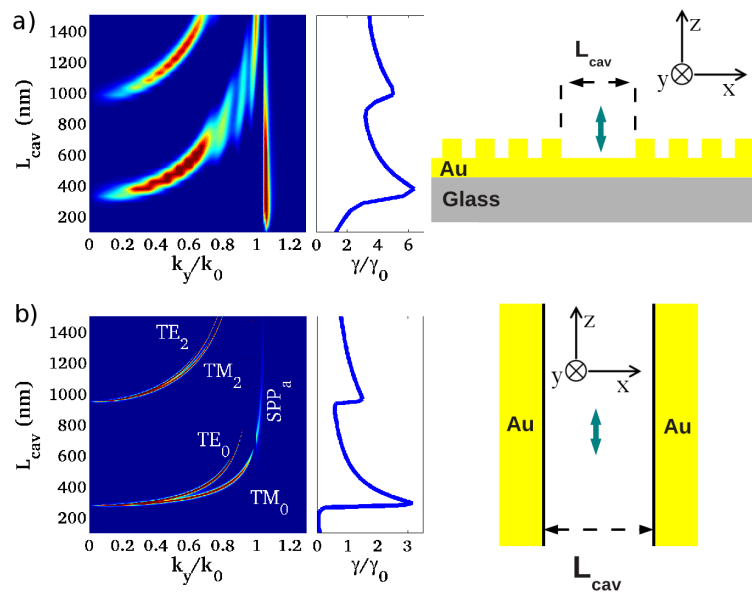


Figure 2.7: a) Power dissipated by a dipolar emitter inside the plasmonic cavity, as a function of cavity length L_{cav} and in plane wavevector along the cavity axis k_y/k_0 . The glass/gold/air slab contribution is subtracted to characterize the cavity effect. Inset: Decay rate as a function of the cavity length obtained by integrating the dissipated power over all the k_y/k_0 spectrum range (including the glass/gold/air slab contribution). b) Same as a) for a 1D gold/air/gold cavity. The dipolar emitter is located at the cavity center and parallel to the mirror walls. The 1D cavity modes are indicated on the dispersion curve. SPP_a and SPP_b (see Fig. 2.8b) are gap plasmons resulting from the coupling between the gold/air SPP supported by the two mirrors (note that the photonic guided TM_0 mode continuously evolves to the gap plasmon SPP_a when the cavity size increases) [Feigenbaum 2007].

To this aim, we first calculate the power $P(k_y)$ dissipated by a dipolar emitter as a function of the in-plane wavevector k_y along the invariant axis, as shown in Fig. 2.7 for a vertical dipole and in Fig. 2.8 for a horizontal dipole. These calculations are performed by numerically evaluating the 2D-Green's dyad associated to the cavity [Lévêque 2006, Colas des Francs 2009b, Barthes 2011, Marty 2012]. In order

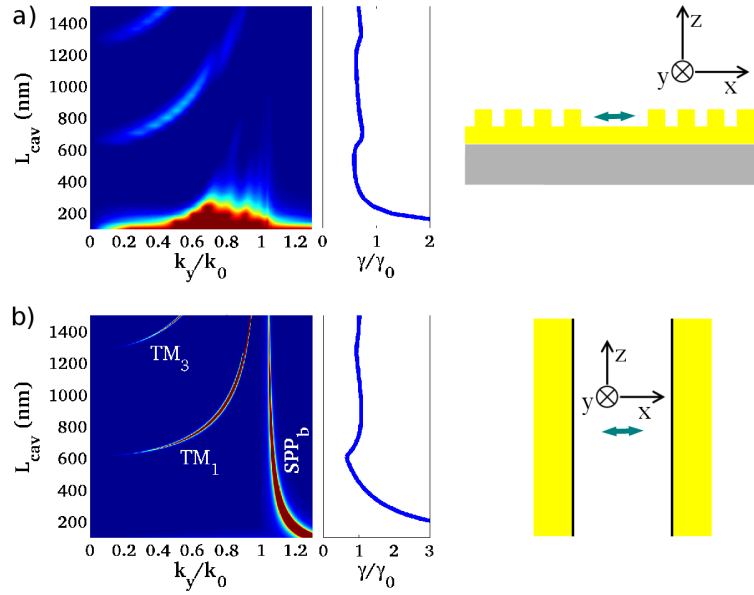


Figure 2.8: Same as Fig. 2.7 for a dipolar emitter perpendicular to the mirror walls.

to focus on the role of the cavity on the emission process, we subtracted the glass/gold/air slab contribution (no grating). For a given cavity size L_{cav} , the main contribution to the dissipated power appears at a given wavevector k_y , associated to a cavity mode. Thus the dissipated power is strongly increased by coupling to the cavity modes, as expected. The total decay rate at the center of the cavity is then computed by integrating the dissipated power over the whole wavevector spectrum for each cavity size (see the insets of Figs. 2.7(a) and 2.8(a)). Recalling that SPP wavelength is $\lambda_{SPP} = \lambda_{em}/n_{SPP} = 645$ nm, we observe that the fluorescence decay rate increases for cavity length in close proximity of odd multiples of $\lambda_{SPP}/2$. Precisely, following Ref.[Weeber 2007b], the dispersion relation of the cavity opened between two Bragg mirrors is better described as a function of the parameter $\delta = L_{cav} - \Lambda + W$ representing the excess of size of the cavity as compared to the mirror period. We check that new cavity modes appear for $\delta \approx (2k + 1)\lambda_{SPP}/4$ with $k = 1, 2, \dots$, as expected.

It is interesting to compare the behaviour of the in-plane plasmonic cavity to a 1D metal/insulator/metal cavity [Worthing 2001, Steiner 2008, Hoogenboom 2009], as presented on Fig. 2.7(b). We observe strong similarities since plasmonic cavity confines a surface wave in direct analogy with 1D optical microcavity that confines a bulk wave. The difference is that the SPP is naturally confined near the metal surface, whereas the 1D modes are delocalized along two directions.

The largest emission rate enhancement is observed for a dipolar emitter oriented parallel to the mirrors (Fig. 2.7). In case of SPP cavity, it also corresponds to an orientation perpendicular to the slab surface, in agreement with the SPP polarization

. Emission enhancement occurs due to the emission coupling to even cavity modes, namely TM_0/TE_0 and TM_2/TE_2 in 1D cavity [Worthing 2001, Hoogenboom 2009] and their plasmonic counterparts in the planar cavity. These modes present an antinode at the cavity center so that they are efficiently excited by the dipolar emitter. Note that only one polarization is allowed in the SPP cavity since it confines the polarised SPP sustained by the substrate/gold/air slab (TM polarised with respect to the slab orientation, that is E_z electric field corresponding to TE mode of the 1D cavity).

A dipolar emitter oriented perpendicular to the mirrors couples weakly to odd cavity modes so that it results in a weak modification of its decay rate, except for small cavity sizes (Fig. 2.8). Although we observe similar behaviours at short cavity length for a dipole coupled to 1D and planar cavities, it comes from different processes (Fig. 2.8a and b). In a 1D cavity, the coupling originates from a large transfer to the non radiative gap plasmon SPP_b leading to a fluorescence quenching. Differently, we observe a strong power dissipation spanning a large wavevector range in the plasmonic case (Fig. 2.8a). This indicates an efficient scattering of the plasmon field by the ridges leading to an increase of the *radiative* rate. Note that this occurs around $0.6 \leq k_y/k_0 \leq 1$ corresponding to the angular range for which the reflectors are inefficient as seen in Fig.2.5(b). The peak near $L_{cav} \approx 270$ nm (corresponding to full grating condition $\delta = 0$) and $k_y/k_0 = 0.6$ is related to the particular point in Fig. 2.5(b) below which no Bloch mode is supported. Last, we observe a very weak decay rate modification in the SPP cavity for a dipolar emitter oriented along the y-axis (not shown).

2.2.2 Single molecule fluorescence lifetime imaging

Figure 2.9 depicts the setup utilized for scanning confocal fluorescence lifetime imaging (confocal FLIM) of single molecules spread into a plasmonic cavity. Dye molecules (DiD, Invitrogen, $\lambda_{em} = 670$ nm) were dispersed in a polymethylmethacrylate (PMMA, toluene solvent) solution at a nanomolar concentration in order to obtain approximatively less than one molecule per μm^2 on the sample. A 35 nm thick dye-doped PMMA film is spin-coated on the plasmonic cavity. Prior to the dye-doped polymer matrix, a 30 nm thick SiO_2 film was deposited by plasma sputtering. This spacer avoids fluorescence quenching near the gold film. Each distributed Bragg mirror consists of six gold ridges (width $W = 140$ nm, height $h = 50$ nm) periodically separated by $\Lambda = 250$ nm. This period was taken as the half SPP wavelength of the glass/gold(50 nm)/ SiO_2 (30 nm)/PMMA(35 nm)/air multilayer system ($n_{SPP} = 1.27$, $\lambda_{SPP} = 526$ nm at the emission wavelength $\lambda_{em} = 670$ nm).

Single molecule detection is performed using the same home-built scanning confocal microscope described in the first section. We added a $\lambda/4$ wave-plate in order

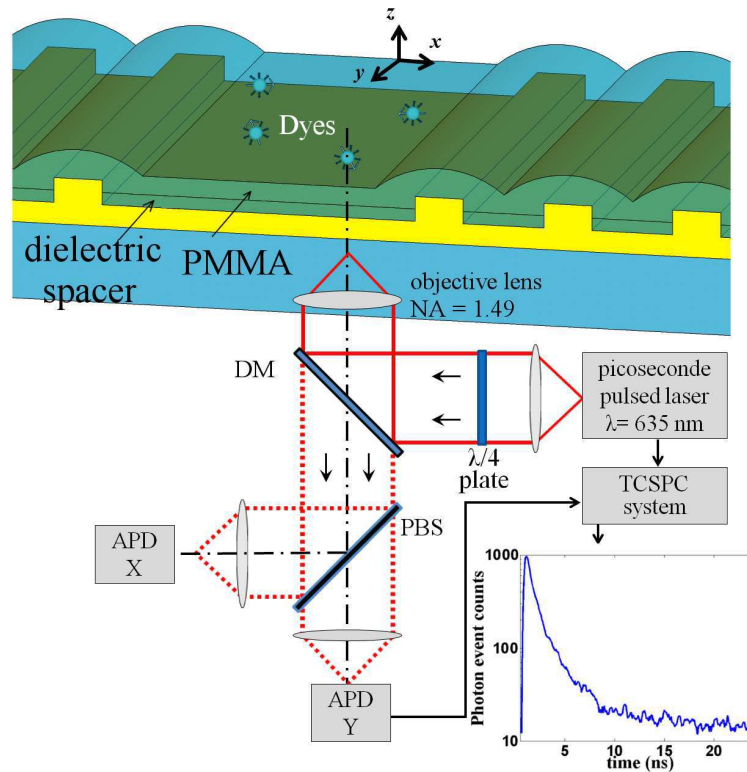


Figure 2.9: Confocal FLIM setup. Dye molecules randomly deposited into a plasmonic cavity are excited with a circularly polarised laser beam. Fluorescence emission is divided by a polarised beam splitter (PBS) and collected on two APDs (*Excelitas Technologies SPCM-AQRH-15*). APD-Y is connected to a time-correlated single photon counting card (TCSPC, *Picoquant-PicoHarp 300*) for fluorescence decay acquisition (inset).

to excite the fluorescent molecules with a circularly polarised light. Therefore all in-plane and out-of-plane oriented dye molecules are excited. The x- and y-polarised photoluminescence are detected on two different APDs, leading to two simultaneous image acquisitions. The x-polarised signal detected on the APD-X records the gold photoluminescence background signal used to locate the position of the grating since the signal is enhanced at the ridges [Kim 2008]. Last, we measured fluorescence lifetime of individual molecules as a function of the cavity size and the molecule position into the cavity.

Figure 2.10 shows a time-correlated single-photon count (TCSPC) histogram (green scatter) recorded from a single dye located inside a cavity. The instrument response function (IRF) of the microscope (black curve) is used for a bi-exponential reconvolution fitting procedure to evaluate the lifetime trace (red curve). The small lifetime component (dozens of picoseconds) is attributed to the background signal [Pic 2010], notably gold photoluminescence. The long lifetime component corresponds to the fluorescence lifetime of the dye molecule. The FWHM of the IRF

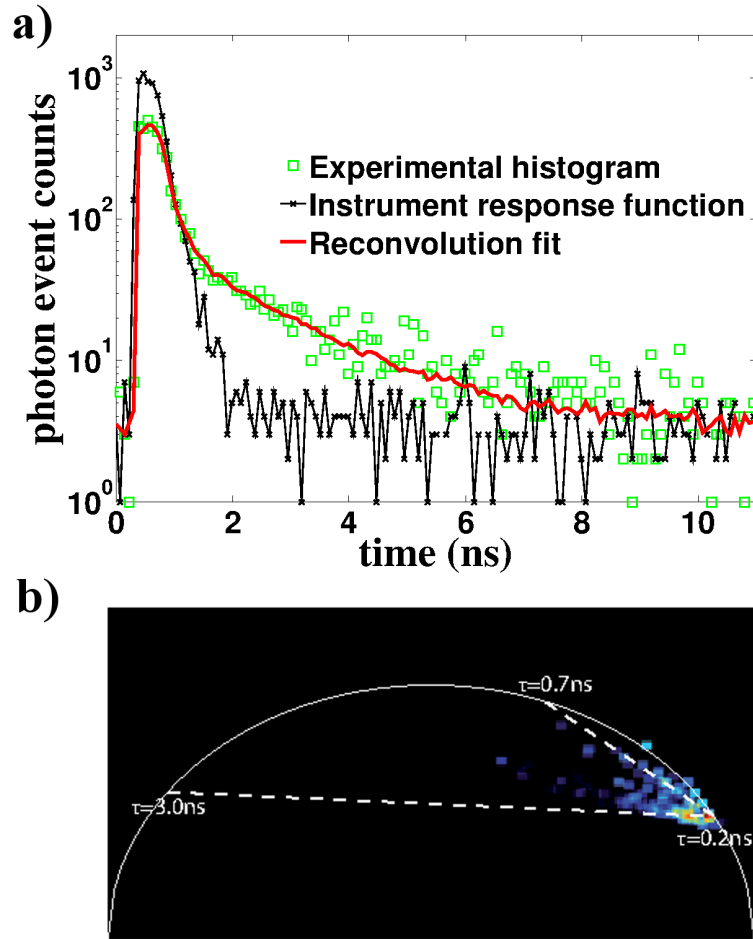


Figure 2.10: a) Green scattered points: TCSPC histogram recorded for a single dye inside a cavity. Black curve: Instrument response function (IRF) of the microscope. Red curve: Result of the reconvolution fitting procedure. b) Polar representation of the fluorescence lifetime. Each point refer to a single molecule lifetime measurement. The right part of the figure corresponds to low lifetime whereas the left part corresponds to long lifetimes

histogram is measured to 450 ps and defines the lower limit for lifetime measurement.

Overall, we have measured the fluorescence lifetime of 137 molecules randomly spread into plasmonic cavities with length ranging from 200 nm to 1.4 μm . Since the gold photoluminescence renders difficult the measurement of the lifetime, we cross-check our measurements using a polar representation (see Fig. 2.10b). In this representation, each point is defined by its (u,v) coordinates which are the cosine and sine transforms of the fluorescence intensity decay [Leray 2012]. Single exponential decay are located on the semi-circle with long lifetime on the left and short lifetime on the right of the circle. In case of bi-exponential behavior, as here, each measure is represented by a point inside the semi-circle. By plotting a

line that joins the experimental measure and short lifetime, we can estimate the long fluorescence lifetime and the respective contribution of each component. This method avoids any fitting procedure and leads to robust evaluation of the lifetimes. In the present case, we observe an important contribution of the short lifetimes but we also confirm the value achieved using a standard fitting procedure with fluorescence lifetime ranging from 0.7 ns to 3 ns. Note that the polar representation and fitting procedure are independant methods. Finally, we estimate the errors on the measured fluorescence lifetime to 200 ps.

The photodynamic of individual dye molecules located into a planar cavity depends on several parameters; namely their orientation, position (distance to the mirror but also altitude), and the length of the cavity. In the following, we try to identify the main trends. To this purpose, we compare the measured lifetime to numerical simulations. For the numerical simulations, we considered two distributed Bragg mirrors made of 6 gold ridges ($W = h = 50$ nm, $\Lambda = 250$ nm) deposited on a 50 nm thick gold film and supported on a glass substrate. The main difference is related to the multilayer system used in the simulation. In order to keep the computing time reasonable, we consider three layers, namely glass/gold(50 nm)/effective medium where the effective medium has an optical index fixed to $n_{above} = 1.2$ since it leads to a similar SPP effective index $n_{SPP} = 1.27$ than the glass/gold/SiO₂/PMMA/air multilayer system. The SPP propagation length is however underestimated using this effective medium ($L_{spp} = 1.9$ μ m instead of $L_{spp} = 5$ μ m). In first approximation, this difference can be safely disregarded since we demonstrate recently that the surface plasmon coupled emission rate does not depend on the propagation length [Barthes 2011, Barthes 2013]. We considered a dipolar emitter 25 nm above the gold film.

Figure 2.11 shows the decay rate calculated as a function of cavity size and molecule position for three emitters orientations. We observe oscillations typical from coupling to the cavity modes, similar to what was already observed in a 1D cavity [Hoogenboom 2009]. As already pointed out, the largest decay rate are obtained for a vertical emitter (Fig. 2.11c).

Figure 2.12(a) shows the measured lifetimes as a function of the cavity size. The dispersion of the measurements is due to both the position and the orientation of the dye molecules. 75 more measurements were also performed for molecules far from the cavities (*i.e.* embedded within the PMMA matrix in the glass/gold/SiO₂/PMMA/air multilayer system) and are taken as reference measurements. The calculated reference lifetime is $\tau_{ref}/\tau_0 = 0.51$ in agreement with the experimental one estimated to $\tau_{ref}/\tau_0 = 1.43/2.6 = 0.55$ where $\tau_0 = 2.6$ ns was measured in a PMMA matrix [Hoogenboom 2009]. In the following, fluorescence lifetimes are normalized with respect to this average reference lifetime τ_{ref} to focus on the plasmonic cavity role. In Fig. 2.12(b), we compare the measured and calculated lifetimes. In order to assess a first trend, we averaged

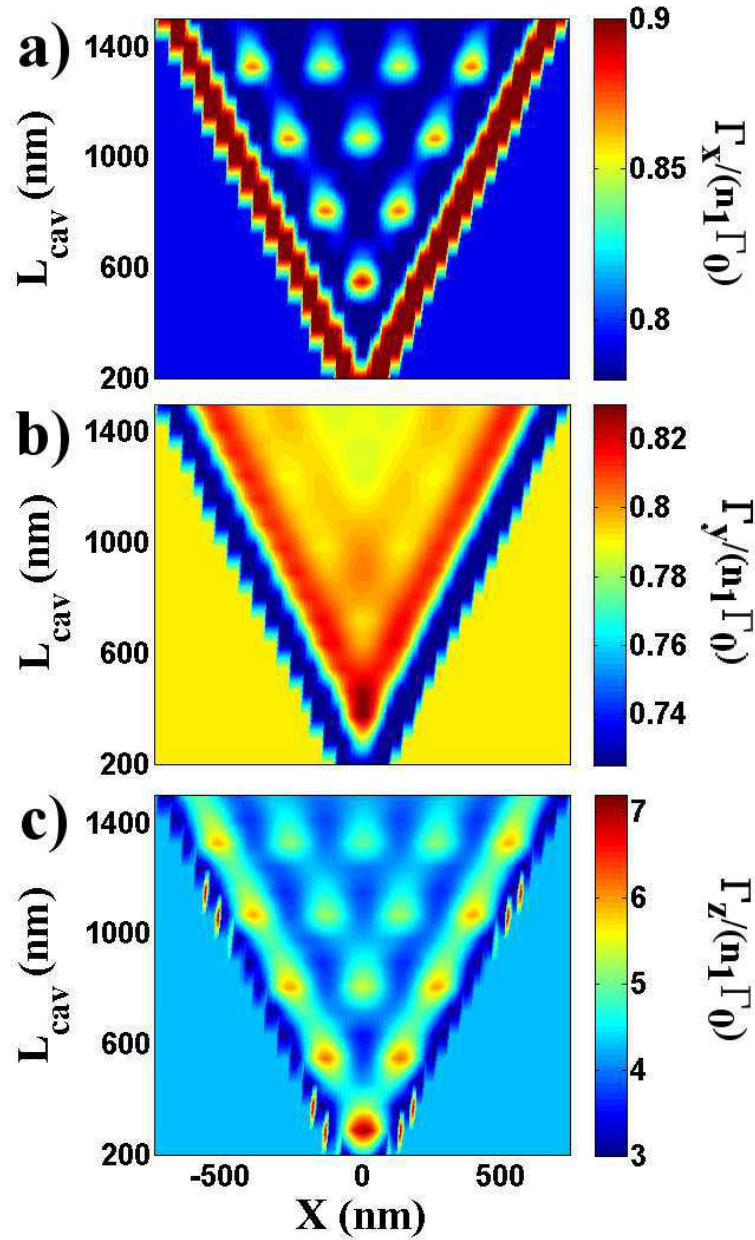


Figure 2.11: a-c) Normalized fluorescence decay rate calculated as a function of cavity size L_{cav} and molecule position for x-(a),y-(b) and z-(c) oriented emitter. Decay rates are normalized with respect to their free-space value Γ_0 . The value outside the cavity refers to the decay rate in absence of the gold gratings.

the lifetimes for each cavity size. The experimental curve is in qualitative agreement with the calculated one with variations related to the coupling to cavity modes.

We also plot the normalized decay rate ($\Gamma_{cav}/\Gamma_{ref} = \tau_{ref}/\tau_{cav}$) distribution as a function of molecule's distance from the mirror in Fig. 2.13. We observe large dispersion of the measured decay for a given distance to the mirror since resonant

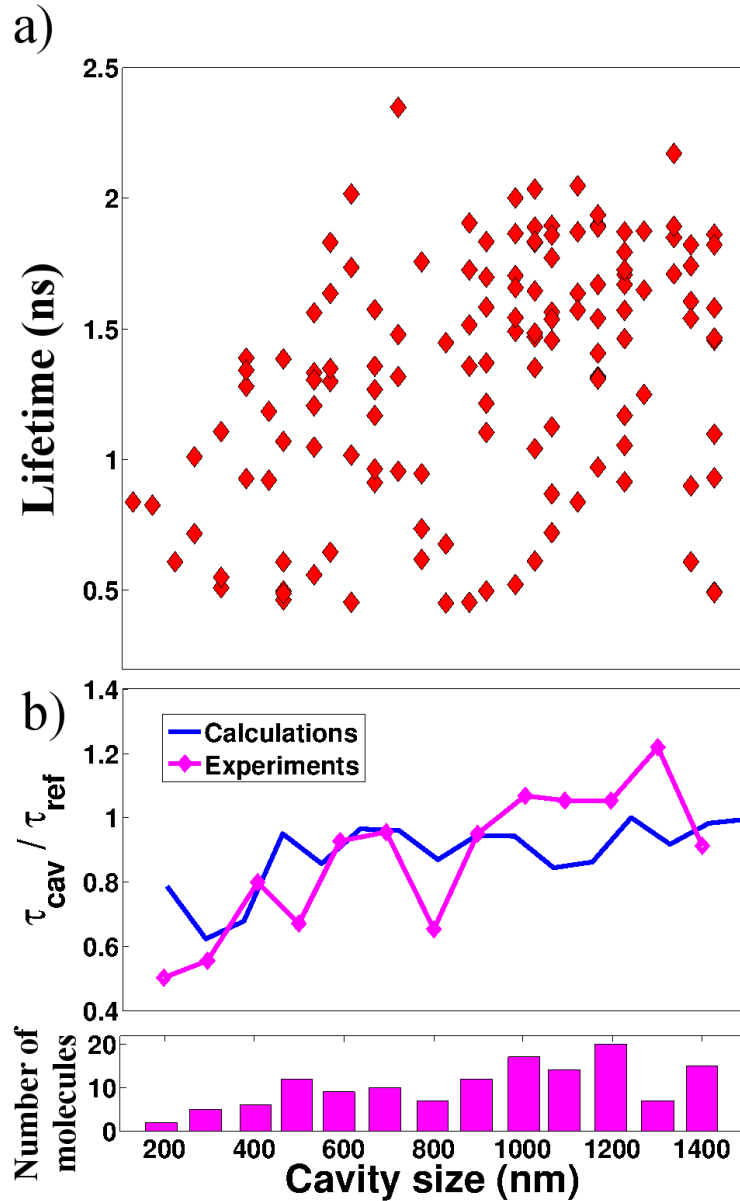


Figure 2.12: a) Fluorescence lifetime as a function of the cavity size. b) Distribution of the lifetimes measured inside the cavity (red bars) or far from the cavity (blue bars). c) Average lifetime as a function of the cavity size (purple curve) The blue curve is calculated assuming a mean molecule position $z = 25$ nm above the metal film. Lifetimes are normalized with respect to the reference measured ($\tau_{ref} = 1.43$ ns) or calculated ($\tau_{ref}/\tau_0 = 0.51$) far from the cavity. The bottom panel depicts the number of considered molecules for each cavity size.

and non resonant cavities length are involved. The average decay (solid curves) shows small oscillations around $\Gamma_{cav}/\Gamma_{ref} = 1$ that are reminiscences of nodes and antinodes of the planar cavity modes (see Fig. 2.11). We also represent the maximum and minimum decay rates expected for a z - and x -oriented dipole,

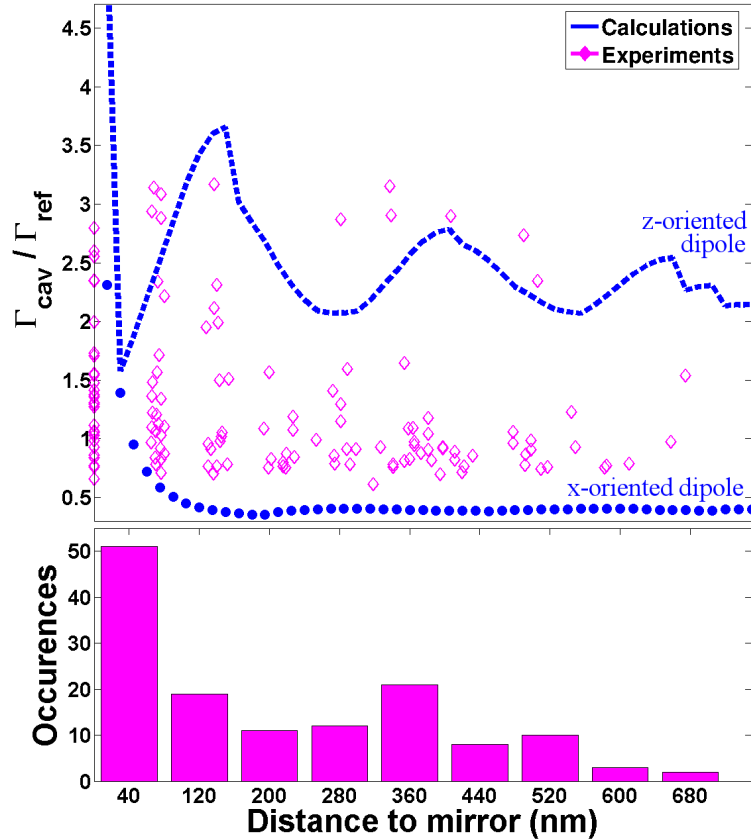


Figure 2.13: Distribution of the fluorescence decay rate as a function of distance to the closest Bragg mirror for all cavity sizes (purple diamonds). The dotted (dashed) curve is the minimum (maximum) calculated decay rate for a x-oriented (z-oriented) dipole.

respectively. This qualitatively reproduces the measured lifetime dispersion. The discrepancies are attributed to the simplifications used in our model.

Figure 2.14 presents the evolution of the decay rate as a function of the position inside a resonant $1.1 \mu\text{m}$ cavity. The observed dispersion is again in agreement with the numerical simulations. Maximum decay rate enhancement is $\Gamma/\Gamma_{ref} = 2.3$ as compared to a flat gold film. This corresponds to an enhancement factor (Purcell factor) of $F_P = \Gamma/\Gamma_0 = (\Gamma/\Gamma_{ref}) \times (\Gamma_{ref}/\Gamma_0) \sim 2.3/0.55 = 4.2$. It could reach $F_P \approx 7$ in a single mode cavity (see Fig. 2.11c). This reveals the capability of a planar plasmonic cavity to control fluorescent emission. Finally, we calculate the radiative contribution to the total decay rate (red dashed curve) since light extraction is an important aspect to consider [Mallek-Zouari 2010]. This is estimated by vanishing the imaginary part of the dielectric function of gold. We estimate the quantum efficiency to $\Gamma_{rad}/\Gamma_{tot} \approx 90\%$ so that high extraction efficiency is expected from such planar plasmonic cavity. This originates from SPP decoupling into the substrate [Barthes 2011].

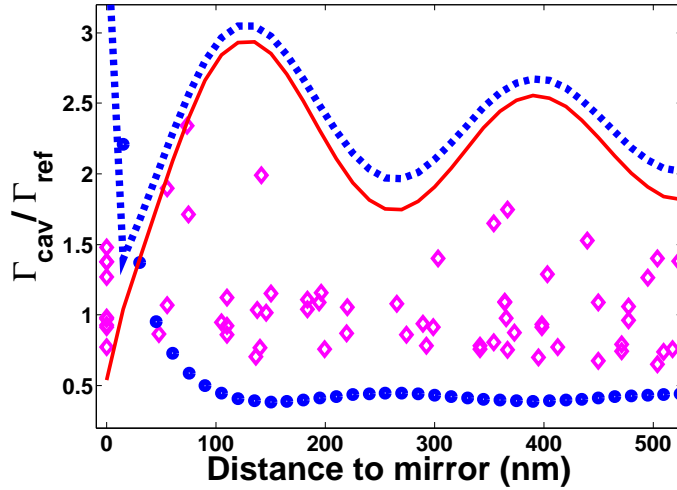


Figure 2.14: Normalized decay rates in a cavity shown as the purple diamond with a $L_{cav} = 1.1 \mu\text{m}$ as function of the distance to the mirror. Decay rates calculated for a z-oriented (dashed curve) and a x-oriented (dotted curve) dipole are also shown. The calculated radiative decay is plot for a z-oriented emitter (solid red curve).

2.3 Conclusion

To summarize, we have demonstrated at the single molecule level that plasmonic planar cavity permits emission control thanks to surface wave confinement. This is in direct analogy to fluorescence emission governed by bulk mode confinement in an optical dielectric microcavity . We first studied the effect of SPP mirrors on surface plasmon coupled emission by leakage radiation microscopy. We have demonstrated that the mirrors remains efficient when excited by a localized SPP source at room temperature. Then, we measured the fluorescence lifetime into in-plane SPP cavities and interpreted the modifications with the help of numerical simulations. This leads to a clear understanding of the role of the cavity modes in the emission mechanism. We estimated a high decay rate enhancement (up to 7 in a $\lambda_{SPP}/2$ cavity for a z-oriented dipole). Finally, we have shown that efficient radiation decoupling of the SPP into the substrate leads to high apparent quantum yield of great interest for light extraction. The design of the planar cavity in order to improve the collection rate efficiency is a work in progress in collaboration with the GEMaC group in Versailles (project ANR QDotics). As an added value, let us also note that the emitters located inside the SPP cavity are accessible for external manipulation with *e.g.* optical tweezers or an AFM tip.

Mie Plasmons: Modes Volume, resonance quality and Purcell factor

Contents

3.1	Quasi-static approximation	38
3.1.1	Dipolar mode	38
3.1.2	Multipolar modes	43
3.1.3	β -factor	47
3.2	Mie plasmon	48
3.2.1	Resonance quality	49
3.2.2	Effective volume	52
3.3	Conclusion	56

In the previous chapter, we have shown that optical microcavity design can be transpose to delocalized SPP. Although SPP presents subwavelength confinement in the direction transverse to the metal film, it has a diffraction limited confinement in the two other directions. It is therefore interesting to investigate full 3D subwavelength confinement thanks to localized surface plasmon.

In this chapter, we describe coupling between a dipolar emitter and a LSP in analogy to spontaneous emission in optical microcavity. Indeed, spontaneous emission rate in complex systems follows the Fermi's golden rule. However, for describing the coupling to a cavity mode, the Purcell factor is usually preferred since it clearly introduces the cavity resonance quality factor Q and the mode extension V_{eff} on which coupling remains efficient, bringing therefore a clear physical understanding of the coupling process. Moreover, the knowledge of Q/V_{eff} ratio is crucial for achieving strong coupling regime [Trügler 2008, Savasta 2010] or for designing plasmonic nanolasers [Protsenko 2005, Noginov 2009, Stockman 2010].

In this context, we propose to determine the quality factor and mode volume of LSP supported by a metal nanosphere. In section 3.1, we consider the quasi-static behaviour and a Drude metal since it leads to simple analytical expression with a

clear physical meaning.

In the second section, we will consider exact behaviour thanks to Mie calculations. This will lead notably to discuss about the definition and the validity of the mode volume.

3.1 Quasi-static approximation

In this section, quasi-static approximation on Drude metal is performed for characterizing the localized surface plasmons supported by a metallic spherical nanoparticle. The role of Joule losses and far-field scattering in the coupling mechanism are introduced and discussed with simple physical understanding. We estimate the quality factor Q_n and define the effective volume V_n of the n^{th} mode in a such a way that coupling strength with a neighbouring dipolar emitter is proportional to the ratio Q_n/V_n (in agreement with the Purcell factor expression).

In section 3.1.1, we focus on the dipolar mode and present in details the derivation of its quality factor and effective volume. We extend our approach to each mode of the particle in section 3.1.2. Finally, we discuss the coupling efficiency to one of the particle modes in the last section. For the sake of simplicity, all the analytical expressions are derived assuming a particle in air and dipolar emitter perpendicular to the particle surface. The generalisation to arbitrary emitter orientation and a background medium of optical index n_B is provided in the appendix A.

3.1.1 Dipolar mode

We first characterize the dipolar mode of a spherical particle. For sphere radius R small compared to the excitation wavelength $\lambda = 2\pi c/\omega$, the electric field is considered uniform over the metallic particle. The metallic particle is polarized by the incident electric field \mathbf{E}_0 and behaves as a dipole

$$\mathbf{p}^{(1)}(\omega) = 4\pi\epsilon_0\alpha_1(\omega)\mathbf{E}_0, \quad (3.1)$$

$$\alpha_1(\omega) = \frac{\epsilon_m(\omega) - 1}{\epsilon_m(\omega) + 2}R^3, \quad (3.2)$$

where α_1 is the nanoparticle quasi-static (dipolar) polarisability and ϵ_m is the metal dielectric constant. The dipole plasmon resonance appears at ω_1 such that $\epsilon_m(\omega_1) + 2 = 0$. In case of Drude metal, the dipolar resonance is $\omega_1 = \omega_p/\sqrt{3}$ with ω_p the bulk metal plasma angular frequency. However, expression (3.2) does not satisfy the optical theorem (energy conservation). It is well-known that this apparent paradox is easily overcome by taking into account the finite size of the particle and leads to define the effective polarisability [Wokaun 1982]:

$$\alpha_1^{eff} = \left[1 - i \frac{2k^3}{3}\alpha_1\right]^{-1} \alpha_1, (k = 2\pi/\lambda). \quad (3.3)$$

The corrective term ($2k^3\alpha_1/3$) is the so-called radiative reaction correction and microscopically originates from the radiation emitted by the charges oscillations induced inside the nanoparticle by the excitation field [Jackson 1998]. If the dielectric constant of the metal follows a Drude model,

$$\varepsilon_m = 1 - \frac{\omega_p^2}{\omega^2 + i\Gamma_{abs}\omega} \quad (3.4)$$

where ω_p and Γ_{abs} refers to metal plasma frequency and Ohmic loss rate, respectively, then the dipolar polarisability presents a simple shape near the resonance ω_1 [Carminati 2006]

$$\varepsilon_m = 1 - \frac{\omega_p^2}{\omega^2 + i\Gamma_{abs}\omega}; \quad (3.5)$$

$$\alpha_1^{eff}(\omega) \underset{\omega_1}{\sim} \frac{\omega_1}{2(\omega_1 - \omega) - i\Gamma_1} R^3, \quad (3.6)$$

$$\Gamma_1 = \Gamma_{abs} + \frac{2(k_1 R)^3 \omega_1}{3}, (k_1 = \omega_1/c). \quad (3.7)$$

Here Γ_1 is the decay rate of the particle dipolar mode, and includes both the Joule (Γ_{abs}) and radiative [$\Gamma_1^{rad} = 2(k_1 R)^3 \omega_1/3$] losses rates (for the sake of clarity, we use lowercase notation γ for the emitter decay rates and uppercase Γ for the quantities associated to the metallic particle).

Quality factor The dipolar response can be described by either the extinction efficiency Q_{ext} , proportional to $Im(\alpha_1)$, or scattering efficiency Q_{scatt} , proportional to $|\alpha_1|^2$:

$$Q_{ext}(\omega) = \frac{4k}{R^2} Im[\alpha_1^{eff}(\omega)] \quad (3.8)$$

$$\begin{aligned} &\propto_{\omega_1} \frac{1}{(\omega - \omega_1)^2 + (\Gamma_1/2)^2}, \\ Q_{scatt}(\omega) &= \frac{8}{3R^2} k^4 |\alpha_1^{eff}(\omega)|^2 \quad (3.9) \\ &\propto_{\omega_1} \frac{1}{(\omega - \omega_1)^2 + (\Gamma_1/2)^2}. \end{aligned}$$

As a consequence, the dipolar resonance follows a Lorentzian profile, peaked at the angular frequency ω_1 and a full width at half maximum (FWHM) Γ_1 . The quality factor of this resonance is therefore:

$$Q_1 = \frac{\omega_1}{\Gamma_1}. \quad (3.10)$$

As an example, we consider a 50 nm silver sphere in air. The Drude model parameters are $\hbar\omega_p = 9.1$ eV and $\hbar\Gamma_{abs} = 18$ meV that lead to a resonance peak at $\hbar\omega_1 = 5.2$ eV ($\omega_1 = 7.98 \cdot 10^{15}$ Hz, $\lambda_1 = 236$ nm) and radiative energy $\hbar\Gamma_1^{rad} = 1$ eV ($\Gamma_1^{rad} = 1.5 \cdot 10^{15}$ Hz). The quality factor is then $Q_1 = 5$. Note

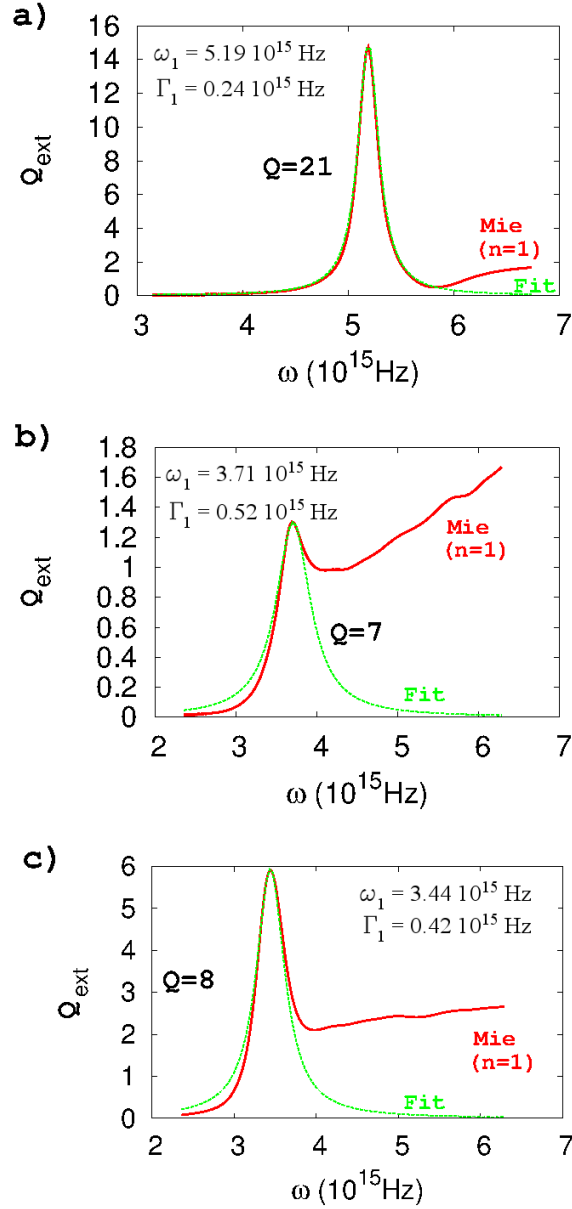


Figure 3.1: Extinction efficiency for the dipolar resonance calculated keeping only the dipolar mode ($n = 1$) in the Mie expansion and using experimental value for the metal dielectric constant [Johnson 1972]. a) Silver particle in air. b) Gold particle in air. c) Gold particle in PMMA (optical index $n_B = 1.5$). The particle radius is $R = 25$ nm for each case. Fit refers to a Lorentzian fit using parameters indicated on the figure.

that the metal optical properties are better described when including the bound electrons in the Drude model: $\epsilon_m = \epsilon_\infty - \omega_p^2/(\omega^2 + i\Gamma_{\text{abs}}\omega)$, ($\epsilon_\infty = 3.7$ for silver, see also the appendix A). In that case, we obtain $\hbar\omega_1 = 3.74$ eV ($\omega_1 = 5.7 \cdot 10^{15}$ Hz, $\lambda_1 = 330$ nm), $\hbar\Gamma_1^{\text{rad}} = 0.13$ eV ($\Gamma_1^{\text{rad}} = 1.97 \cdot 10^{14}$ Hz) and $Q_1 = 24$.

Although Drude model qualitatively explains the shape of the resonance, a more representative value of the quality factor can only be determined using tabulated data for the dielectric constant of the metal and Mie formalism to express the optical response of the particle. In the section 3.2, we will discuss in details the Mie description of the particle properties. It is however useful to give an order of magnitude for Q_1 as a reference value. The extinction efficiency associated to the dipolar resonance is represented in Fig. 3.1. For silver particle (Fig. 3.1a), the extinction efficiency closely follows a Lorentzian shape, as expected, with a quality factor $Q_1 = 21$, in good agreement with the value obtained using Drude model (with the contribution of the bound electrons included). In case of gold, the resonance profile is not well defined due to interband transitions for $\omega > 4.10^{15} \text{ Hz}$ but a quality factor of $Q_1 = 7$ can be estimated (Fig. 3.1b). Figure 3.1c) represents the extinction efficiency for a gold particle embedded in polymethylmethacrylate (PMMA). This leads to a small redshift of the resonance, avoiding therefore the resonance disturbance by interband absorption [Sonnichsen 2002]. We recover partly the Lorentzian profile with a quality factor reaching $Q_1 = 8$.

Effective volume When we consider a quantum emitter coupled to a dipolar particle, the emitter decay rate can be approximated at very short distances d as [Colas des Francs 2005, Carminati 2006, Colas des Francs 2008]:

$$\frac{\gamma_1^\perp}{\gamma_0} \sim \frac{6}{k^3 z_0^6} \text{Im}(\alpha_1), \quad (3.11)$$

for a dipole emitter orientation perpendicular to the nanoparticle surface ($z_0 = R + d$ is the distance to the particle center). Using Eq. 3.6, we obtain, in case of a dipolar emitter emission tuned to the dipolar particle resonance ($\lambda = \lambda_1 = 2\pi c/\omega_1$)

$$\frac{\gamma_1^\perp}{\gamma_0} \sim \frac{6\omega_1 R^3}{\omega_1 k_1^3 z_0^6 \Gamma_1} \sim \frac{3}{4\pi^2} \lambda_1^3 \frac{R^3}{\pi z_0^6} Q_1. \quad (3.12)$$

In order to determine the dipolar mode effective volume, we now identify the coupling rate γ/γ_0 to the Purcell factor assuming $n_B = 1$

$$\frac{\gamma_1^\perp}{n_B \gamma_0} = \frac{3}{4\pi^2} \left(\frac{\lambda_1}{n_B} \right)^3 \frac{Q_1}{V_1^\perp}, \quad (3.13)$$

so that we obtain

$$V_1^\perp(z_0) = \frac{\pi z_0^6}{R^3}. \quad (3.14)$$

This is in full agreement with the expression recently derived by Greffet *et al.* from the optical impedance of the nanoparticle antenna [Greffet 2010]. For a 25 nm radius sphere in air, we estimate the mode effective volume

$V_1^\perp(z_0 = 35 \text{ nm}) = 3.7 \cdot 10^{-4} \mu\text{m}^3 = (72 \text{ nm})^3$ for an emitter 10 nm away from the particle surface. That reveals the strongly subwavelength confinement of the LSP.

Unlike here, usual definition of the mode effective volume does not include the emitter position. As mentioned in Chapter 1, Purcell factor expression (Equation 3.13) is only valid for an emitter located at the maximum field position (here, $z_0 = R$) and aligned with the field polarization (\perp)

$$V_1^\perp = \pi R^3. \quad (3.15)$$

This gives an estimation of the mode volume. We discuss a rigorous definition of V_{eff} later but we can already observe that it is strongly sub-wavelength. For instance, for a $D = 50 \text{ nm}$ silver particle resonant at $\lambda \approx 360 \text{ nm}$ we obtain $V^\perp = 1.1 \cdot 10^{-3} (\lambda/n_B)^3$.

At this point, we have to take care that the dipolar LSP mode is 3-fold degenerated (two lobes aligned along x-, y-, or z-axis). As a consequence, we have to include the 3-fold degenerated mode in the effective volume definition.

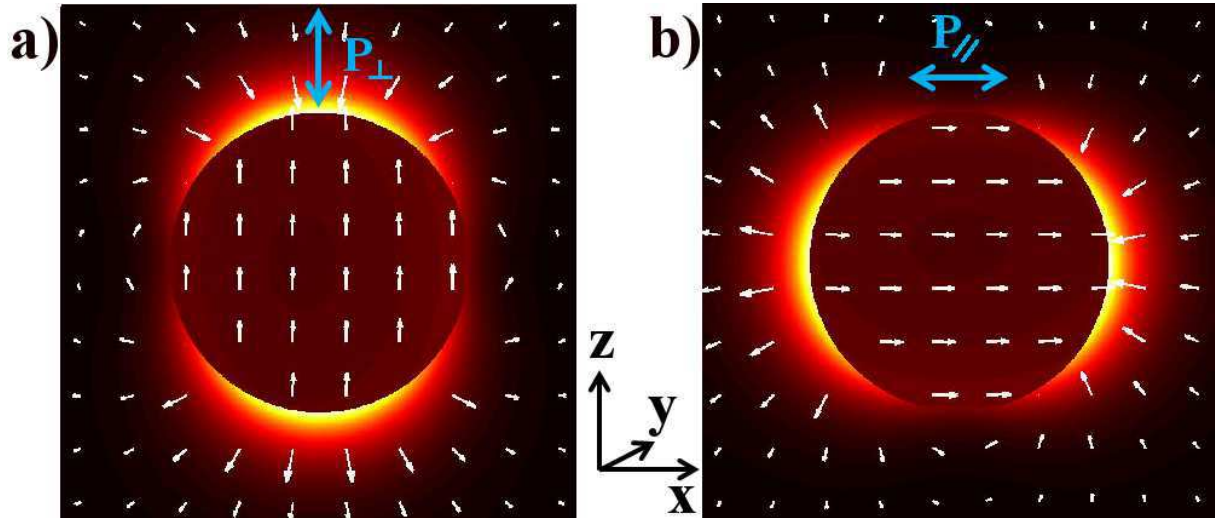


Figure 3.2: Schematic view of an emitting dipole (green double arrow) close to the surface of a metal nanoparticle. a) The emitter P_\perp is oriented perpendicularly to the metal surface. b) The emitter P_\parallel is oriented horizontally to the surface.

The figure 3.2 presents the electric field line of the dipole mode with lobes along the z- or x-axis. Let us consider a dipole at the particle surface, at position indicated on the figure ($z_0 = R$). Depending on the dipole orientation, it can excite the LSP with lobes along the z-axis (longitudinal coupling that is the most efficient) or with lobes along x or y-axis (transverse coupling, less efficient). It is therefore useful to consider a randomly oriented dipole so that we can describe coupling to the 3-fold

degenerated modes. This is equivalent to discuss the average decay rate

$$\langle \gamma \rangle = \frac{1}{3}(\gamma_{\perp} + \frac{2}{3}\gamma_{\parallel}) \quad (3.16)$$

leading to a mode volume V_1 such that

$$\frac{1}{V_1} = \frac{1}{3V_{\perp}} + \frac{2}{3V_{\parallel}}. \quad (3.17)$$

This leads (see Appendix A)

$$V_1 = 2\pi R^3 = \frac{3V_0}{2} \quad (3.18)$$

with $V_0 = (4/3)\pi R^3$ the particle volume. This expression is in agreement with the expression derived by Sun and coworkers using a energy description of the mode volume (also in the quasi-static approximation) [Khurgin 2009].

To conclude, the dipolar LSP presents a mode volume of the order of the particle volume and is not diffraction limited. For instance, 50 nm silver particle ($R = 25$ nm) supports a dipolar mode with effective volume $V_1 = 9.8 \cdot 10^4 \text{ nm}^3 = (46 \text{ nm})^3$. This characterizes the strongly sub-wavelength mode confinement and also defines the space zone on which efficient coupling to a dipolar emitter occurs.

3.1.2 Multipolar modes

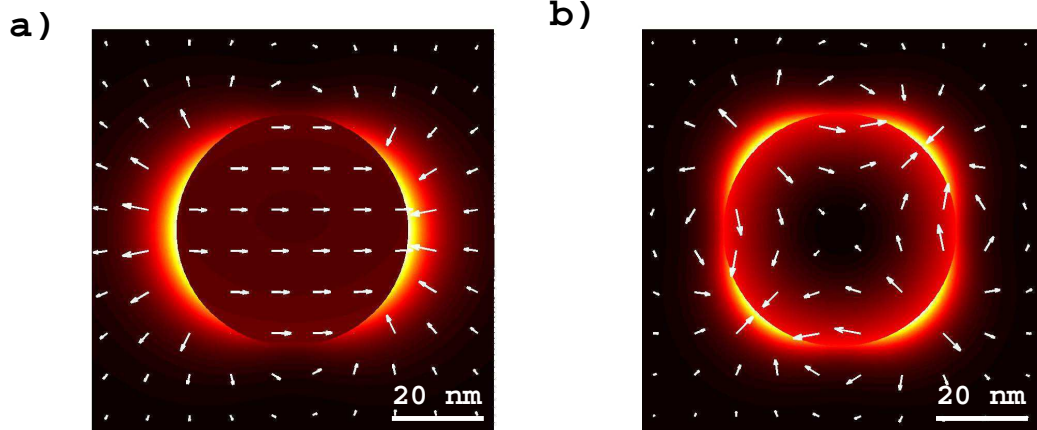


Figure 3.3: a) Dipolar and b) quadrupolar mode profiles of a 50 nm silver sphere, embedded in PMMA calculated using exact Mie expansion. Silver dielectric constant is taken from ref. [Johnson 1972]. Color and arrows refer to electric field intensity and vector respectively.

If the excitation field is generated by a dipolar emitter (fluorescent molecules, quantum dots, ...), it cannot be considered uniform anymore and the dipolar

approximation fails. One needs therefore to consider the coupling strength to high order modes (Fig. 3.3).

The n^{th} multipole tensor moment of the metallic particle is given by:

$$\mathbf{p}^{(n)} = \frac{4\pi\epsilon_0}{(2n-1)!!} \alpha_n \nabla^{n-1} \mathbf{E}_0, \quad (3.19)$$

$$\alpha_n = \frac{n(\epsilon_m - 1)}{n\epsilon_m + (n+1)} R^{(2n+1)}, \quad (3.20)$$

with $(2n+1)!! = 1 \times 3 \times 5 \times \dots \times (2n+1)$ and ∇ is the vector differential operator. As discussed above, the particle dipole moment $\mathbf{p}^{(1)} = 4\pi\epsilon_0\alpha_1\mathbf{E}_0$ is the unique mode excited in an uniform field. However, the dipolar emitter near-field behaves as $1/r^3$ and strongly varies spatially so that higher modes can be excited in the particle.

For a Drude metal, the n^{th} resonance appears at $\omega_n = \omega_p \sqrt{n/(2n+1)}$. Therefore, higher order modes accumulate near $\omega_\infty = \omega_p/\sqrt{2}$. Moreover, as discussed for the dipolar case, quasi-static expression of the n^{th} mode polarisability (Eq. 3.20) does not obey energy conservation. Applying the optical theorem, we can extend the radiative correction to all the spherical particles modes [Colas des Francs 2009a]. This leads to

$$\alpha_n^{eff} = \left[1 - i \frac{(n+1)k^{2n+1}}{n(2n-1)!!(2n+1)!!} \alpha_n \right]^{-1} \alpha_n. \quad (3.21)$$

Quality factors It is now a simple matter to generalize the dipolar mode analysis reported in the previous section to all the particle modes. The n^{th} mode polarisability can be approximated near the resonance. A simple expression for the polarisability is achieved considering a Drude metal:

$$\begin{aligned} \alpha_n^{eff} &\sim \frac{\omega_n}{\omega_n} \frac{\omega_n}{2(\omega_n - \omega) - i\Gamma_n} R^{2n+1}, \\ \Gamma_n &= \Gamma_{abs} + \Gamma_n^{rad}, \\ \Gamma_n^{rad} &= \omega_n \frac{(n+1)(k_n R)^{2n+1}}{n(2n-1)!!(2n+1)!!}, \quad (k_n = \omega_n/c), \end{aligned} \quad (3.22)$$

where Γ_n is the total decay rate of the n^{th} mode, that includes both ohmic losses and radiative scattering. As expected, for a given mode n , the radiative scattering rate $\Gamma_n^{rad} \propto R^{2n+1}$ increases with the particle size since it couples more efficiently to the far-field. For instance, we obtain $\hbar\Gamma_2^{rad} = 39 \text{ meV}$ ($\hbar\Gamma_2^{rad} = 1.8 \text{ meV}$ with $\epsilon_\infty = 3.7$) for the quadrupolar mode of a 50 nm silver particle in air. As expected, the radiative rate of the quadrupolar is strongly reduced compared to the dipolar mode. The quality factor associated to the n^{th} mode is

$$Q_n = \frac{\omega_n}{\Gamma_n} = \frac{\omega_n}{\Gamma_{abs} + \Gamma_n^{rad}}. \quad (3.23)$$

Figure 3.4 details the quality factor the two first modes of a silver sphere in PMMA using tabulated value for ϵ_m . The quadrupolar mode presents a quality factor almost

5 times higher than the dipolar mode since it has limited radiative losses. Indeed, quadrupolar mode poorly couples to the far-field. Finally, similar Q values ($Q_n \approx 50$) are obtained for all the higher modes ($n \geq 3$). Here again, assuming a Drude metal and in the quasi-static approximation, we qualitatively explains this result. Actually, Q factors of high order modes are absorption loss limited ($\Gamma_n^{rad} \ll \Gamma_{abs}$, so called dark modes) and tend to $Q_\infty = \omega_\infty/\Gamma_{abs}$. However this overestimates the mode quality factor ($Q_\infty \approx 207$) as compared to the value deduced using tabulated value for ε_m and exact Mie expansion.

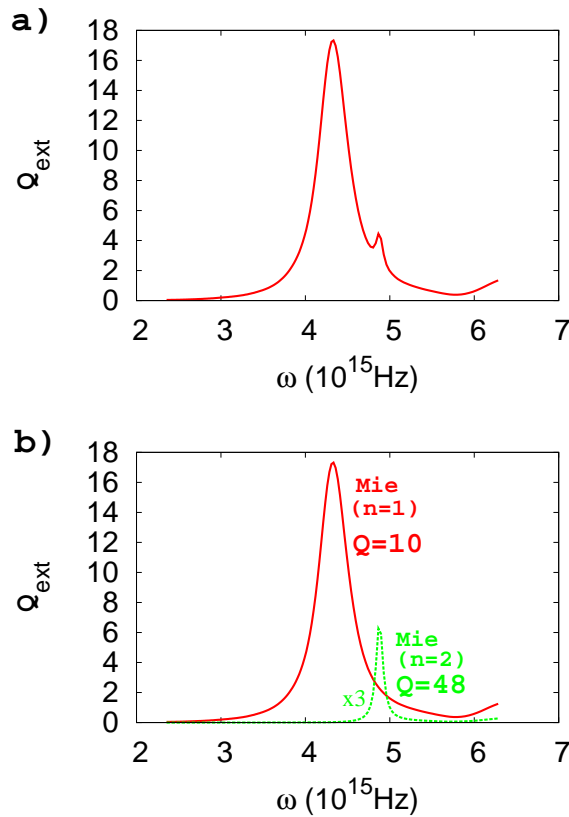


Figure 3.4: a) Extinction efficiency of a silver sphere embedded in PMMA ($R = 25$ nm), calculated using full Mie expansion. b) Contribution of the dipolar ($n=1$) and quadrupolar ($n=2$) mode to the full extinction efficiency. The quality factor is indicated for each mode. Dielectric constant for silver is taken from ref. [Johnson 1972].

Effective volumes Last, we express the *total* decay rate of a dipolar emitter near a spherical metallic particle for very short separation distances ($kz_0 \ll 1$) [Colas des Francs 2008, Colas des Francs 2009a]:

$$\frac{\gamma_{tot}^\perp}{\gamma_0} \approx \frac{3}{2} \frac{1}{(kz_0)^3} \sum_{n=1}^{\infty} \frac{(n+1)^2}{z_0^{(2n+1)}} \text{Im}(\alpha_n^{eff}). \quad (3.24)$$

So that the coupling strength to the n^{th} mode is easily deduced as

$$\frac{\gamma_n^\perp}{\gamma_0} \approx \frac{3}{2} \frac{1}{(kz_0)^3} \frac{(n+1)^2}{z_0^{(2n+1)}} \text{Im}(\alpha_n^{\text{eff}}), \quad (3.25)$$

$$\tilde{\omega}_n \approx \frac{3}{2} \frac{R^{2n+1}}{(k_n z_0)^3} \frac{(n+1)^2}{z_0^{(2n+1)}} Q_n. \quad (3.26)$$

where we have used approximated expression (3.22) for the n^{th} polarisability. The mode effective volume is then straightforwardly deduced from comparison to the Purcell factor (Eq. 3.13)

$$V_n^\perp = \frac{4\pi z_0^{2n+4}}{(n+1)^2 R^{2n+1}}. \quad (3.27)$$

As discussed in the dipolar case, the mode effective volume is generally defined independently on the particle-emitter distance so that it gives an estimation of the mode extension. This is done by evaluating the maximum decay rate available, and for a random emitter orientation. It comes

$$\frac{1}{V_n} = \frac{1}{3V_n^\perp(R)} + \frac{2}{3V_n^\parallel(R)}, \quad (3.28)$$

$$V_n = \frac{9}{(2n+1)(n+1)} V_0, \quad (3.29)$$

where $V_0 = 4\pi R^3/3$ is the metallic sphere volume and V_n^\parallel refers to a dipole parallel to the sphere surface (see Eq. A.11 in appendix, with $\varepsilon_B = 1$). Dipolar and quadrupolar mode volumes are $V_1 = 3/2 V_0$ and $V_2 = 3/5 V_0$, respectively.

The expression (3.29), derived for a Drude metal, quantifies an extremely important property of localized SPPs; their effective volume does not depend on the wavelength and is of the order of the particle volume.

Metallic nanoparticles therefore support localized modes of strongly subwavelength extension. Highest order modes have negligible extension ($V_n \rightarrow 0$ for $n \rightarrow \infty$, see Fig. 3.5). As a comparison, photonics cavity modes are generally limited by the diffraction limit so that their effective volume is at best of the order of $(\lambda/n_B)^3$ (see ref. [Vahala 2003]). Nevertheless, the extremely reduced SPP volume is achieved at the expense of the mode quality factor. It should be noticed that a low quality factor indicates a large cavity resonance FWHM so that emitter-SPP coupling can occur on a large spectrum range.

Note that mode effective volume is generally defined by its energy confinement [Maier 2006](Eq. 1.12). Sun and co-workers used this definition in the quasi-static regime and obtained [Khurgin 2009] $V_n = 6V_0/(n+1)^2$ that is in agreement with our expression for the dipolar mode volume ($V_1 = 1.5V_0$) but leads to slightly different values for other modes (*e.g.* $V_2 \approx 0.67V_0$ instead of $V_2 = 0.60V_0$). Recently, Koenderink showed that defining the mode volume on the basis of energy

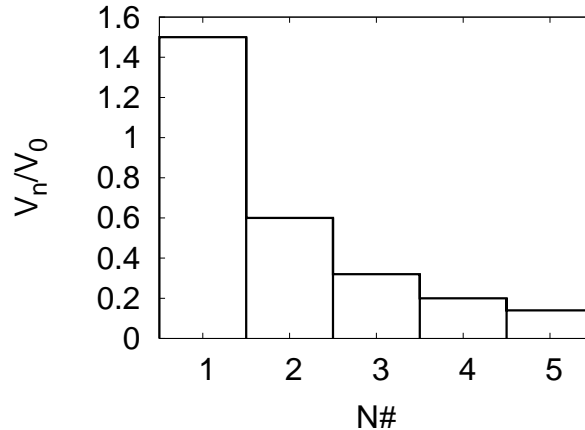


Figure 3.5: Normalized effective volume V_n/V_0 as a function of the mode order.

density could lead to underestimate the Purcell factor near plasmonic nanostructures [Koenderink 2010] (however, he defined the coupling rate to the whole system rather than considering the coupling into a single mode). Oppositely, we adopt here a phenomenological approach where the mode volume is defined so that Purcell factor remains valid. Nevertheless, both methods lead to very similar results for the effective volumes of localized SPPs supported by a nanosphere. Since mode volume is generally a simple way to qualitatively characterize the mode extension, expressions derived here or by Sun *et al* could be used. We discuss in more details the energetic definition of the mode volume in section 3.2.

3.1.3 β –factor

Purcell factor quantifies the coupling strength between a quantum emitter and a (plasmon) mode but lacks information on the coupling efficiency as compared to all the others emitter relaxation channels. However, one can determine the coupling efficiency into a single mode as compared to all others modes. This coupling efficiency, or the so-called β –factor, is easily estimated in case of a spherical metallic particle since all the available channels are taken into account in the Mie expansion. Coupling efficiency into n^{th} mode writes

$$\beta_n = \frac{\langle \gamma_n \rangle}{\langle \gamma_{tot} \rangle}, \quad (3.30)$$

where $\langle \gamma \rangle = (\gamma^\perp + 2\gamma^\parallel)/3$ is the decay rate of a randomly oriented molecule. β –factor is represented on Fig. 3.6 for the first three modes. A maximum efficiency of 90% can be achieved in the dipolar mode ($d \sim 10$ nm) and 87% into quadrupolar mode ($d \sim 15$ nm). The coupling efficiency into the hexapolar mode is lower ($\sim 60\%$ around $d \sim 15$ nm) since it has a very low extension, as indicated in Fig. 3.5. For very short distances, all the coupling efficiencies drop down to zero since all the higher order modes accumulate in this region, opening numerous alternative decay

channels. Moreover, it is possible to efficiently couple the emitter to either the dipolar or quadrupolar mode, by matching the emitter and mode wavelengths. This is of strong importance when designing a SPASER (or plasmon laser) [Bergman 2003] so that the active mode can be tuned on the dipolar or quadrupolar mode. This last *spasing* mode would consist of an extremely localized and ultrafast nanosource [Stockman 2010].

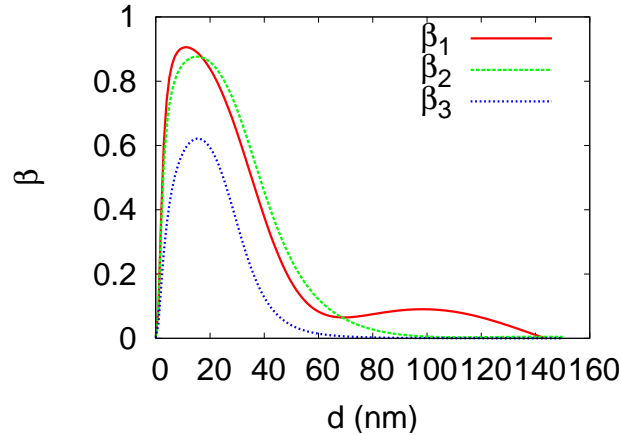


Figure 3.6: Coupling efficiency into the dipolar (β_1), quadrupolar (β_2) and hexapolar (β_3) mode of a 50 nm silver sphere in PMMA, calculated using exact Mie expansion. The emitter wavelength is assumed to match the considered mode. Therefore β_1 , β_2 and β_3 are calculated at $\lambda_1 = 435$ nm (dipolar resonance), $\lambda_2 = 387$ nm (quadrupolar resonance), and $\lambda_3 = 375$ nm (hexapolar resonance), respectively.

3.2 Mie plasmon

In this section, we extend the previous method to the study of the size dependence of LSP mode characteristics. We focus on Mie plasmons supported by a metallic nanosphere (see e.g. Fig. 3.3 showing the two first modes of a silver particle) by applying exact calculations.

The coupling between a dipolar emitter and a metallic sphere is exactly described thanks to Mie expansion on the particle localized modes. It is therefore possible to investigate the role of each mode on the coupling process. We first determine their quality factor and evaluate the contribution of radiative and absorption rates. Secondly, we define their mode volume. To this aim, we propose two definitions. The first one describes spatial extension on which the coupling to an emitter remains efficient. The second one, directly adapted from cQED considerations, is related to the energy confinement.

3.2.1 Resonance quality

Let us consider a silver nanosphere of radius R . In the following, we use either tabulated data for the metal permittivity ε_{Ag} [Johnson 1972] for quantitative investigation or a Drude model $\varepsilon_{Ag}(\omega) = 1 - \omega_p^2/(\omega^2 + i\omega\Gamma_D)$ ($\hbar\omega_p = 9.1$ eV, $\hbar\Gamma_D = 18$ meV) for comparison with the previous section.

3.2.1.1 Quality factor

The quality factor associated to the n^{th} mode of the particle writes $Q_n = \omega_n \tau_n$ where ω_n and $\tau_n = 1/\Gamma_n$ are resonance angular pulsation and lifetime of the n^{th} localized SPP, respectively. In the case of Drude metal, these two parameters are directly obtained as the complex root $\tilde{\omega}_n = \omega_n - i\Gamma_n/2$ of the n^{th} SPP dispersion relation [Kolwas 2009]:

$$n_{Ag}\psi_n(k_{Ag}R)\xi'_n(k_B R) - n_B\xi_n(k_B R)\psi'_n(k_{Ag}R) = 0, \quad (3.31)$$

with $k_{Ag} = \varepsilon_{Ag}^{1/2}\omega/c$, $k_B = \varepsilon_B^{1/2}\omega/c$ the wavenumber in the particle and homogeneous background (permittivity ε_B), respectively. j_n , $h_n^{(1)}$, $\psi_n(z) = zj_n(z)$, and $\xi_n(z) = zh_n^{(1)}(z)$ refer to spherical Bessel, Hankel and Ricatti-Bessel functions. Prime stands for derivative.

We also consider tabulated data for the silver permittivity, we calculate the extinction cross section of the particle, keeping only the n^{th} mode contribution in the Mie expansion. As proceed on the previous section, a fit with a Lorentzian profile gives the resonance peak and full-width at half-maximum from which we deduce the mode quality factor.

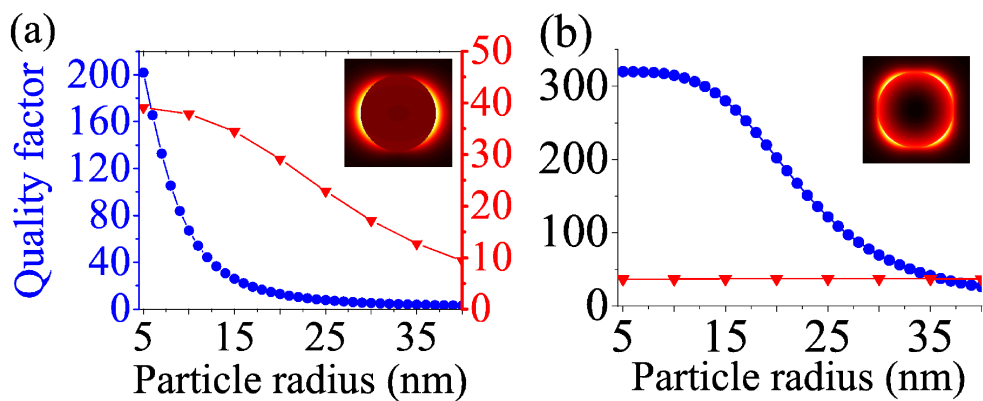


Figure 3.7: Dipolar (a) and quadrupolar (b) SPP quality factor as a function of particle radius. The metal dielectric constant follows Drude model (blue curves, dots) or is taken from Johnson & Christy tabulated data (red curves, triangles).

Figure 3.7 represents the Q factor for the dipolar and quadrupolar modes of a silver sphere in air as a function of its radius. We observe a strong dependency on the

particle size when considering the Drude permittivity. Indeed, the radiative losses increase with the particle size leading to low Q factors. This effect is stronger for the dipolar mode that efficiently radiates in the far-field. Q factor obtained considering tabulated silver permittivity are lower than for Drude model, due to higher absorption. Although less pronounced, we also observe that dipolar Q factor decreases with the particle size (Fig. 3.7a). The quality factor of the quadrupolar mode (Fig. 3.7b), calculated with the tabulated permittivity ($Q_2 \approx 37$), does not depend on the particle size since it is limited by Joule losses as discussed in the next paragraph.

3.2.1.2 Losses channels

We now quantify the radiative and non radiative contributions to the mode losses. In the quasi-static approximation, and for Drude metal, the total losses rate of the n^{th} SPP mode is given by $\Gamma_n = \Gamma_D + \Gamma_n^{rad}$ as seen in the previous section 3.1. Joule losses are the same for all the LSP modes and given by the Drude decay rate Γ_D . The radiative rate $\Gamma_n^{rad} \propto (k_n R)^{2n+1}$ increases with the particle radius and is higher for the first particle modes (dipolar mainly). In Fig. 3.8 we compare this quasi-static approximation to exact calculations. The radiative losses (Fig. 3.8a-b) follows the quasi-static approximation for particle radius below 15 nm. It is about 50 times higher for the dipolar than for the quadrupolar mode.

Figure 3.8(c-d) clearly shows strong deviations of the exact Joule rate compared to the quasi-static approximation. For very small particles, the absorption rate is equal to the Drude decay rate for both dipolar and quadrupolar modes (horizontal black curve). However, it decreases with the particle size. Indeed, for large metallic particles the mode radiatively leaks into the far-field so that only a small portion of its field is confined into the absorbing nanostructure. Similar behaviours occur considering tabulated silver dielectric constant.

At this point, we would like to emphasize that the LSP Q factor defines a high bandwidth due to strong losses. Therefore, we expect efficient molecular coupling to a LSP mode on a large spectral domain. The large resonance breadth is however mainly due to strong absorption into the metal. Indeed, realistic data (red curves) exhibits absorption rates (Γ_{nrad}) that are 10 times higher than the radiative rate (Γ_{rad}) for the quadrupolar mode. The dipolar mode couples to far-field with a ratio $\Gamma_{rad}/\Gamma_{nrad}$ which does not exceed 4.

As far as nanoantennas applications are concerned, it is better to work on the radiative quality factor $Q_n^{rad} = \omega_n/\Gamma_n^{rad}$ that includes radiative losses only. Then the coupling bandwidth corresponds to radiative losses so that low Q^{rad} factors would indicate coupling on a large bandwidth that is associated to available signal in the far-field. The Q^{rad} bandwidth is however strongly limited for small particles

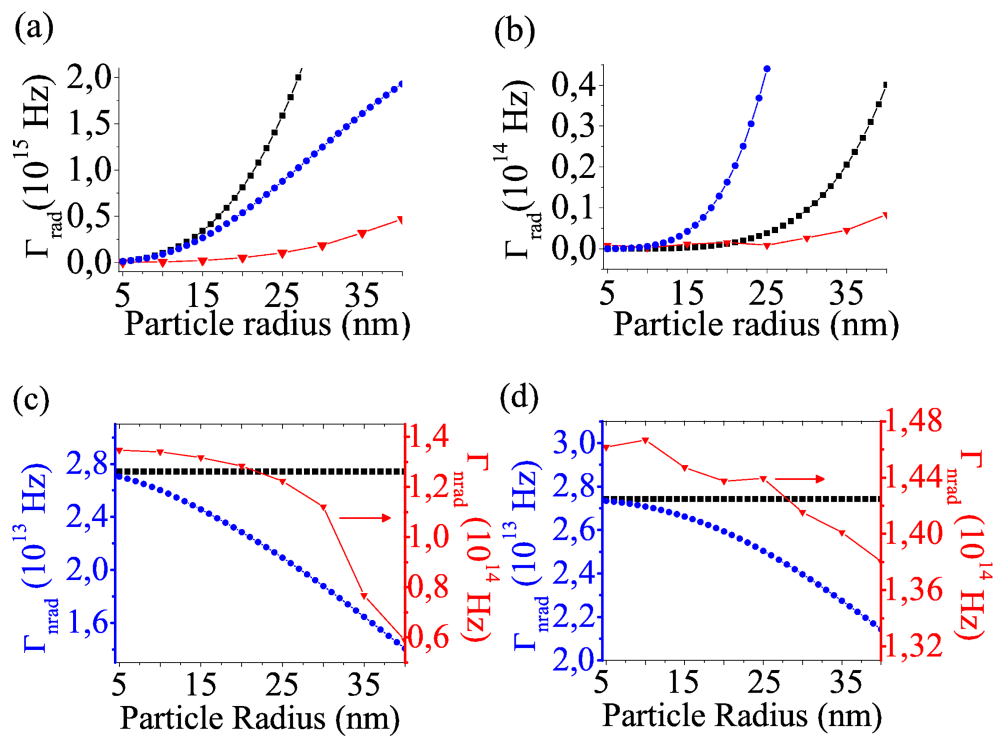


Figure 3.8: Radiative and absorption rates for dipolar and quadrupolar mode. The metal dielectric constant follows Drude model (blue curves) or is taken from Johnson & Christy tabulated data (red curves). The black curves consider Drude metal and quasi-static approximation. Left column (a,c): dipolar mode, right column (b,d): quadrupolar mode. Top graphs (a,b): radiatives rates. Bottom graphs (c,d): non radiatives rates.

(see Fig. 3.8a,b) so that nanoantennas present a minimal size, known as Chu limit [Chu 1948, Agio 2012]. As far as near-field behaviour is concerned (e.g. SPASER), we do not expect theoretical lower limit for the system size.

3.2.2 Effective volume

The modal volume of localized SPPs quantifies their confinement. It is however difficult to evaluate since LSPs can radiatively leak in the far-field as discussed previously. We analyse here two different definitions. First, the mode volume is defined so that the Purcell factor remains valid for a dipolar emitter coupled to a plasmonic nanostructures. Secondly, we consider the usual definition based on mode energy confinement and follow the work of Koenderink to avoid the difficulties due to leakages [Koenderink 2010].

3.2.2.1 Coupling range to a quantum emitter

Let us first consider a dipolar emitter of emission wavelength λ located at distance $d = z - R$ of a spherical metallic nanoparticle. For a randomly oriented emitter, its coupling to the plasmonic particle opens new radiative and non radiative decay channels so that its total decay rate is modified according to [Kim 1988, Colas des Francs 2008]:

$$\begin{aligned} \frac{\gamma}{\gamma_0} &= \frac{1}{3} \frac{\gamma_{\perp}}{\gamma_0} + \frac{2}{3} \frac{\gamma_{\parallel}}{\gamma_0}, \\ \frac{\gamma_{\perp}}{\gamma_0} &= 1 - \frac{3}{2} Re \sum_{n=1}^{\infty} n(n+1)(2n+1) a_n \left[\frac{h_n^{(1)}(u)}{u} \right]^2, \\ \frac{\gamma_{\parallel}}{\gamma_0} &= 1 - \frac{3}{2} Re \sum_{n=1}^{\infty} \left(n + \frac{1}{2} \right) \left[a_n \left[\frac{\zeta_n'(u)}{u} \right]^2 + b_n [h_n^{(1)}(u)]^2 \right], \end{aligned} \quad (3.32)$$

where the subscript \perp (\parallel) indicates a dipole perpendicular (parallel) to the particle surface and $u = k_B z$. The Mie's scattering coefficients a_n and b_n write:

$$\begin{aligned} a_n &= \frac{n_{Ag} \psi_n(k_{Ag} R) \psi_n'(k_B R) - n_B \psi_n(k_B R) \psi_n'(k_{Ag} R)}{n_{Ag} \psi_n(k_{Ag} R) \xi_n'(k_B R) - n_B \xi_n(k_B R) \psi_n'(k_{Ag} R)}, \\ b_n &= \frac{n_B \psi_n(k_{Ag} R) \psi_n'(k_B R) - n_{Ag} \psi_n(k_B R) \psi_n'(k_{Ag} R)}{n_B \psi_n(k_{Ag} R) \xi_n'(k_B R) - n_{Ag} \xi_n(k_B R) \psi_n'(k_{Ag} R)}. \end{aligned} \quad (3.33)$$

Expression (3.32) originates from the Fermi's golden rule and quantifies the modification of the decay rate of an emitter by coupling to all the electromagnetic modes sustained by the surroundings. Differently, Purcell factor expresses the effect of one mode (of e.g. a micro-optical cavity or, as here, a metallic nanoparticle). Since a_n refers to the TM polarized LSP mode (dispersion relation (3.31) corresponds to the

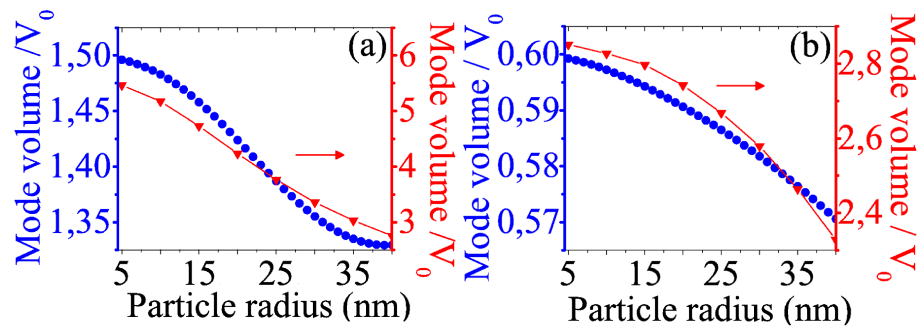


Figure 3.9: Dipolar (a) and quadrupolar (b) SPP volume as a function of particle radius. The metal dielectric constant follows Drude model (blue curves) or is taken from Johnson & Christy tabulated data (red curves) [Johnson 1972]. Mode volume is normalized with respect to the particle volume V_0 .

pole of a_n), we determine the contribution of the n^{th} localized SPP to the decay rate

$$\frac{\gamma^n}{\gamma_0} = \frac{1}{3} \frac{\gamma_{\perp}^n}{\gamma_0} + \frac{2}{3} \frac{\gamma_{\parallel}^n}{\gamma_0}, \quad (3.34)$$

$$\frac{\gamma_{\perp}^n}{\gamma_0} = -\frac{3}{2} \text{Re} \left[n(n+1)(2n+1)a_n \left[\frac{h_n^{(1)}(u)}{u} \right]^2 \right],$$

$$\frac{\gamma_{\parallel}^n}{\gamma_0} = -\frac{3}{2} \text{Re} \left[\left(n + \frac{1}{2} \right) a_n \left[\frac{\zeta_n'(u)}{u} \right]^2 \right].$$

Having extracted the contribution of one mode of the metallic particle, we can identify it to the Purcell factor that expresses the coupling rate to a given mode:

$$\frac{\gamma^n}{\gamma_0} = \frac{3}{4\pi^2} \left(\frac{\lambda}{n_B} \right)^3 \frac{Q_n}{V_n}. \quad (3.35)$$

Note that Purcell factor expresses the maximum decay rate achievable by coupling to a mode, that is for an emitter located at the particle surface in the case considered here ($z = R$). Identifying expressions (3.34) and (3.35), and using the quality factor calculated previously, we compute in Fig. 3.9 the effective volumes of the dipolar and quadrupolar modes. This effective volume quantifies the region on which dipolar emitters efficiently couple to the particle mode. Effectives volumes are normalized with respect to the particle volume $V_0 = 4\pi R^3/3$. In case of Drude metal, we obtain $V_1 = 1.5V_0$ and $V_2 = 0.6V_0$ for the dipolar and quadrupolar mode respectively for very small particles as demonstrated in section 3.1. The normalized mode volume slightly decreases with the particle size. However it corresponds to an increase of the absolute mode volume (see Fig. 3.10). Considering experimental metal permittivity, we compute larger mode volumes but still strongly below the diffraction limit. For both Drude and tabulated permittivities, we check that the quadrupolar mode is roughly two times more confined than the dipolar mode.

3.2.2.2 Mode energy confinement

In cQED, mode volume is defined as the energy confinement. For dispersive materials, this leads to (see also Ref. [Lecamp 2007] for a classical derivation)

$$\begin{aligned}
 V_n^{nrj} &= \frac{\int U_n(\mathbf{r}) d\mathbf{r}}{\max[\varepsilon_0 \varepsilon_B |\mathbf{E}_n(\mathbf{r})|^2]}; \\
 U_n(\mathbf{r}) &= \frac{\partial[\omega \varepsilon_0 \varepsilon(\mathbf{r}, \omega)]}{\partial \omega} |\mathbf{E}_n(\mathbf{r})|^2 + \mu_0 |\mathbf{H}_n(\mathbf{r})|^2
 \end{aligned} \tag{3.36}$$

where $(\mathbf{E}_n, \mathbf{H}_n)$ is the electromagnetic field of the n^{th} mode. Recently, Sun and coworkers used this definition and obtained $V_1^{nrj} = 1.5V_0$ and $V_2^{nrj} \approx 0.67V_0$ for the dipolar and quadrupolar mode respectively in the quasi-static approximation and for Drude metal [Khurgin 2009]. This is in good agreement with the mode volumes deduced from the Purcell factor. However, quasi-static approximation is no longer valid for large particles and the exact expressions of $(\mathbf{E}_n, \mathbf{H}_n)$ has to be used. It expresses

$$\begin{aligned}
 \mathbf{E}_n(\mathbf{r}) &= i^{n-1} \frac{2n+1}{n(n+1)} \begin{cases} n_{Ag} \mathbf{N}_{e1n}^{(1)}(\mathbf{r}) & (r < a) \\ n_B \frac{\psi'_n(k_{Ag}a)}{\zeta'_n(k_Ba)} \mathbf{N}_{e1n}^{(3)}(\mathbf{r}) & (r \geq a) \end{cases} \\
 \mathbf{H}_n(\mathbf{r}) &= i^{n-1} \frac{2n+1}{n(n+1)} \sqrt{\frac{\varepsilon_0}{\mu_0}} \begin{cases} \varepsilon_{Ag} \mathbf{M}_{e1n}^{(1)}(\mathbf{r}) & (r < a) \\ \varepsilon_B \frac{\psi'_n(k_{Ag}a)}{\zeta'_n(k_Ba)} \mathbf{M}_{e1n}^{(3)}(\mathbf{r}) & (r \geq a) \end{cases}
 \end{aligned} \tag{3.37}$$

where \mathbf{N}_{e1n} and \mathbf{M}_{e1n} are the vector spherical harmonics, explicitly given in Bohren & Huffman [Bohren 1983].

Moreover, the application of definition (3.36) is difficult for large particles since localized LSPs leak in the far-field so that the energy confinement is not finite. As far as light-matter coupling is concerned, the pertinent parameter is the confinement of the mode energy stored inside the cavity. Following recent work of Koenderink [Koenderink 2010], we calculate on Fig. 3.10(a,b) the mode volume as a function of the integration volume for two particle sizes. Small particle ($R = 5$ nm, Fig. 3.10a) presents low radiative losses and the energy enclosed in the integration sphere only slightly depends on the integration volume. For a particle radius $R = 40$ nm (Fig. 3.10b), we observe a strong linear increase of the mode volume with the integration sphere radius. Indeed, as discussed above (see Fig. 3.8a), large particles support strongly radiative modes. The energy flux through a surface sphere is constant for distances large enough so that the energy enclosed within this sphere linearly increases with its radius. Finally, the intrinsic mode volume is estimated from the energy confinement, excluding radiative leaks [i.e, ordinate at the origin in Fig. 3.10(a,b)].

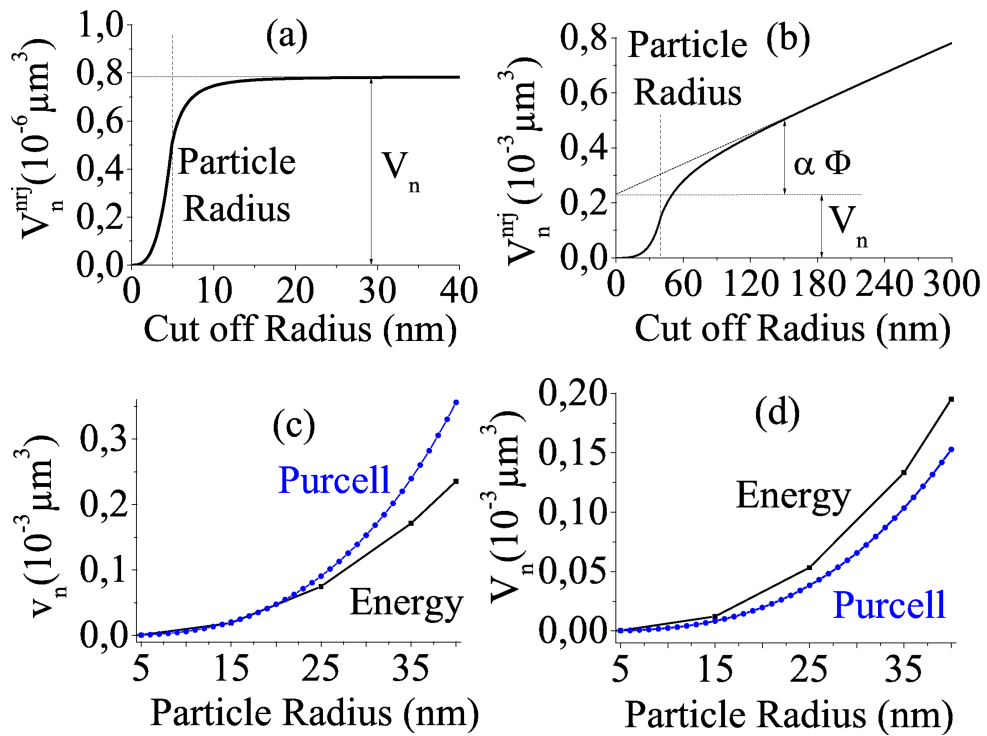


Figure 3.10: Mode energy confinement. (a,b) Mode volume expression (3.36) as a function of the integration sphere cut-off radius. The metallic sphere radius is $R = 5$ nm (a) or $R = 40$ nm (b). The energy enclosed in the integration sphere linearly increases with sphere radius with a slope proportional to the field flux Φ . The mode volume energy is defined as the ordinate at origin. (c,d) Dipolar (a) and quadrupolar (b) LSP volumes. Purcell and energy refer to the mode volume definition. The metal dielectric constant follows Drude model.

Figure 3.10(c,d) represents the effective (energy) volume of the dipolar and quadrupolar SPPs. Modes volumes are strongly subwavelength and similar to the values obtained using Purcell factor definition for small particle sizes. However, significant differences appear for large particles. Particularly, for the dipolar mode, the energy confinement underestimates the volume on which the coupling remains efficient (“Purcell” mode volume) since the radiative leakages are removed. Moreover, the calculated modes energy confinement are similar for dipolar and quadrupolar modes since they do not take into account the radiative losses. In conclusion, applying the Purcell factor expression with the mode energy confinement volume could lead to inaccuracies. Nevertheless, the concept of particle modes becomes flawed for large particles since they are characterized by an extremely short lifetime (below their oscillation period). Insofar as mode volume represents the mode extension both expressions lead to similar order of magnitude and can be used. Finally, localized SPP effective volume is of the order of the particle physical volume that is, of *nanometric dimensions*.

3.3 Conclusion

In this chapter, we have proposed a quasi-static approximation based description of the resonance quality and mode confinement of the localized SPPs supported by a metallic nanosphere. We retrieved fully analytical and simple expressions with a clear physical meaning.

Quantitatively, the role of radiative and absorption losses have been clearly identified. We also discuss the definition and the behaviour of the modes effective volumes. In particular, we have found that discrepancies occur by using the definition based on either energy mode confinement or Purcell factor. However, very recently, Sauvan and co-workers propose to define a complex energetic mode volume that allows to extend the Purcell factor definition to open cavities [Sauvan 2013].

Anyway, we retrieve strongly subwavelength confinement, that is of great interest for applications involving light-matter interaction at the nanoscale. In the next chapter, we describe optical nanosources based on plasmonic core-shell nanoparticles doped with luminescent material (dye molecule or rare-earth ions). In a more prospective way, it is interesting to note that Stockman recently estimated the SPASER threshold as $d_{12}^2 N Q_n / \hbar \gamma V_n > 1$ where d_{12} is the dipolar moment of the emitters constituting the gain medium, γ their decay rate, N the number of emitters within the mode effective volume V_n and Q_n the mode quality factor [Stockman 2010]. Therefore, we expect the possibility to tune the SPASER emission on either dipolar or quadrupolar localized SPP by a proper choice of the gain medium emission wavelength, by profiting on the strong mode confinement, despite a rather low quality factor.

Luminescent doped plasmonic nanoparticles

Contents

4.1	Mie description of metal enhanced fluorescence	58
4.1.1	Excitation field and pumping rate	58
4.1.2	Emission rate	61
4.1.3	Fluorescence enhancement in the continuous regime	62
4.2	Effect of the particle size	64
4.2.1	Excitation and emission rate	64
4.2.2	Single molecule metal enhanced fluorescence	65
4.3	Fluorescence of doped core-shell plasmonic particles	66
4.3.1	Average enhancement factor	67
4.3.2	Rare earth doped plasmonic core shell	69
4.4	Conclusion	74

In this chapter, we investigate fluorescence modification of Rhodamine 6G (Rh6G) and Rare earth ions near a metal nanoparticle (MNP). Rh6G molecule is typically used for dye lasers because of its photostability and its high quantum yield. Therefore Rh6G-MNP coupled systems have been widely studied to understand metal enhanced fluorescence and will serve as a reference system [Shalaev 2007, Reineck 2013]. Rare earth (RE) ions are widely studied for solar cells, optical amplification or biological fluorescence imaging. Although they present high quantum efficiencies, they could suffer from low absorption cross-section [Bünzli 2007] so that metal enhanced fluorescence has been proposed to improve their emission properties.

We are interested in core-shell particles, where the metallic core enhances the emission of emitters doping the shell. To this aim, we first present Mie theory that exactly describes metal enhanced fluorescence near a spherical particle. Then, we focus on doped core-shell particles. We notably define an average fluorescence factor that characterizes the efficiency of the whole hybrid nanosource.

4.1 Mie description of metal enhanced fluorescence

Figure 4.1 is a schematic view of the coupling between a metallic nanoparticle and a dipole. The whole system is excited by a plane wave:

$$\mathbf{E}_i = E_0 \exp i(\mathbf{kz} - \omega t) \mathbf{e}_x, \quad (4.1)$$

with a wave-number $k = 2\pi n_B/\lambda$.

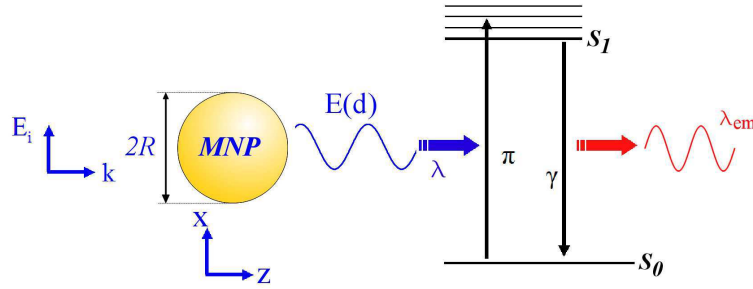


Figure 4.1: Schematic view of the coupling between a metallic nanoparticle and quantum emitter separated by a distance d . The Jablonski diagram illustrates the energy levels of the emitter. The coupled system is excited by the incident electric field \mathbf{E}_i . The MNP and background dielectric constant are ε_m and ε_B , respectively.

The emitter is modeled as a two level system (TLS) on the Jablonski diagram depicted on Fig. 4.1: the ground singlet state \mathbf{S}_0 and the excited state \mathbf{S}_1 . In order to describe the Stokes shift between absorption and emission wavelengths, we also consider a vibrational state ν in the excited level \mathbf{S}_1 . The system is excited from \mathbf{S}_0 to (\mathbf{S}_1, ν) at wavelength λ_{exc} . The vibrational relaxation to the lowest vibrational state of \mathbf{S}_1 is much faster than other process so that its duration is neglected. Then emission occurs at $\lambda_{em} > \lambda_{exc}$. The TLS is modeled with a transition dipolar moment of arbitrary orientation $\mathbf{u} = \mathbf{u}_0(\sin \alpha \cos \beta, \sin \alpha \sin \beta, \cos \alpha)$.

The enhancement factor of the fluorescence signal is proportional to

- the excitation rate $|\mathbf{u} \cdot \mathbf{E}(\mathbf{r}, \omega_{exc})|^2 / |\mathbf{E}_0|^2$ where $\mathbf{E}(\mathbf{r}, \omega_{exc}) = \mathbf{E}_i + \mathbf{E}_s$ refers to the excitation field at the emitter location \mathbf{r} and excitation angular frequency $\omega_{exc} = 2\pi c / \lambda_{exc}$,
- the emitter quantum yield $\eta(\mathbf{r}, \omega_{em}) = \gamma^R / (\gamma^R + \gamma^{NR})$ at the emission angular frequency ω_{em} .

4.1.1 Excitation field and pumping rate

We assume a spherical particle of optical index $n_m = \sqrt{\varepsilon_m}$ embedded in a dielectric background of optical index $n_B = \sqrt{\varepsilon_B}$. The scattered electric field \mathbf{E}_s is expressed

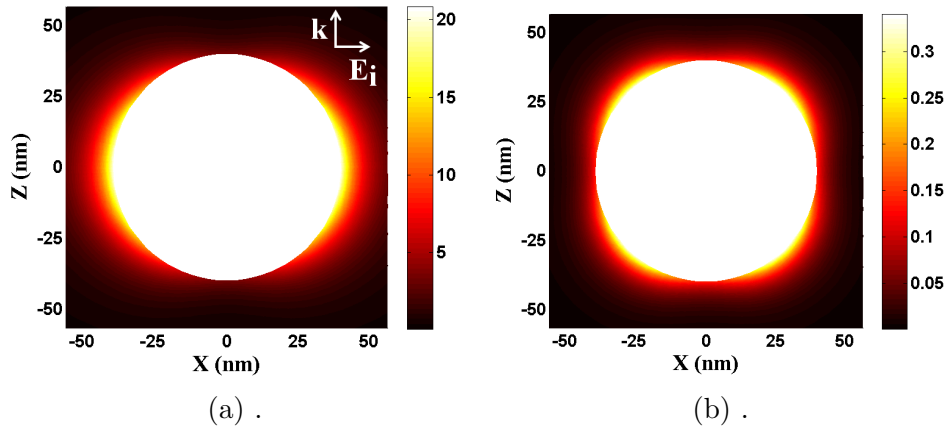


Figure 4.2: Near field electrical intensity maps near a 80 nm gold particle in air. Contribution of the dipolar (a) and the quadrupolar (b) mode. The particle is illuminated at the wavelength $\lambda = 532$ nm. The bulk gold dielectric function $\varepsilon_{Au}(\lambda)$ is extracted from Johnson & Christy's tabulated data [Johnson 1972].

according to Mie expansion on the particle modes[Bohren 1983]:

$$\mathbf{E}_s(r, \theta, \phi) = E_0 \sum_{n=1}^{\infty} i^n \frac{2n+1}{n(n+1)} (ia_n \mathbf{N}_n(r, \theta, \phi) - b_n \mathbf{M}_n(r, \theta, \phi)). \quad (4.2)$$

\mathbf{M}_n and \mathbf{N}_n are vector spherical harmonics and are fully detailed on page 89 of Ref. [Bohren 1983]. a_n and b_n are the Mie coefficients (Eq. 3.33).

Figure 4.2 depicts the dipolar and quadrupolar contribution to the scattered field near a 80nm gold particle. The dipolar mode is sufficient to describe the particle optical response in the near-field since the other modes contribution are negligible (see the color scale bar). We also represent on Fig. 4.3 the spectral response of the excited modes. The dipolar and quadrupolar resonance appear at $\lambda = 532$ nm and $\lambda = 524$ nm, respectively. We observe strong field enhancement near the dipolar resonance that could lead to molecule excitation enhancement.

The pumping rate Π is proportional to the absorption power P_{abs} [Novotny 2006]:

$$\Pi(d) = \frac{P_{abs}}{\hbar\omega_0} = \frac{Im\{\alpha\}}{2\hbar} |\mathbf{u} \cdot \mathbf{E}(\mathbf{d})|^2, \quad (4.3)$$

where α is the molecular polarizability. In order to characterize the plasmonic effect independently on the molecule, it is convenient to normalize the pumping rate $\Pi(d)$ with respect to its free-space value Π_0 :

$$\Pi_0 = \frac{Im\{\alpha\}}{2\hbar} |\mathbf{u} \cdot \mathbf{E}_i|^2, \quad (4.4)$$

so that

$$\Pi(d) = \Pi_0 \frac{|\mathbf{u} \cdot \mathbf{E}(\mathbf{d})|^2}{|\mathbf{u} \cdot \mathbf{E}_i|^2}. \quad (4.5)$$

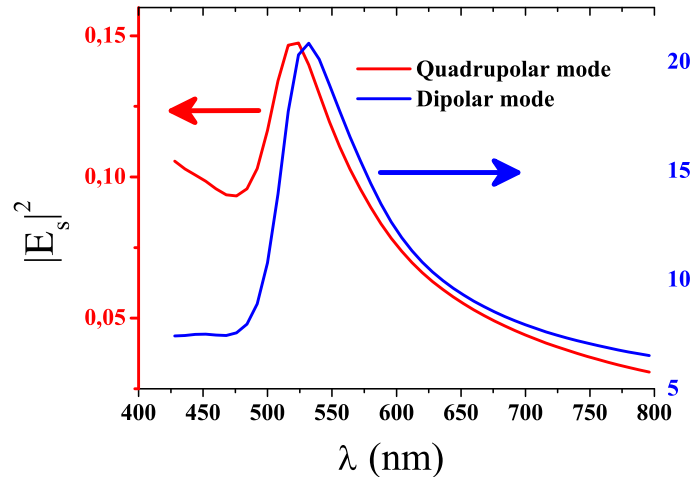


Figure 4.3: Near field scattering spectra of dipolar and quadrupolar modes shown on Fig. 4.2, calculated at the particle surface.

Figure 4.4 depicts the enhancement of the pumping rate $\Pi(d)/\Pi_0$. It decreases when the coupling distance d increases as expected for the strongly confined dipolar LSP.

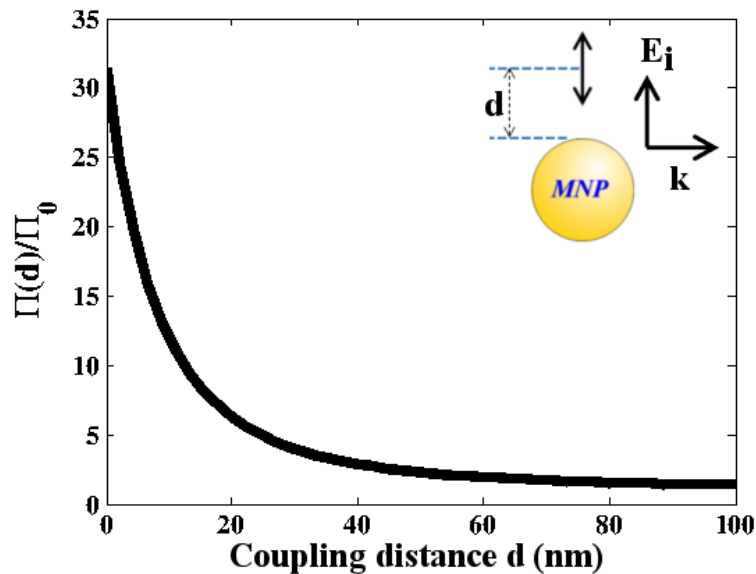


Figure 4.4: Normalized excitation rate of a molecule at a distance d from gold particle surface. Parameters are the same as used in Figure 4.2.

4.1.2 Emission rate

We discuss the modification of the emission decay rate near a spherical MNP. This topic has been studied intensively in the 80's [Ruppin 1982, Chew 1987, Kim 1988]. For an emitter perpendicular to the particle surface, the total and the radiative decay rates are expressed as:

$$\frac{\gamma_{\perp}}{\gamma_0} = 1 + \eta_0 \frac{3}{2} \Re \left\{ \sum_{n=1}^{\infty} (2n+1)n(n+1)(-a_n) \left(\frac{h_n^{(1)}(\rho)}{\rho} \right)^2 \right\}, \quad (4.6)$$

$$\frac{\gamma_{\perp}^R}{\gamma_0} = \eta_0 \frac{3}{2} \sum_{n=1}^{\infty} n(n+1)(2n+1) \left| \frac{j_n(\rho) - a_n h_n^{(1)}(\rho)}{\rho} \right|^2, \quad (4.7)$$

where η_0 is the intrinsic quantum yield of the molecule and $\rho = 2\pi n_B z / \lambda_{em}$. For dipole parallel to the surface:

$$\frac{\gamma_{\parallel}}{\gamma_0} = 1 + \eta_0 \frac{3}{2} \Re \left\{ \sum_{n=1}^{\infty} \left(n + \frac{1}{2} \right) \left[-a_n \left[\frac{\zeta'_n(\rho)}{y_1} \right]^2 - b_n (h_n^{(1)}(\rho))^2 \right] \right\}, \quad (4.8)$$

$$\frac{\gamma_{\parallel}^R}{\gamma_0} = \eta_0 \frac{3}{4} \sum_{n=1}^{\infty} (2n+1) \left[|j_n(\rho) - b_n h_n^{(1)}(\rho)|^2 + \left| \frac{\psi'_n(\rho) - a_n \zeta'_n(\rho)}{\rho} \right|^2 \right]. \quad (4.9)$$

Note that the Mie coefficients (see Eq. 3.33) have to be calculated at the emission wavelength. Finally, the non-radiative decay rate is

$$\frac{\gamma^{NR}}{\gamma_0} = \frac{\gamma}{\gamma_0} - \frac{\gamma^R}{\gamma_0}. \quad (4.10)$$

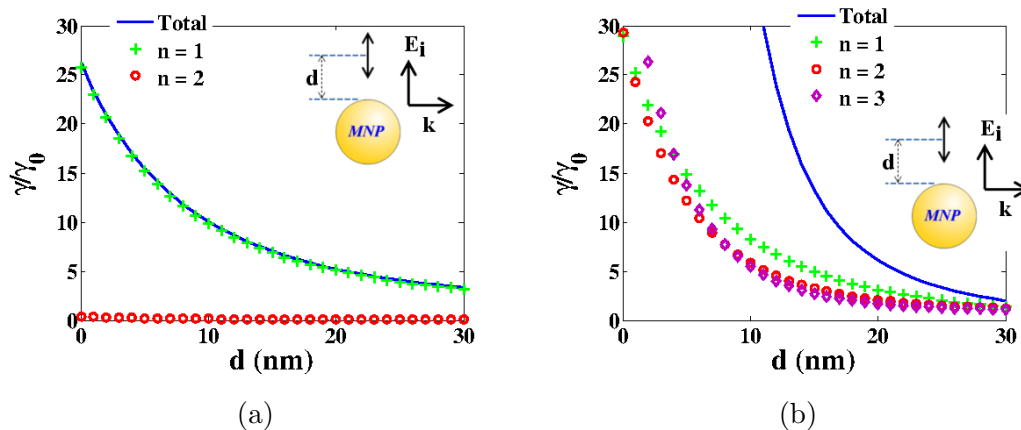


Figure 4.5: Mode contribution to radiative (a) and non-radiative (b) decay rates as a function of the distance coupling d for a perpendicularly oriented dipole. The dipole emits light at the wavelength $\lambda_{em} = 560$ nm. The sphere is a 80 nm sized gold particle in air.

Figure 4.5 a) and b) shows the decay rates as a function of the coupling distance d . We observe that γ^{NR} diverges near the surface due to strong non-radiative transfer to the metal (note that the model fails for $d \lesssim 1$ nm where non local description of $\varepsilon_m(\omega)$ has to be used [Vielma 2007, Castanié 2010]). Contrary to the pumping (Fig. 4.3) and radiative (Fig. 4.5a) rate that are governed by the dipolar mode ($n = 1$), we observe in Fig. 4.5b) that non-radiative decay rate is governed by the high order modes at short distances [Mertens 2009].

4.1.3 Fluorescence enhancement in the continuous regime

Finally, the fluorescence signal expresses in the stationary regime

$$I_{fluo}(d) = \Pi(d) \frac{\gamma^R(d)}{\gamma(d)} = \Pi(d) \eta(d) \quad (4.11)$$

where we assume a linear regime ($\Pi \ll \gamma$) that is a good approximation near plasmonic structures. Hence, the fluorescence enhancement is

$$\frac{I_{fluo}(d)}{I_{fluo}(\infty)} = \frac{\Pi(d)}{\Pi_0} \frac{\eta(d)}{\eta_0} = \frac{|\mathbf{u} \cdot \mathbf{E}(d)|^2 \eta(d)}{|\mathbf{u} \cdot \mathbf{E}_i|^2 \eta_0}. \quad (4.12)$$

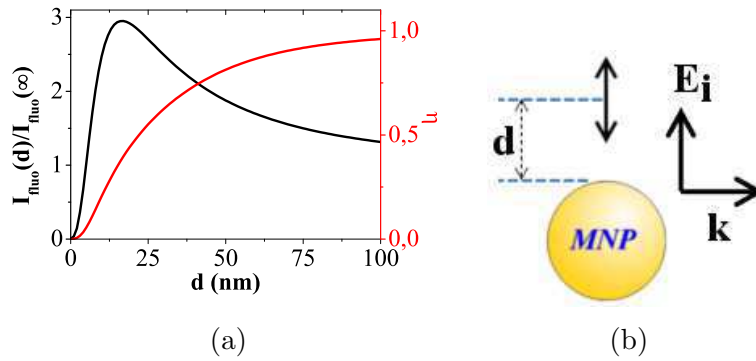


Figure 4.6: a) Computation of the fluorescence signal enhancement (black curve) and the quantum yield (red curve) as a function of the coupling distance d . The intrinsic quantum yield is $\eta_0 = 1$. Other parameters are identical to figures 4.5 and 4.4.

Figure 4.6 shows the emission intensity enhancement as a function of the coupling distance d . This curve is deduced from the previously calculated pumping rate at $\lambda = 532$ nm (Fig. 4.2) and the decay rates at $\lambda_{em} = 560$ nm (Fig. 4.5). The maximum enhancement factor ($\simeq 3$) is obtained for a distance $d = 17$ nm. On the other hand, the quantum yield decreases drastically to zero when decreasing the coupling distance d . This originates from non radiative transfer to the metal and leads to fluorescence quenching.

Coupling distance between Eu^{3+} emitters and silver particles As an illustration of the fluorescence modification close to MNP, we discuss the experimental data obtained by A. Pillonet *et al.* (LPCML, Lyon) in the collaborative project Fenoptics (ANR -09-Nano023). Rare earth ions luminescence applications are *e.g.* colored displays, optical amplifiers or photovoltaic cells so that enhancing their luminescence is important.

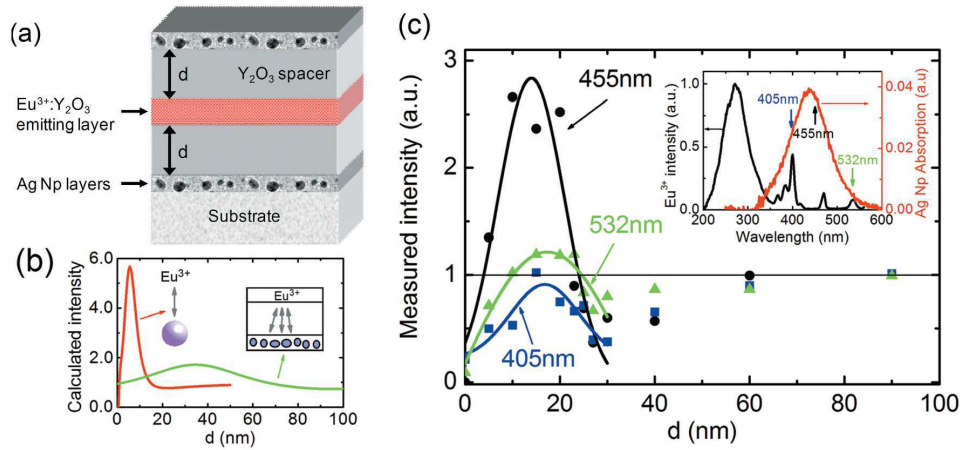


Figure 4.7: a) Scheme of the multilayer consisting of an emitting $Eu : Y_2O_3$ layer separated by a distance d from two silver nanoparticles layers into a passive Y_2O_3 spacer layer. b) Calculated evolution of Eu^{3+} emission versus d by supposing the coupling of an Eu^{3+} emitter with one silver nanoparticle (red curve) or with a silver nanoparticles layer (green curve) as shown in the schemes. c) Experimental evolution of Eu^{3+} emission versus d under excitation at 405 (squares), 455 (circles), and 532 nm (triangles). The inset of (c) shows the comparison between the excitation spectrum of Eu^{3+} emission in $Eu : Y_2O_3$ powders and the silver nanoparticle layer absorption.

The system under study is a multilayer where Eu^{3+} emitters are enclosed between two layers of silver nanoparticles of diameter $\simeq 10\text{nm}$ (Fig. 4.7a). The coupling distance d is controlled by using passive Y_2O_3 spacer layer. Fluorescence intensity measurements (Fig. 4.7c) have been measured for 3 excitation wavelengths: $\lambda = 405\text{nm}$, $\lambda = 455\text{nm}$ (near the LSP resonance) and $\lambda = 532\text{nm}$. The maximum enhancement is achieved for excitation wavelength near the LSP resonance and for distance $d \simeq 17\text{nm}$.

In order to discuss these results, we calculated the fluorescence enhancement near a single nanoparticle as presented in this section. We also calculated the fluorescence signal above a metal mirror to describe the interaction of the Eu^{3+} emitters with an assembly of silver nanoparticles (Fig. 4.7b). To this aim, we modelize the Y_2O_3 doped silver layer with an effective medium of dielectric constant ε_{eff} given by the

Maxwell-Garnett model

$$\frac{\varepsilon_{eff} - \varepsilon_{Y_2O_3}}{\varepsilon_{eff} + 2 \varepsilon_{Y_2O_3}} = f \frac{\varepsilon_{Ag} - \varepsilon_{Y_2O_3}}{\varepsilon_{Ag} + 2 \varepsilon_{Y_2O_3}}, \quad (4.13)$$

where the silver nanoparticles volume fraction was fixed to $f = 0.1$. The signal behavior is qualitatively explained by the interaction to the metal mirror at long distance and coupling to a single MNP at short distance. As expected, plasmon mediated fluorescence enhancement is possible for rare-earth ions coupled to a single MNP. We propose to optimize doped MNP core-shell in the next section.

4.2 Effect of the particle size

Since the LSP resonance strongly depends on the particle size, we discuss the size effect on the fluorescence enhancement. We consider Rh6G as a typical benchmark system to which we will compare when considering rare earth ions system in the following section. In particular, we will discuss the optimum particle wavelength compared to excitation and emission wavelength of the luminescent system.

4.2.1 Excitation and emission rate

Figure 4.8 depicts the excitation and decay rates for an emitter closed to a gold or silver bead. All the maps display spectra according to the particle diameter $D = 2R$. The emitter is perpendicular to the particle surface since stronger magnitudes are obtained for this orientation as shown previously.

The excitation and radiative rates follow the dipolar plasmon mode dispersion for small particle diameters. Large particles support a leaky quadrupolar mode so that the radiative rate couples to this mode. Note that the excitation rate weakly follows the quadrupolar mode dispersion since the emitter is not located on a mode lobe. Finally, the non radiative rate originates from coupling to high order modes so that it presents a flat dispersion curve [Colas des Francs 2008]. The low orders modes are well-separated in case of a silver particle due to lower losses (compare the non radiative rate near gold and silver structures). Last, we observe that the dipolar plasmon resonance can be tuned from $\lambda = 525$ nm (well-defined resonance) to $\lambda \approx 900$ nm (large resonance) for gold beads diameter varying from $D = 10$ nm to $D = 200$ nm. For silver nanoparticles between 10 nm and 100 nm, the dipolar resonance wavelength varies from $\lambda = 400$ nm to $\lambda = 530$ nm. We have now all the ingredient to optimize metal enhanced fluorescence of a single molecule.

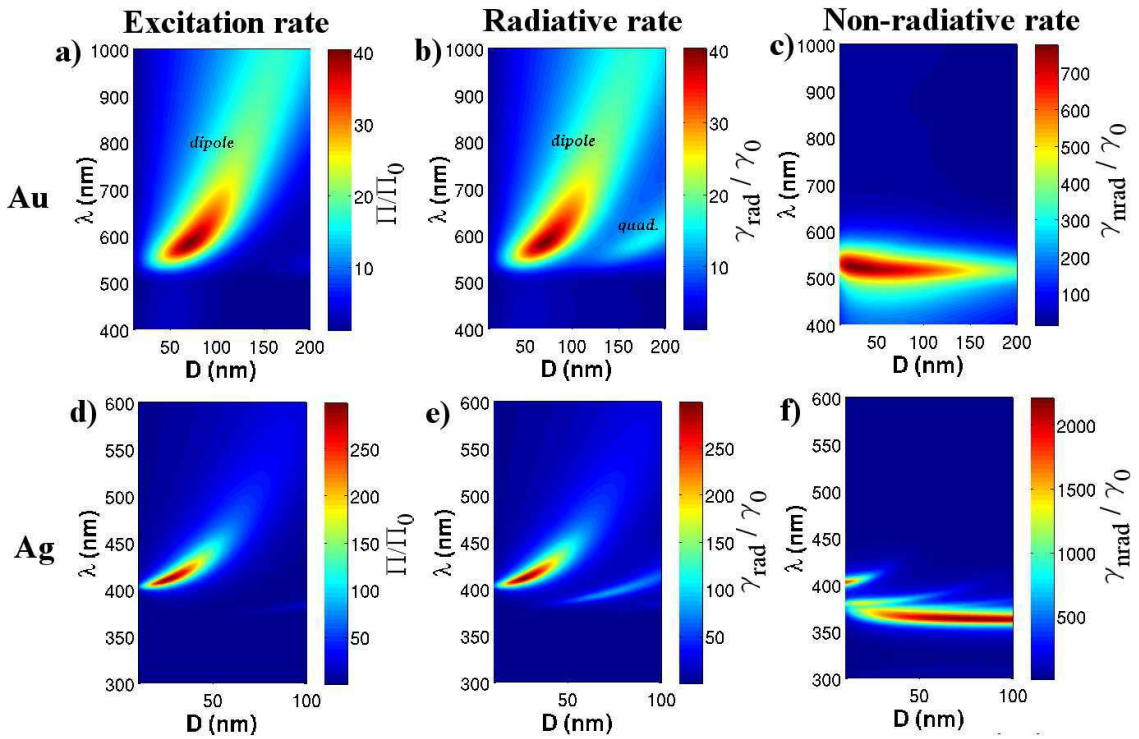


Figure 4.8: Excitation (left), radiative (middle) and non-radiative (right) rates near a metal spherical particle as a function of wavelength and particle diameter. Top (bottom) line refers to gold (silver) particle. The emitter is located 5 nm from the particle surface and perpendicular to it. The optical index of the embedding matrix is $n_B = 1.5$. Metal dielectric constant are taken from Johnson and Christy [Johnson 1972]. *dipole* and *quad.* refer to the dipolar and quadrupolar mode of the particle involved in the coupling mechanism.

4.2.2 Single molecule metal enhanced fluorescence

Since metal enhanced fluorescence depends on both the particle size and molecule position, we first calculate the emission enhancement as a function of the bead diameter and molecule distance to the MNP in Fig. 4.9a).

We observe a maximum enhancement factor of 26 for a particle diameter $D = 80\text{nm}$ and distance $d = 5\text{nm}$. We also plot in Fig. 4.9b) the fluorescence enhancement factor as a function of the distance for the optimum particle size. The optimum particle size is achieved when the dipolar plasmon resonance is near the excitation and emission rate as clearly seen in the extinction efficiency shown in Fig. 4.9c).

We also consider a silver particle in air for comparison (Fig. 4.10). The maximum enhancement is achieved for large particle ($D = 140\text{nm}$) since it is required to red shift the dipolar resonance as close as possible to the emitter excitation and emission wavelengths. The maximum enhancement factor is lower than in PMMA

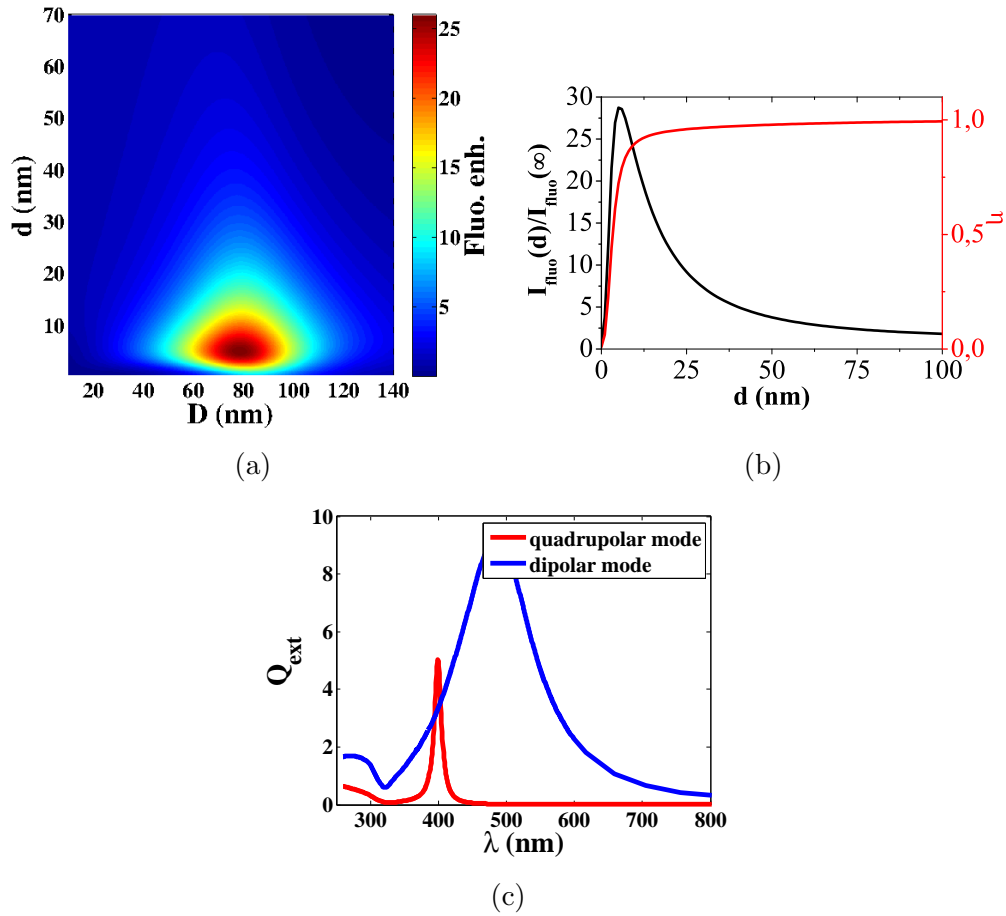


Figure 4.9: a) Fluorescence signal enhancement according to the distance d and the silver particle diameter D . b) Fluorescence signal enhancement (black curve) and quantum yield (red curve) according to the distance d for a particle size of $D = 80$ nm. c) Extinction efficiency spectra of the 80 nm size silver particle. For all those figures, the background medium is PMMA ($n_B = 1.5$) and the emitter is perpendicular to the metal particle surface.

matrix since the particle resonance is still far from the excitation wavelength (see extinction efficiency on Fig. 4.10). Finally, for gold particle in air, the maximum enhancement factor is limited to 6 due to larger losses (see Table 4.1).

4.3 Fluorescence of doped core-shell plasmonic particles

Having determined the metal enhanced fluorescence for a single molecule, we now discuss the average enhancement factor over a doped core-shell particle.

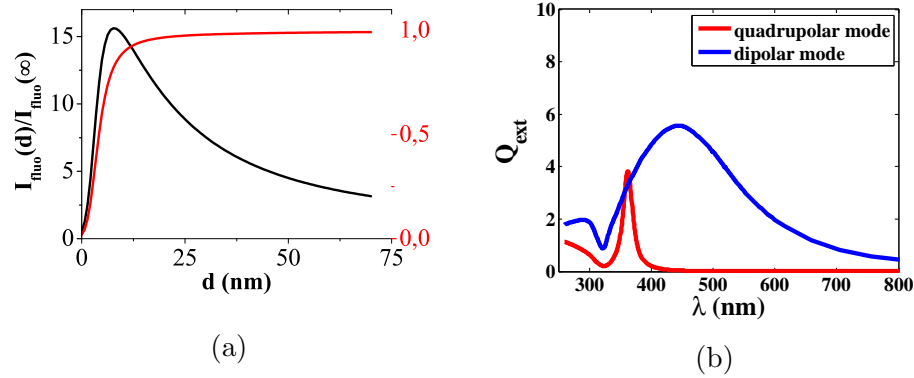


Figure 4.10: a) Fluorescence signal enhancement (black curve) and quantum yield (red curve) of an emitter at a distance d from a 140 nm sized silver particle surface and perpendicular to it. b) Extinction efficiency spectra of the particle. The background medium is air ($n_B = 1$).

Table 4.1: Optimum enhancement factor calculated for 3 different configurations.

Sphere material	Background medium	sphere diameter D	optimum coupling distance d_{max}	$\alpha_{\perp}(d_{max})$
Silver	PMMA	80nm	5nm	29
Silver	Air	140nm	8nm	16
Gold	Air	120nm	16nm	6

4.3.1 Average enhancement factor

The emitter orientation plays a crucial role in metal enhancement fluorescence. Although nice results have been obtained by coupling a single dye molecule with definite orientation with a single MNP or coupled MNPs [Bharadwaj 2007a, Kühn 2006, Anger 2006, Bonod 2010], it is also important to consider a randomly oriented emitter that corresponds to the most common case [Kreiter 2002, Lieb 2004]. In addition, numerous works involve MNP coupling with an ensemble of emitters [Mertens 2006, Marques 2007, Aslan 2007, Kassab 2010, Ma 2009, Som 2011, van Wijngaarden 2011, Deng 2011, Rivera 2012] in a core-shell configuration since it constitutes an hybrid optical nanosource. Following the work of Liaw, we introduce the average enhancement factor (AEF) [Liaw 2010].

The fluorescent enhancement factor for an emitter oriented along the arbitrary direction \mathbf{u} is

$$\alpha_{\mathbf{u}}(\mathbf{r}, \omega_{exc}, \omega_{em}) = \frac{|\mathbf{u} \cdot \mathbf{E}(\mathbf{r}, \omega_{exc})|^2}{|\mathbf{E}_{\mathbf{i}}(\omega_{exc})|^2} \eta_{\mathbf{u}}(\mathbf{r}, \omega_{em}), \quad (4.14)$$

where $\eta_{\mathbf{u}} = \gamma_{\mathbf{u}}^R / \gamma_{\mathbf{u}}$ is the quantum yield associated to the dipole orientation \mathbf{u} .

Assuming randomly oriented emitters at location \mathbf{r} , we calculate the mean enhancement factor over 4π sr:

$$\alpha(\mathbf{r}, \omega_{exc}, \omega_{em}) = \frac{3}{4\pi} \int_{\alpha=0}^{\pi} \int_{\beta=0}^{2\pi} \alpha_{\mathbf{u}}(\mathbf{r}, \omega_{exc}, \omega_{em}) \sin \alpha \, d\alpha \, d\beta \quad (4.15)$$

where the factor 3 ensures a unit enhancement factor for isolated emitters excited with a linearly polarized field.

The quantum yield $\eta_{\mathbf{u}}$ has to be carefully expressed.

The transition dipole orientation is $\mathbf{u} = (\sin \alpha \cos \beta, \sin \alpha \sin \beta, \cos \alpha)$. The quantum yield is [Colas des Francs 2002]

$$\begin{aligned} \eta_{\mathbf{u}} = & \sin^2 \alpha \cos^2 \beta \eta_x + \sin^2 \alpha \sin^2 \beta \eta_y + \cos^2 \alpha \eta_z \\ & + \sin^2 \alpha \cos \beta \sin \beta \eta_{xy} + \sin \alpha \cos \alpha \cos \beta \eta_{xz} + \sin \alpha \cos \alpha \sin \beta \eta_{yz}. \end{aligned} \quad (4.16)$$

Interestingly enough, the integration over the dipole orientation is analytical. After a few algebra, we achieve

$$\begin{aligned} \alpha(\mathbf{r}, \omega_{exc}, \omega_{em}) & \\ = & \frac{\eta_x(3E_x^2 + E_y^2 + E_z^2) + \eta_y(E_x^2 + 3E_y^2 + E_z^2) + \eta_z(E_x^2 + E_y^2 + 3E_z^2)}{5}. \end{aligned} \quad (4.17)$$

It is also useful to derive this expression in spherical coordinates (r, θ, ϕ) . With subscripts // and \perp indicating an orientation parallel or perpendicular to the particle surface, it writes

$$\alpha(\mathbf{r}, \omega_{exc}, \omega_{em}) = \frac{\eta_{//}(2E_r^2 + 4E_\theta^2 + 4E_\phi^2) + \eta_{\perp}(3E_r^2 + E_\theta^2 + E_\phi^2)}{5} \quad (4.18)$$

that leads to an analytic expression for (homogeneous, core-shell or onion-like) spherical particles, thanks to Mie expansion [Kim 1988, Sinzig 1994]. It is also possible to consider particle aggregate thanks to the generalized Mie theory [Stout 2008, Bonod 2010] and more complex structures using Maxwell equation solver [Girard 2005]. In the following, $\alpha(\mathbf{r}, \omega_{exc}, \omega_{em})$ is referred as the local fluorescence enhancement.

Average enhancement factor (AEF) Finally, the average enhancement factor of the whole doped volume V_0 can be numerically computed as

$$AEF = \frac{1}{V_0} \int_{doped} \int_{\theta=0}^{\pi} \int_{\phi=0}^{2\pi} \alpha(\mathbf{r}, \omega_{exc}, \omega_{em}) r^2 \sin \theta \, d\theta \, d\phi \, dr, \quad (4.19)$$

Where $d\Omega = \sin \theta \, d\theta \, d\phi$ corresponds to the infinitesimal solid angle in the direction (θ, ϕ) . It is also useful to define an average enhancement factor associated to a doped shell layer which depends only on the distance d to the metallic surface:

$$\alpha_{layer}(\omega_{exc}, \omega_{em}, d) = \frac{1}{4\pi} \int_{\Omega} \alpha(\mathbf{r}, \omega_{exc}, \omega_{em}) \, d\Omega. \quad (4.20)$$

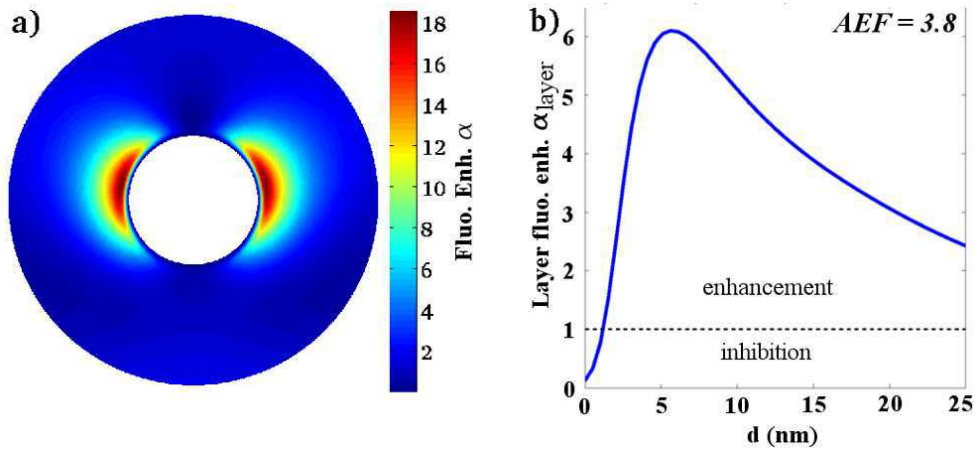


Figure 4.11: a) Fluorescence enhancement $\alpha(\mathbf{r})$ (Eq. 4.18) near a silver particle for randomly oriented molecules near a 80nm silver particle. b) Layer fluorescence enhancement α_{layer} (Eq. 4.20). The horizontal line indicates the enhancement/inhibition threshold. The average fluorescence enhancement of the whole doped layer (25 nm) is $AEF = 3.8$. The excitation and emission wavelengths are $\lambda_{exc} = 532\text{nm}$ and $\lambda_{em} = 560\text{nm}$, respectively. The embedding medium is PMMA (optical index $n_B = 1.5$).

Figure 4.11a) shows the local fluorescent enhancement $\alpha(\mathbf{r})$ map (Eq. 4.18) for randomly oriented emitters dispersed in PMMA near a silver spherical particle. It follows the dipolar mode profile and the maximum enhancement reaches $\alpha \approx 18$. Since the random dye orientation is taken into account, this value is lower than that obtained previously for a perpendicular dye $\alpha_{\perp} \approx 29$. Note that the dipolar mode profile is slightly tilted from the incident polarization axis. This feature is explained by the interference of the scattered field with the incoming plane wave [Härtling 2007].

Figure 4.11c) shows the layer fluorescence enhancement α_{layer} (Eq. 4.20) and the average fluorescence factor (AEF) of the dye doped core-shell particle. The overall $AEF \approx 4$ is optimized given the absorption and emission wavelengths of the dye molecule. This factor takes into account inhomogeneous excitation in the dipolar modes as well as the distance dependence of the emission rate. This system will be used as a reference system in the following.

4.3.2 Rare earth doped plasmonic core shell

In previous sections, we have introduced two important parameters in order to quantify plasmon/emitters interactions in a core-shell particle: layer-averaged enhancement factor α_{layer} , and shell-averaged enhancement factor $\tilde{\alpha}$. We have estimated maximum AEF achievable for a Rh6G doped core-shell $Ag@SiO_2$. These

factors will now allow us to characterize the effect of a metal nanoparticle on the luminescence of RE ions.

In this part, we study luminescence enhancement for two rare earth ions used in different application domains: Eu^{3+} used for example as biolabel for its emission in visible spectrum and Er^{3+} , as main active medium for amplification at the telecom wavelength $1.55 \mu\text{m}$. Quantum efficiency of these emitters is closed to unity. Therefore, as explained in the previous section, plasmon resonance can not much increases this factor.

Lanthanide absorption, based on 4f transitions, in contrast, is very weak (around 10^{-20}cm^2). Therefore, the strongest exaltation is expected when matching the lanthanide absorption wavelength with the dipolar plasmon resonance. Emission of lanthanide is far from excitation wavelength and then is probably not much influenced by plasmon phenomenon [Pillonnet 2012] contrary to dye molecules where the stokes shift ($\lambda_{em} - \lambda_{exc}$) is weaker (see previous section).

4.3.2.1 Emission in the visible

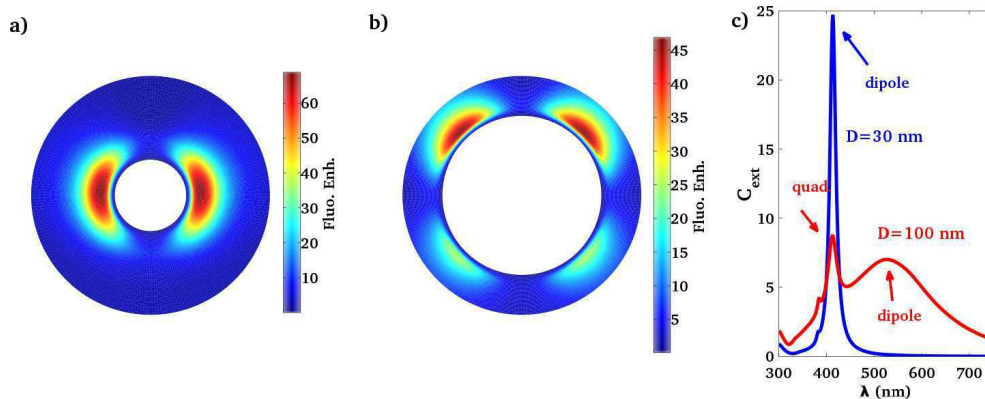


Figure 4.12: Eu^{3+} fluorescence enhancement map $\alpha(\mathbf{r})$ near a 30nm(a) or 100nm (b) silver particle. c) Extinction efficiency of a 30nm (blue line) or 100nm (red line) silver particle. The dipolar and quadrupolar resonance are indicated for the two particle diameters. Excitation and emission wavelength are $\lambda_{exc} = 415\text{nm}$ and $\lambda_{em} = 620\text{nm}$, respectively. The embedding medium is SiO_2 ($n_1 = 1.5$).

In this section, we consider Europium Eu^{3+} system: this rare earth ion, usually UV/blue excited, has an emission spectrum in the red and with a maximum emission around 620nm. The excitation wavelength is $\lambda_{exc} = 415 \text{ nm}$.

Since their excitation is in the blue part of the visible spectrum, the coupling with a silver core is well suited. In our simulations, the core is surrounded by a

	d_{max}	Π/Π_0	γ^R/γ_0	γ^{NR}/γ_0	η	$max(\alpha)$	AEF
Rh6G- <i>Ag</i> (80 nm)@ <i>SiO</i> ₂	4nm	35	9.7	5	0.66	19	3.8
<i>Eu</i> ³⁺ - <i>Ag</i> (30 nm)@ <i>SiO</i> ₂	6nm	210	1.8	3	0.37	69	11.0
<i>Eu</i> ³⁺ - <i>Ag</i> (100 nm)@ <i>SiO</i> ₂	5.5nm	90	8	4.2	0.66	47	6.7

Table 4.2: Comparison of excitation and emission rates calculated at the optimum distance for Rh6G and *Eu*³⁺ doped silver core-shell. The local fluorescence enhancement is slightly below the product of excitation rate \times apparent quantum yield since it obeys to Eq. 4.18.

*SiO*₂ shell (optical index $n_1 = 1.5$) which is doped with rare earth ions. Then, we consider the core-shell particle is hosted in a bulk *SiO*₂ matrix. Since emission of rare earth ions is quenched in polymer matrix, we consider a silica matrix of same index as PMMA so that direct comparison with the previous dye molecule case is possible. Note that this luminescent doped core-shell *Ag*@*SiO*₂ can be chemically synthesized [Aslan 2007, van Wijngaarden 2011].

Figure 4.12a) is a map of the fluorescence exaltation $\alpha(\mathbf{r})$ achieved near a 30 nm sized silver sphere. This optimum core diameter D allows to achieve a maximum local fluorescent enhancement $\alpha(\mathbf{r}) \approx 70$. This enhancement is mainly an improvement of absorption process: we have a strong exaltation Π/Π_0 of the excitation field which is resonant with the dipolar mode. Since the emission wavelength is far from the particle resonances (see the extinction efficiency in Fig. 4.12c), radiative decay rate is practically not affected by the presence of the plasmonic nanostructure.

Table 4.2 represents the excitation and decay rates for dye-doped and RE-doped silver core-shell. We have previously seen that for dye molecules exhibiting a low Stokes shift, large particles lead to the strongest effect since it corresponds to large resonances and coupling to the dipolar plasmon enhances both the excitation and radiative emission rates [Bharadwaj 2007b]. Differently, small metal core sizes are preferred to enhance RE emission. This leads to a strong excitation rate increase that compensate the decrease of the apparent quantum yield.

Moreover, we investigate a second possibility for enhancing RE emission. Considering a silver core diameter which is about $D = 100\text{nm}$, we obtain an other optimum enhancement $max(\alpha)$ which reaches ≈ 50 as depicted on Figure 4.12b). This result is also reported in table 4.2. Compared to the previous case, the excitation rate Π decreases (210 to 90), but, on the other hand, the quantum yield η increases (37% to 67%). The excitation field couples to the plasmon quadrupolar mode ($\lambda = 415\text{ nm}$) and radiative rate is also efficiently enhanced by coupling to the dipolar mode ($\lambda \approx 525\text{ nm}$, Fig. 4.12c). This leads to intermediate luminescence enhancement as compared to dye-doped system and dipolar assisted RE luminescence enhancement (see table 4.2).

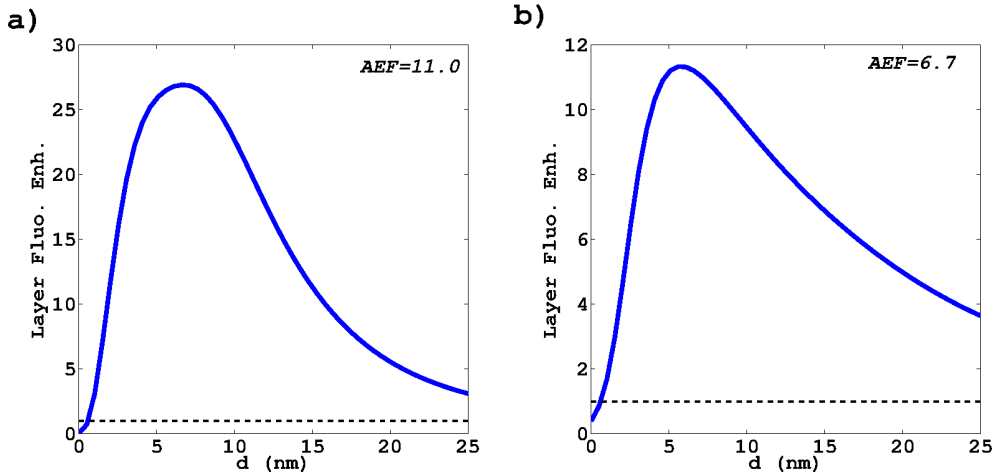


Figure 4.13: Layer fluorescence enhancement of a Eu^{3+} doped core-shell $Ag@SiO_2$ spherical particle. with a silver core of 30 nm (a) or 100 nm (b). The average fluorescence enhancement of the whole doped layer (25 nm) is reported on each figure. The horizontal line indicates the enhancement/inhibition threshold.

Having determined the optimal nanoparticle sizes in order to enhance red luminescent of randomly oriented Eu^{3+} ions, we now estimate the enhancement of a doped shell layer (Eq. 4.20). Figure 4.13 shows the evolution of the layer fluorescence enhancement α_{layer} with distance d between metal and emitters and the average fluorescence enhancement factor for the whole Eu^{3+} doped shell for the two optimal core sizes. For a 30nm metal core and doped shell thickness of 25nm, we achieve a strong $AEF = 11$. This high AEF relies on the strong field enhancement at the plasmon dipolar mode resonance. Quenching is limited to emitters very closed to the metal surface.

Finally, it is not possible to achieve fluorescence enhancement for these rare earth doped systems using a gold core (even by optimizing the core diameter), since the dipolar resonance cannot be tuned to the excitation wavelength $\lambda = 415$ nm (see Fig. 4.8).

4.3.2.2 Emission in the near infrared

Erbium ions (Er^{3+}), are widely used for optical amplification for telecom applications, since they emit around $\lambda_{em} = 1.55$ μm . We investigate the possibility to enhance their IR emission signal using core-shell configuration. In Erbium Doped Fiber Amplifier (EDFA), they are usually pumped at 800 nm or 900 nm wavelength in order to limit non radiative losses present with high energy pumping. We consider excitation wavelength $\lambda_{exc} = 800$ nm and emission at $\lambda_{em} = 1.55$ μm . We calculate an optimum particle size of 130 nm metal core, either for $Ag@SiO_2$ or $Au@SiO_2$. We find a maximum local enhancement up to 8.5 (6.5) fold near a silver (gold) particle resulting from the coupling of both excitation field and emission radiation to

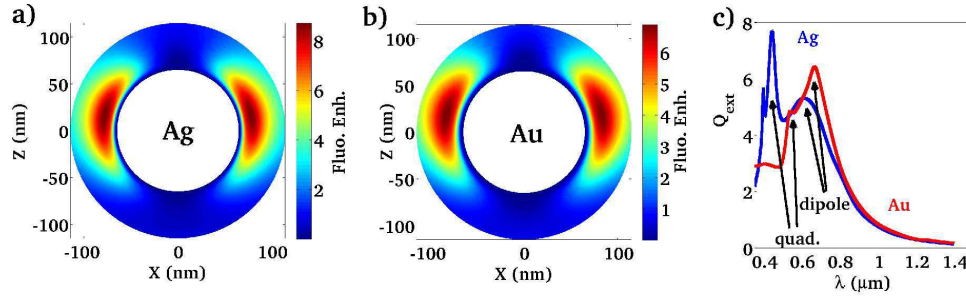


Figure 4.14: Fluorescence enhancement $\alpha(\mathbf{r})$ of randomly oriented Er^{3+} near a 130nm silver (a) or gold (b) particle. The excitation and emission wavelengths are $\lambda_{exc} = 800$ nm and $\lambda_{em} = 1.55$ μm , respectively. c) Extinction efficiency of a 130nm silver (blue line) or gold (red line) particle. The embedding medium is SiO_2 (optical index $n_B = 1.5$).

the large dipolar resonance (see Fig. 4.14c)). Our simulation gives then an average enhancement factor (AEF) of 2.3 (1.7) for the whole doped volume V_0 for a silver (gold) core surrounded by a 25nm doped shell layer. This poor AEF is due to the position of excitation and emission wavelengths of Er^{3+} , both far from plasmon resonance. Since it is possible to shift the longitudinal dipolar plasmon resonance towards NIR spectrum with anisotropic nanoparticle presenting high aspect ratio, we propose to optimize the AEF with an anisotropic metal core.

4.3.2.3 Nanorod core-shell particle

Spherical core-shell present limited AEF and imposes to use large particle in order to red shift the plasmon dipolar resonance to match the Er^{3+} absorption spectrum. Another possibility is to use elongated particle with high aspect ratio [Mertens 2009, Liaw 2012]. In this last section, we investigate nanorod core shell and estimate the fluorescent enhancement (Eqs (4.17) and (4.19)). In this goal, the excitation electric field \mathbf{E} and emission rates γ_i need to be evaluated at any location in the doped layer. In case of arbitrary structure, they can be calculated thanks to the Green's dyad technique [Girard 2005, Baffou 2008, Girard 2008]. Liaw *et al* investigate similar structures using multiple multipole method [Liaw 2012]. However, they limit the computation to a plane (emitter orientation is constrained in 2 dimensions and only the doped layer inside the plane of incidence is considered).

Figure 4.15 represents the fluorescent enhancement near a metal nanorod. The

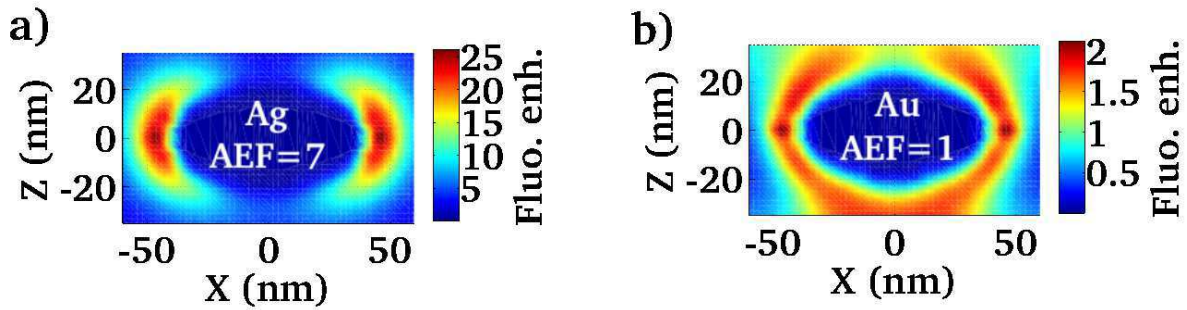


Figure 4.15: Fluorescence enhancement of randomly oriented Er^{3+} near a silver (a) or gold (b) nanorod ($70 \text{ nm} \times 20 \text{ nm}$). The incident electric field \mathbf{E}_i is polarized along the rod long axis. The excitation and emission wavelength are $\lambda_{exc} = 800 \text{ nm}$ and $\lambda_{em} = 1.55 \mu\text{m}$, respectively. The AEF over the whole (3D) 25nm doped shell is indicated. The two first nm of the shell are undoped (SiO_2 spacer). The embedding medium is SiO_2 (optical index $n_B = 1.5$)

aspect ratio of the rod has been fixed in order to match the particle resonance and the excitation field ($\lambda_{exc} = 800 \text{ nm}$). The volume of the nanorod is the same as for a 30nm spherical particle so that the achieved enhancement factor can be compared to the visible regime (Fig. 4.12a). The tip effect strengthen the field exaltation at the dipolar resonance [Mertens 2009] and we observe a fluorescence enhancement up to 25 fold near the rod tip. Finally, we achieve an average enhancement factor $AEF = 7$ for the whole doped shell, comparable to the visible regime (Fig. 4.13). No improvement occurs for a gold core ($AEF = 1$, Fig. 4.15b) due to higher losses.

4.4 Conclusion

In this chapter, we have quantified the luminescence enhancement of Rhodamine 6G or rare earth doped plasmonic core-shell nanoparticles. For rare-earth doped core-shell nanoparticles, the highest enhancement is achieved when the particle dipolar resonance matches the excitation wavelength. The enhancement mainly comes from excitation rate exaltation by coupling to the dipolar mode whereas emission process is weakly modified. This results is different from Rh6G dye-doped particle where a low Stokes shift between emission and excitation wavelengths leads to choose a particle resonance in between to enhance both excitation and radiative rates. We demonstrate average enhancement factor of the fluorescence on the overall RE-doped silver nanoparticle $AEF = 11$ and $AEF = 7$ in the visible and near-infrared regime, respectively. Gold core leads to lower effect due to larger losses.

Finally, RE doped plasmonic particles constitutes bright optical nanosources. Colloidal solutions of doped plasmonic particles can be synthesized and would benefit for *e.g* biolabelling [Bouzigues 2011], solar cells [Timmerman 2008] or photodynamic cancer therapy [Wang 2011].

Single photon source in a tip-surface junction

Contents

5.1	Photon anti-bunching near a plasmonic nanostructure. . . .	78
5.2	Nitrogen Vacancy color center in nanodiamonds	79
5.3	Optical addressing of individual NV centers	81
5.3.1	Experimental set-up and methods	81
5.3.2	Photodynamics of NV nanodiamonds	84
5.4	Nanodiamond NV center emission in a tip-surface junction	86
5.4.1	SNOM Tip	87
5.4.2	Tip perturbed single photon source emission	89
5.5	Conclusion	92

In chapter 4, we have discussed the fluorescence enhancement of an ensemble of emitters coupled to a metal nanoparticle. Since the LSP mode can be confined on a strongly subwavelength scale, it is possible to reduce the number of emitter to unity. It is of great interest since one emitter can emit only one photon at a time (photon antibunching) so that it constitutes a single photon source. The control of single photon source emission is a challenging topic since it is a key component for quantum information devices [Fausto 2011].

Numerous recent works discussed the acceleration of a single photon source by coupling to metal nanoparticles [Akimov 2007, Schietinger 2009, Marty 2010, Cuche 2010, Busson 2012b, Greffet 2013, Beams 2013]. Moreover, several theoretical works propose to couple efficiently a single emitter source into a photonic fiber via a SPP [Bouhelier 2003, Chang 2006, Chen 2009, Mivelle 2010, Grosjean 2013] as well as a few experimental demonstration [Taminiau 2007, Mivelle 2012].

In this chapter, we describe preliminary studies on single photon source emission in a tip-surface junction. Indeed, we expect efficient coupling of single photon source to an optical fiber (the tip) that could lead to a versatile configuration for single photon source manipulation [Neu 2012, Thompson 2013].

First, we discuss briefly the mechanisms involved in the coupling of a single emitter and a MNP with a simple model. Then, we characterize single photon emission of one nanodiamond NV center deposited on glass substrate. Finally, we present our results obtained with metal coated optical tapered fibers put close to the nanocrystals.

5.1 Photon anti-bunching near a plasmonic nanostructure.

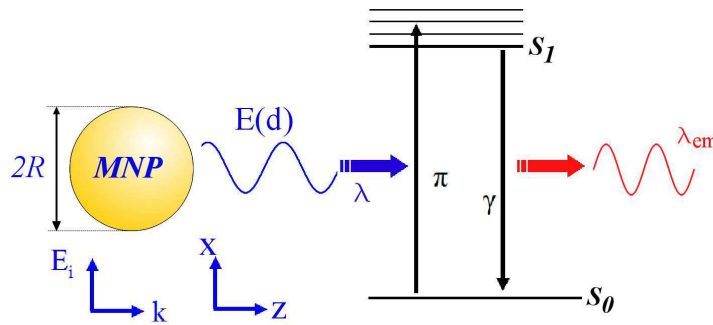


Figure 5.1: Schematic view of the coupling between a metal nanoparticle and a single quantum emitter. The Jablonsky diagram illustrates the energy levels of the emitter. The coupled system is excited by the incident electric field \mathbf{E}_i .

Here, we introduced a simple description of the photon antibunching process involving a single photon emitter. Photon antibunching is a quantum phenomenon which is revealed by the second order autocorrelation function [Orrit 2002]:

$$g^2(\Delta t) = \frac{\langle I(t)I(t + \Delta t) \rangle}{\langle I(t) \rangle^2}. \quad (5.1)$$

The $g^2(\Delta t)$ function represents the probability for a source to emit a second photon at a delay time Δt following a first emission. In order to express this function, we need to determine the photodynamic of the emitter. We consider the emitter as a two level system (TLS) already introduced in chapter 4 (Fig. 5.1). For low excitation power, the source photodynamic is well described by its population equation [Novotny 2006, Marty 2010]. We note N_0 and N_1 the population of the ground state \mathbf{S}_0 and the excited state \mathbf{S}_1 , respectively

$$\begin{aligned} \frac{dN_1(t)}{dt} &= \Pi N_0 - \gamma N_1, \\ &= \Pi - (\Pi + \gamma) N_1 \end{aligned} \quad (5.2)$$

where we used $N_0 + N_1 = 1$. Assuming the initial condition $N_1(t = 0) = 0$ (the TLS has emitted a photon), the above differential equation has the solution

$$N_1(\Delta t) = N_1(\infty) [1 - e^{-(\Pi + \gamma)\Delta t}], \quad (5.3)$$

where $N_1(\infty) = \Pi/(\Pi + \gamma)$ is the steady-state population. $g^2(\Delta t)$ function expresses as [Novotny 2006]

$$g^2(\Delta t) = \frac{N_1(\Delta t)}{N_1(\infty)}, \quad (5.4)$$

Hence, we obtain

$$g^2(\Delta t) = 1 - e^{-|\Delta t|/\tau_{AB}}, \quad (5.5)$$

where $\tau_{AB} = 1/(\Pi + \gamma)$ is the antibunching time between two consecutive photon emission.

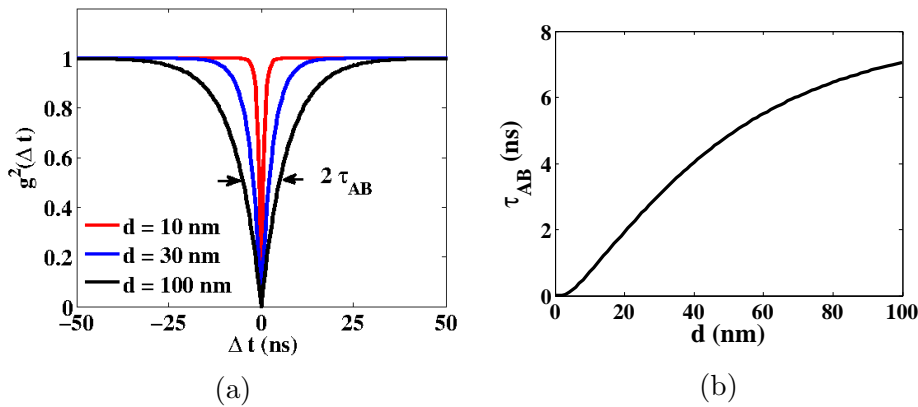


Figure 5.2: a) Second order autocorrelation function $g^2(\Delta t)$ according to the distance d with a 80nm gold particle. b) Calculation of the photon antibunching time τ_{AB} as a function of the coupling distance d . The emitter has an intrinsic decay rate $\gamma_0 = 1/10 \text{ ns}^{-1}$ and the free pumping rate is fixed as $\Pi_0 = 1/50 \text{ ns}^{-1}$.

Figure 5.2a depicts the second order autocorrelation function. The $g^2(\Delta t)$ has a typical dip of width twice the antibunching time τ_{AB} . $g^2(\Delta t = 0)$ equals 0 because the source emits photon one by one. In chapter 4, we have expressed the enhancement of both the excitation rate Π and the decay rate γ as a function of the distance d to a gold nanoparticle (see figures 4.4 and 4.5). We have observed that $\Pi(d)$ and $\gamma(d)$ increase when the emitter is at short separation distances d . Hence, the antibunching time $\tau_{AB} = 1/(\Pi + \gamma)$ is reduced for small coupling distances (see Figure 5.2). This means that the rate of single photon emission is accelerated (except for very short distances where the emission is quenched).

5.2 Nitrogen Vacancy color center in nanodiamonds

In this section, we briefly describe the characteristics of NV (Nitrogen Vacancy) centers in diamond lattice. They are punctual defects in the lattice, formed by a substitutional Nitrogen atom combined with an adjacent carbon vacancy

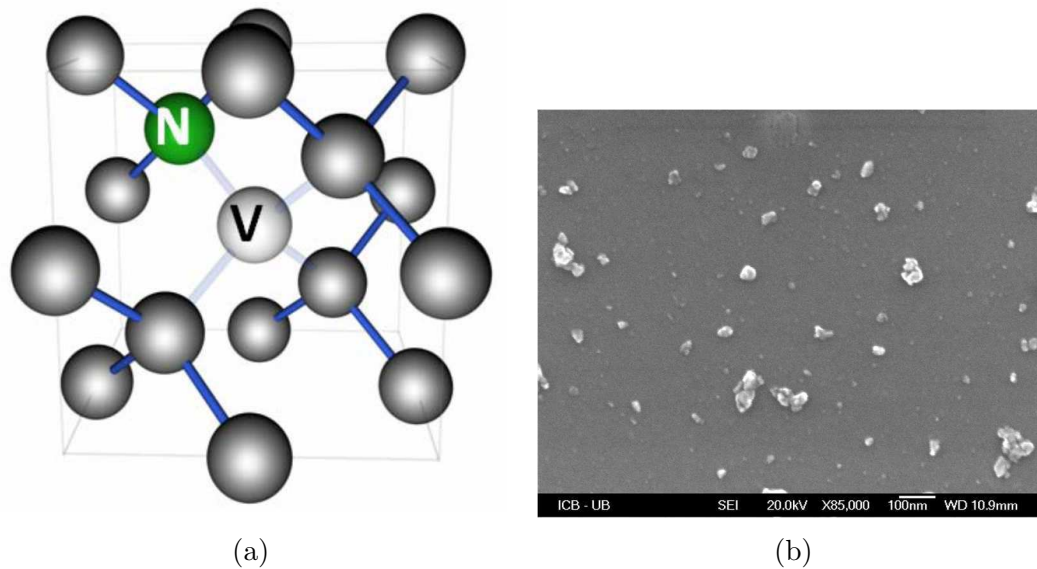


Figure 5.3: a) Description of Nitrogen Vacancy (NV) center in the lattice of a diamond. Reprinted by permission from Macmillan Publishers Ltd: Nature (Ref. [Balasubramanian 2008]), copyright (2008). b) Scanning electron micrograph of nanodiamonds spread on glass.

as shown in Figure 5.3a. NV centers are promising emitters because they are highly photo-stable and have quantum yield close to unity even at room temperature. For these reasons, NV center in diamonds would be of interest in many applications as quantum cryptography, optoelectronics and biolabeling [Wrachtrup 2006, Praver 2008, Young 2009, Faklaris 2009, Mochalin 2012]. Usually, heavy fabrication processes need to be performed for implanting NV centers inside diamonds [Zheng 2010, Beveratos 2002, Meijer 2005]. Nevertheless, it is possible to find such color centers embedded inside synthetic nano-diamonds.

Figure 5.3b depicts a scanning electron microscopy picture of a synthetic nanodiamonds solution spin-coated on glass substrate. The nano-diamond powder (Microdiamant AG, Switzerland) was previously diluted in de-ionized water and then mixed with polyvinyl alcohol (0.3% weight) in order to avoid the formation of aggregates on the substrate. The nanocrystals have an average size of 25 nm.

Figure 5.4 presents two typical spectra measured on two different nanodiamonds. NV centers exhibit two charge states: a neutrally charged NV^0 , with a zero-phonon line (ZPL) emitting at 575nm [Mita 1996] (Fig 5.4a) and a negatively charged NV^- , with a zero-phonon line emitting at 637nm [Davies 1976] (Fig 5.4b). Both the types of NV centers are detected on the same sample. Furthermore, NV centers are photochromic: it is possible to switch them between different charge states by exciting them at a strong illumination power (typically at the dozen of mW at a 532 nm wavelength laser injected in a high numerical aperture lens) [Zheng 2010].

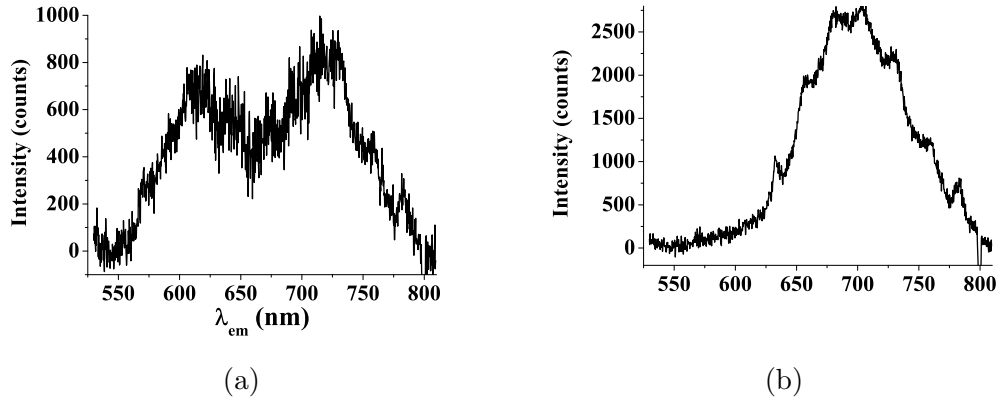


Figure 5.4: Emission spectra of a) neutrally charged NV center (NV^0) with a ZPL at 575nm, b) negatively charged NV center (NV^-) with a ZPL at 637nm.

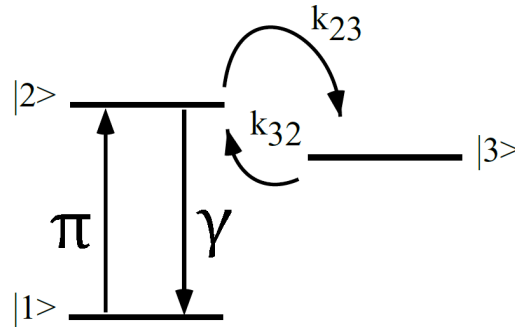


Figure 5.5: Jablonsky diagram of NV centers which takes into account his metastable state $|3\rangle$. Figure extracted from Ref. [Beveratos 2002].

Usually, NV centers are modeled as three levels systems [Zheng 2010, Beveratos 2002, Kurtsiefer 2000] (see on Fig.5.5). Such emitters present a metastable state denoted $|3\rangle$. The lifetime of the metastable state ($1/k_{23}$) is typically of few hundreds of nanoseconds for NV^- centers [Dräbenstedt 1999]. It has been found that NV^0 centers exhibit a metastable state lifetime of a few microseconds [Gali 2009].

5.3 Optical addressing of individual NV centers

5.3.1 Experimental set-up and methods

Figure 5.6 depicts the optical set-up used for optical characterization of nanodiamonds. The system is a home-built confocal microscope with a high numerical aperture objective lens ($NA = 1.49$). The excitation source is a continuous wave (CW) laser emitting at 532nm wavelength. The exciting beam is removed from detection by using a dichroic mirror (DM). In order to acquire the second

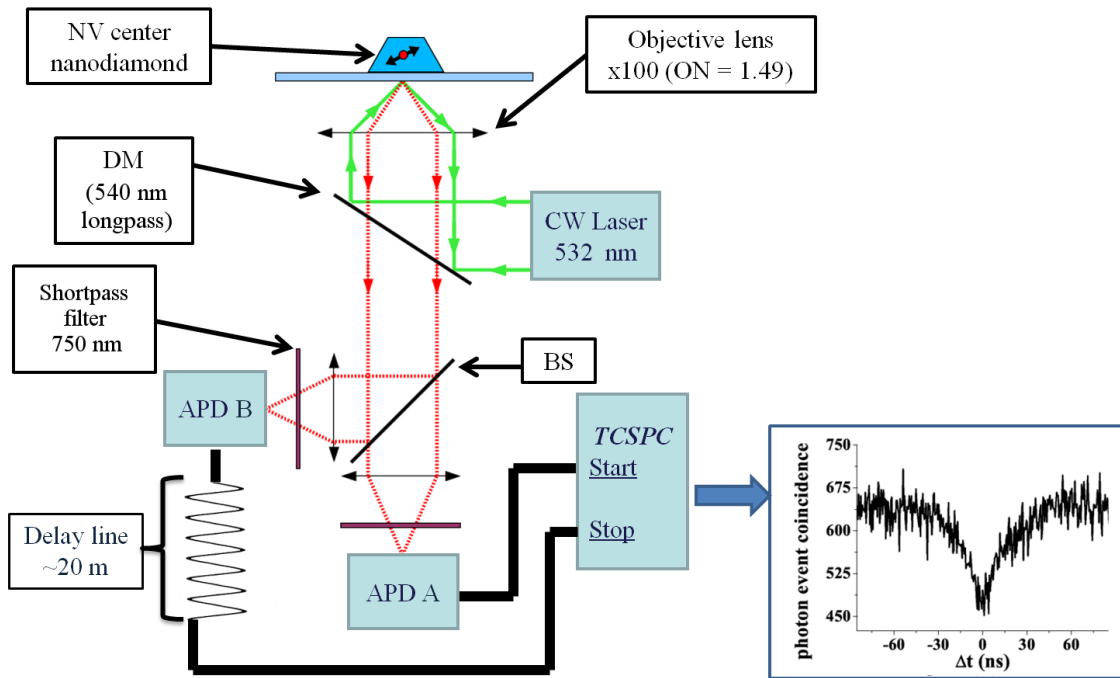


Figure 5.6: Confocal microscopy setup. NV center nanodiamonds are spread on glass substrate and are excited with a CW laser beam. Fluorescence emission is divided by a beam splitter (BS) and collected on two APDs (*Excelitas Technologies SPCM-AQRH-15*). APD A and B are connected to a time-correlated single photon counting card (TCSPC, *Picoquant-PicoHarp 300*) for $g^2(\Delta t)$ acquisition. DM: dichroic mirror.

order autocorrelation function $g^2(\Delta t)$, the microscope output (light collection) is upgraded with a Hanbury, Brown and Twiss set-up.

The latter consists of a 50/50 beam splitter (BS) which separates the signal of fluorescence into two channels. Each channel is focused on an avalanche photodiode (APD) for collecting photon events. In order to prevent optical cross talk between the two detectors, a longpass optical filter is inserted in front of the APDs. We use a time correlated single photon counting (TCSPC - *Picoquant GmbH*) card for acquiring histograms. The *start* signal is triggered when a photon is detected on APD A. An electrical delay line is inserted by using about 20 m long electrical cable between the APD B and the *stop* channel of the TCSPC card. This introduces a lagtime of ≈ 85 ns in order to count photon events before the origin (delay time $\Delta t < 0$). Finally, we obtain a typical symmetric auto-correlation histogram $C(\Delta t)$ as depicted in the inset of Fig. 5.6.

In order to obtain the 2^{nd} order autocorrelation function $g^2(\Delta t)$, it is necessary to

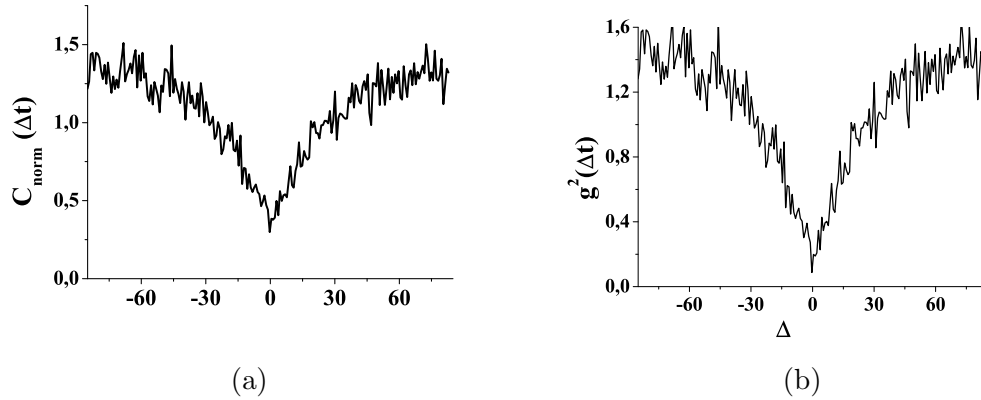


Figure 5.7: Numerical treatments of a second order autocorrelation histogram. a) Normalized histogram and b) background corrected histogram giving the $g^2(\Delta t)$ function.

first normalize the measured coincidence function $C(\Delta t)$ as follows (see Fig. 5.7a)

$$C_{norm}(\Delta t) = \frac{C(\Delta t)}{N_A N_B T \Omega}, \quad (5.6)$$

where T is the duration of the acquisition (typically a few dozen of minutes). N_A and N_B are the number of photon per second detected by the APD A and B, respectively. $\Omega = 512$ ps is the width of the time bin channel. Then, the signal is background corrected according to

$$g^2(\Delta t) = \frac{C_{norm}(\Delta t) - (1 - \rho^2)}{\rho^2}; \quad (5.7)$$

$$\rho = \frac{S}{S + B},$$

where S and B are the signal and the background magnitudes, respectively. Signal and background magnitudes are estimated from a Gaussian fitting on the scanning confocal picture. Finally, we obtain the 2nd order autocorrelation function $g^2(\Delta t)$ as shown in Fig. 5.7b). For delay time $\Delta t = 0$, the g^2 value is close to zero ($g^2(\Delta t = 0) < 0.5$), we ensure that only one emitter (*i.e.* one NV center) is detected during the acquisition. Indeed, second order autocorrelation function enables the quantification of the number N of emitters within the confocal volume:

$$g^2(\Delta t = 0) = 1 - \frac{1}{N}. \quad (5.8)$$

Nevertheless, background correction on Fig. 5.7b) lacks of accuracy since the curve does not tend to unity for long delay time $\Delta t \mapsto \infty$. Indeed, we suspect residual graphite layers remained on the nanocrystals before acquisitions so that they generate parasites during photon events collection.

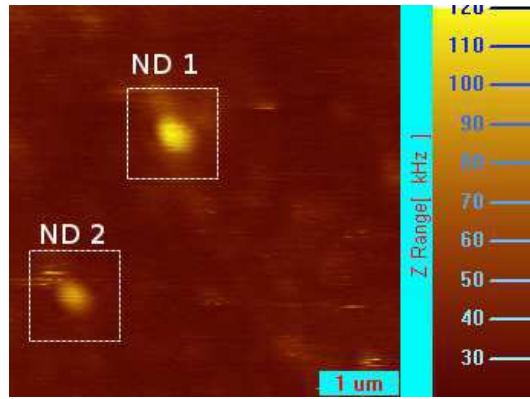


Figure 5.8: Scanning confocal imaging of two NV center nanodiamonds of interest.

5.3.2 Photodynamics of NV nanodiamonds

Figure 5.8 is a scanning confocal picture performed on the sample described in section 5.2 (see Fig. 5.3b). Two nanodiamonds of interest are detected (namely ND 1 and ND 2). Figure 5.9 depicts the $g^2(\Delta t)$ functions acquired for each nanodiamond. The curves confirm that each of the nanodiamonds contain only one NV center since $g^2(0) < 0.5$. We also measure their emission spectra (see Figure 5.4) and we deduce that ND 1 and ND 2 contain a NV^0 and a NV^- center respectively.

In addition, it is interesting to measure the $g^2(\Delta t)$ function for different excitation power as presented in Fig. 5.9. In case of a three levels system, the $g^2(\Delta t)$ function expresses [Beveratos 2000, Kurtsiefer 2000]

$$g^2(\Delta t) = [1 + c_1 e^{-\Delta t/\tau_1} + c_2 e^{-\Delta t/\tau_2}], \quad (5.9)$$

which the parameters τ_1, τ_2, c_1 and c_2 express

$$\begin{aligned} \tau_{1,2} &= 2/(A \pm \sqrt{A^2 - 4B}), \\ c_1 &= \frac{1 - \tau_1 k_{32}}{k_{32}(\tau_1 - \tau_2)}, \quad c_2 = -1 - c_1, \\ A &= \Pi + \gamma + k_{32} + k_{23}, \quad B = \Pi k_{23} + \Pi k_{32} + \gamma k_{32}. \end{aligned} \quad (5.10)$$

The above fit parameters rely on the whole photodynamics quantities: Π, γ, k_{32} and k_{23} as depicted on figure 5.5. Indeed, the fit equation 5.9 modelizes the metastable state (k_{23} and k_{32}) in addition to the excitation and the relaxation processes (Π and γ). For excitation powers $P_{exc} \geq 100 \mu\text{W}$, the equation 5.9 fits accurately the histograms acquired on Fig. 5.9. Nevertheless, regarding the complexity of the above equations, a fitting procedure of an individual $g^2(\Delta t)$ acquisition is not sufficient for determining the whole photodynamics quantities. In principle, a complete treatment (not performed in this thesis) requires to acquire $g^2(\Delta t)$ functions in a range of excitation power up to the dozen of mW, in order to set a

linear system of equations providing each the parameters [Beveratos 2002].

As it is observed on Figure 5.9, $g^2(\Delta t)$ functions exhibit bunching effects. This is due to metastable states lifetime ($1/k_{23}$) which decreases when the excitation power P_{exc} increases. Metastable state is prominent when the parameter τ_2 decreases so that it is related to the bunching effect. On the other hand, τ_1 is related to the antibunching effect since it tends to the antibunching time τ_{AB} at a weak excitation power.

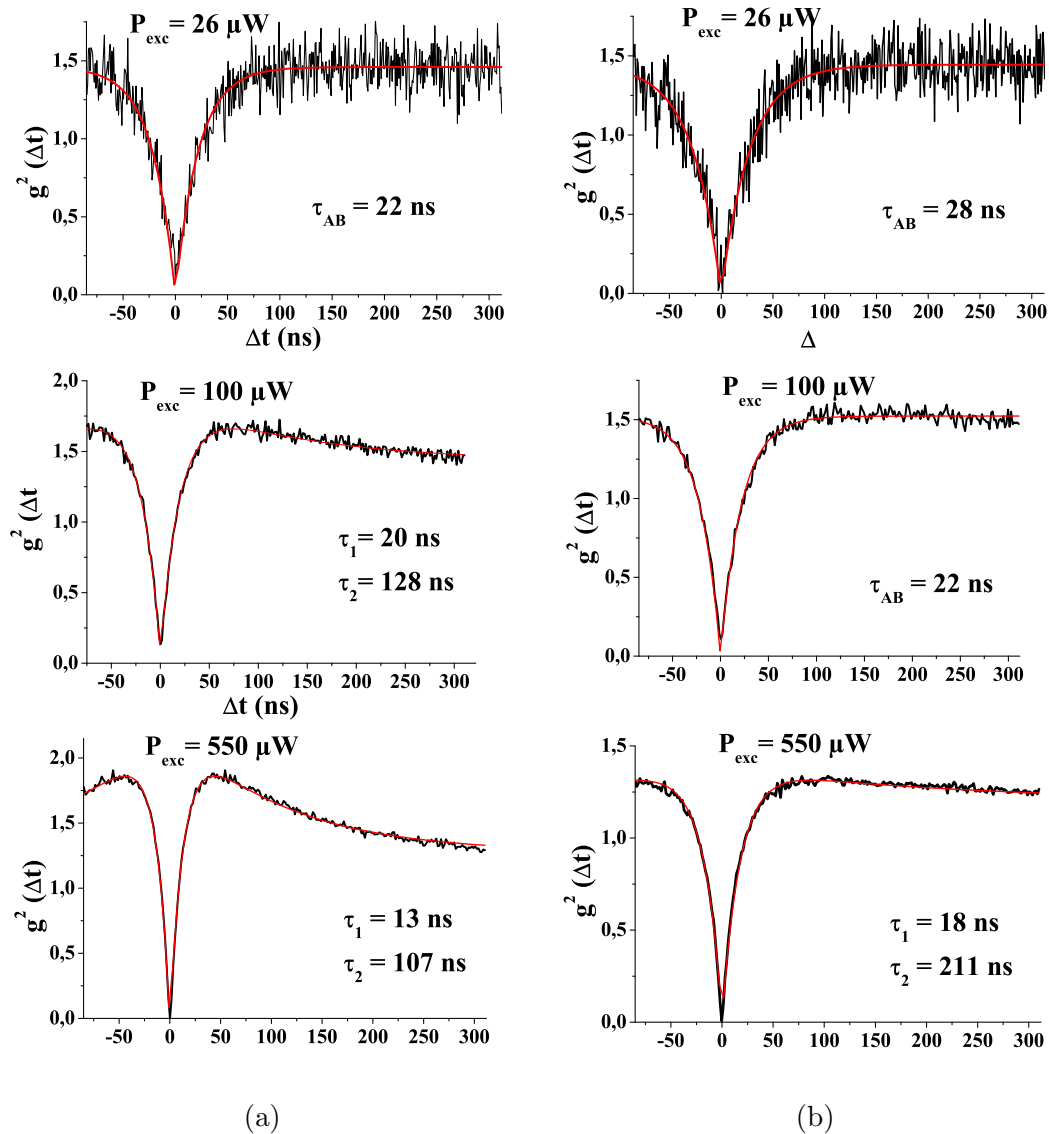


Figure 5.9: Acquisitions of $g^2(\Delta t)$ functions according to the excitation power P_{exc} . Left column: acquisitions on ND1 nanodiamond (NV^0 center). Right column: acquisitions on ND2 nanodiamond (NV^- center).

On the other hand, the NV centers exhibit a very long metastable state lifetime ($1/k_{23}$) under weak excitation in a such way that they can be modeled as two

levels systems. Indeed, for an excitation power $P_{exc} = 26\mu\text{W}$, the $g^2(\Delta t)$ functions are well fitted with the following expression

$$g^2(\Delta t) = 1 - e^{-\Delta t/\tau_{AB}}, \quad (5.11)$$

where the average antibunching time $\tau_{AB} = 1/(\Pi + \gamma)$ depends on the excitation rate Π and the decay rate γ . The NV^0 and the NV^- centers exhibit an antibunching time of $\tau_{AB} = 22$ ns and 28 ns, respectively.

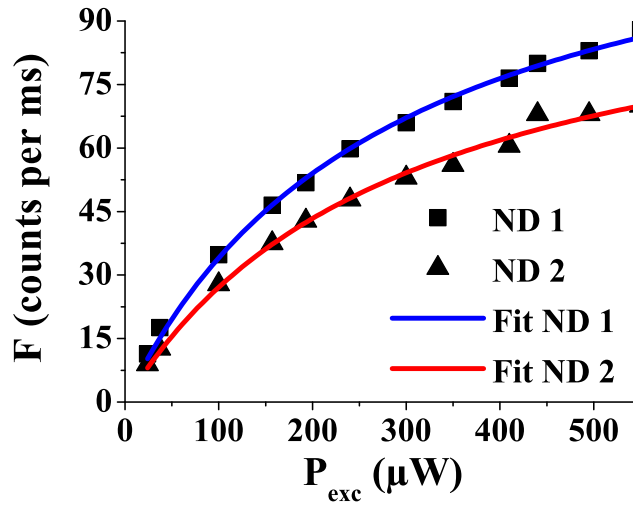


Figure 5.10: Saturation curves of each the NV centers embedded within ND 1 and ND 2. The NV fluorescence (F) is plotted as a function of the excitation power P_{exc} .

Finally, Figure 5.10 represents the saturation spectroscopy curves of the emitters. The experiments is performed with excitation powers P_{exc} below $550\mu\text{W}$. The fluorescence signal signal follows

$$F(P_{exc}) = F_{\infty} \frac{P_{exc}}{P_{exc} + P_{sat}}, \quad (5.12)$$

where P_{sat} is the saturation power. The fit leads to $P_{sat} = 280\mu\text{W}$ and $P_{sat} = 300\mu\text{W}$ for NV centers within ND 1 and ND 2, respectively. These values confirm that the $g^2(\Delta t)$ functions acquired with $P_{exc} = 26\mu\text{W}$ correspond to a weak excitation regime ($P_{exc} \ll P_{sat}$).

5.4 Nanodiamond NV center emission in a tip-surface junction

In this section, we investigate the coupling between a NV center and a metal coated tip of a scanning near-field optical microscope (SNOM). The set-up is

depicted in Fig. 5.11. A metal coated elongated fiber is raster scanned over a single nanodiamond. The tip head is shear-force controlled and is mounted above the confocal microscope presented in Fig. 5.6.

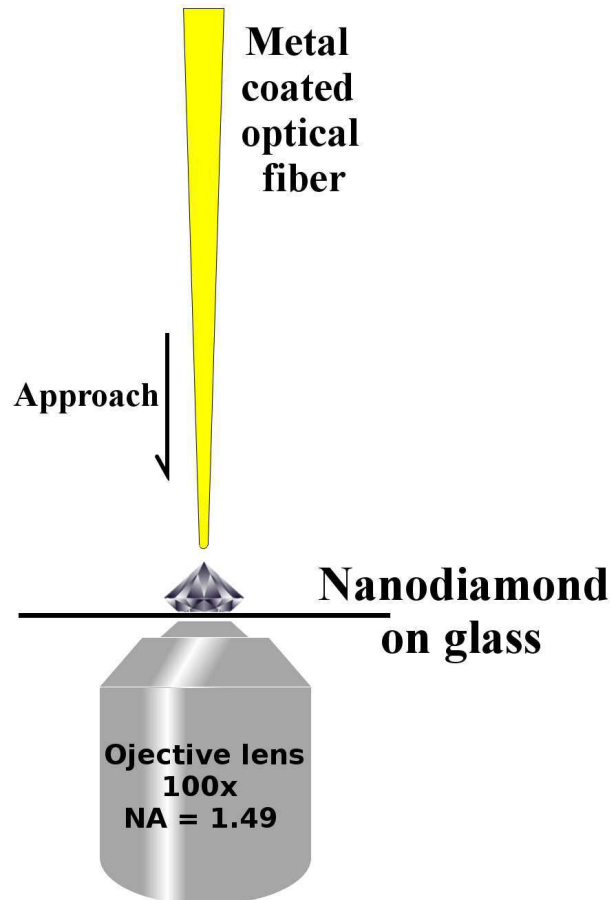


Figure 5.11: Schematic view of the experiment: a metal coated tapered optical fiber is raster scanned above a nanodiamond. Simultaneously, excitation and collection of the NV center fluorescence is done by a high numerical aperture objective lens mounted in the set-up depicted on Fig. 5.6.

5.4.1 SNOM Tip

Fabrication of the tip An optical fiber is first elongated by heating with a CO_2 laser and then pulling the fiber by a micropipette puller. Using the parameters given in table 5.1, we achieve tapered fiber with a radius of curvature of about 50 nm.

Then, the tapered fiber is coated with a metal thickness of 75nm. In the following, we test a gold coated and a silver coated fiber. The process is performed by physical vapor deposition (PVD) of silver or gold under vacuum (10^{-7} mbar). The coated

Table 5.1: Parameters used for the fabrication of tapered optical fibers with the model P-2000 micropipette puller (*Sutter Instrument*).

	Heat	Velocity	Delay	Pull
parameters values (arbitrary units)	310	15	123	220

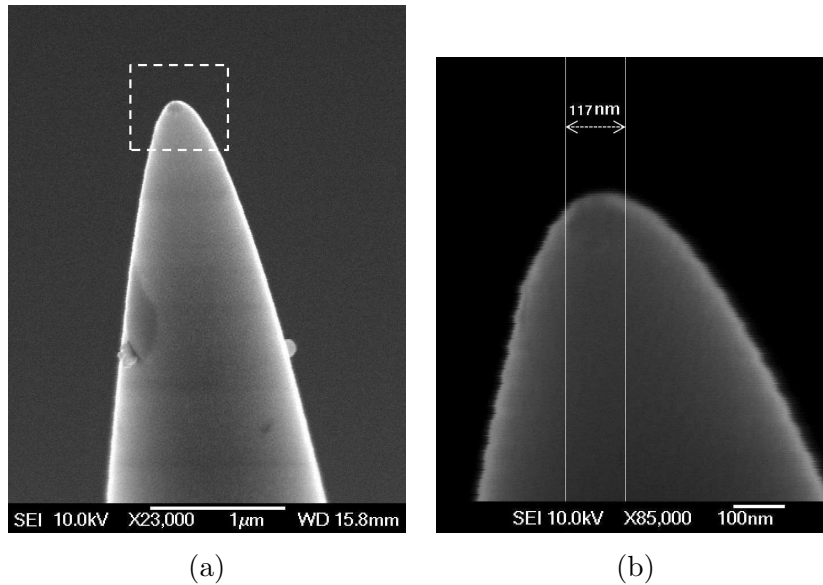


Figure 5.12: Scanning electron micrograph of a silver coated tapered optical fiber. The dashed square area in (a) corresponds to the zoomed picture on (b).

tip end radius is typically 100 – 150nm (see fig. 5.12).

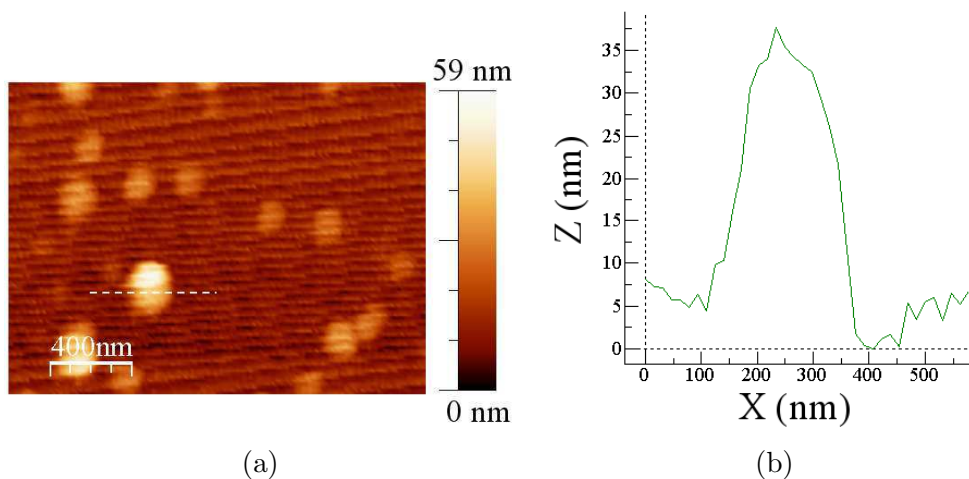


Figure 5.13: (a) Topographic image acquired above nanodiamonds spread on glass substrate. (b) Topographic profile along the dashed white line.

Shear-force controlled topographic imaging Since the elongated fiber distance to the sample is controlled using shear-force, this probe permits to acquire simultaneously topographic (Fig. 5.13a) and optical images. The figure 5.13b presents a topographic profile of a single nanodiamond. The height of the nanodiamonds is a few tens of nanometers. The profile width is roughly 200 nm which is in good agreement with the aperture size of the tip. Indeed, since the nanocrystal is smaller ($\phi \approx 25$ nm) than the tip end (≈ 150 nm), it acts as a local probe for the lateral dimension of the scanning tip.

5.4.2 Tip perturbed single photon source emission

We finally investigate single photon emission in a tip surface junction. We first characterize the luminescence of the metal coated tip since it could hide the nanocrystals emission. For this reason, the SNOM tip is raster scanned within the focal spot ($\lambda = 532$ nm). The photoluminescence of the silver coated tip is collected by an avalanche photodiode during the tip scan as shown in Fig. 5.14. We observe an Airy disk, as expected for a highly focused beam. The excitation power is $P_{exc} = 400\mu\text{W}$. The photoluminescence reaches 1MHz which is roughly 15 fold the fluorescence intensity of NV centers excited on similar conditions (see Fig. 5.10).

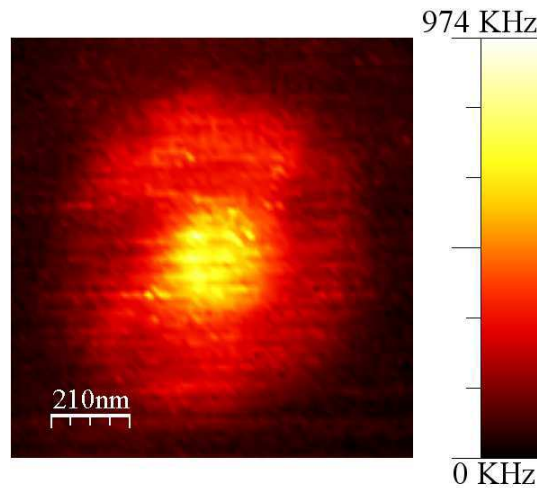


Figure 5.14: Photoluminescence of a silver tip scanning a laser beam focused with an objective lens ($NA = 1.49$). The excitation wavelength is 532nm and power is $P_{exc} = 400\mu\text{W}$. The luminescence is detected after a longpass filter ($\lambda > 540\text{nm}$).

Figure 5.15 depicts the photoluminescence spectra acquired for gold and silver coated tips. These spectra show that tip photoluminescence completely overlaps our spectral window of detection so that it is impossible to optically discriminate NV fluorescence from photoluminescence (*i.e.* by using optical filtering).

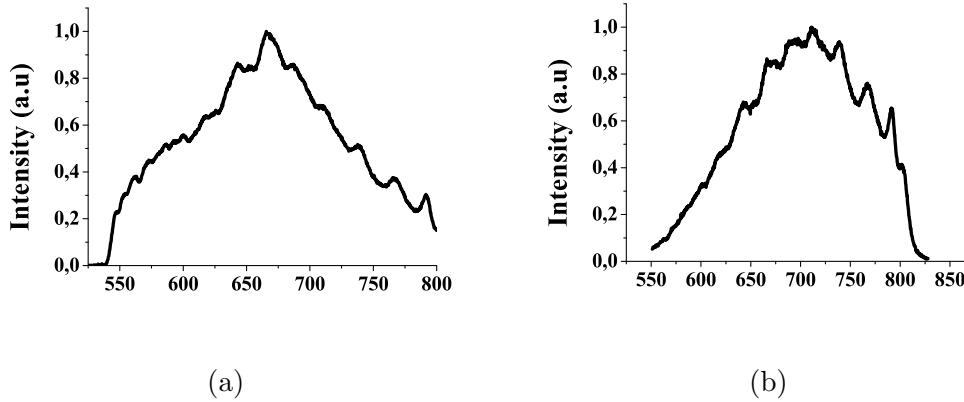


Figure 5.15: Photoluminescence spectra of (a) a gold and (b) a silver coated tapered optical fiber. The excitation wavelength is 532 nm.

We however try to study the nanodiamond emission in the tip-surface junction. Figure 5.16 presents the intensities collected according to the distance Z between the end of a gold tip and a NV center. The laser excitation power is fixed to $P_{exc} = 25\mu\text{W}$ so that weak excitation of the NV center is ensured. On Figure 5.16a both the gold tip photoluminescence and the NV fluorescence are collected (red curve). In order to subtract the gold tip photoluminescence, we collect the gold photoluminescence (black curve). The NV fluorescence signal (difference between red and black curves) is shown in Fig. 5.16b. We observe that NV fluorescence enhancement occurs on a large distance (over 300nm) probably because the tip is large.

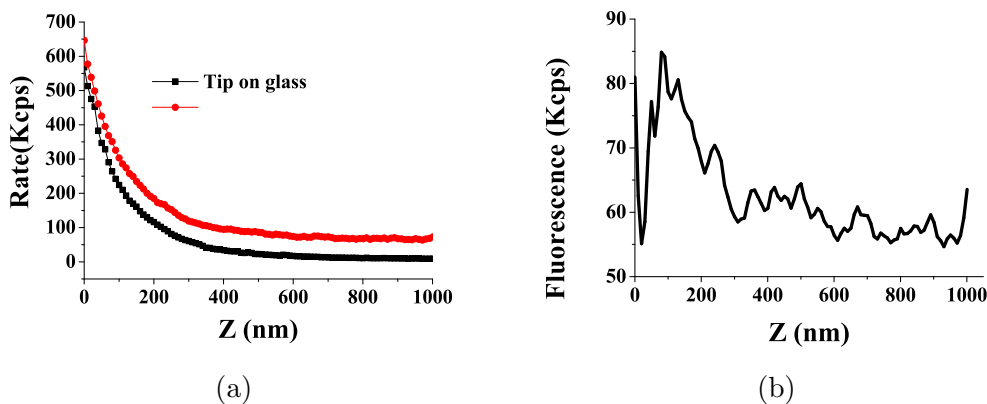


Figure 5.16: Approach curves of a gold tip at an excitation $P_{exc} = 25\mu\text{W}$. (a) The red curve is the signals measured for gold tip above a nanocrystal. The black one is tip photoluminescence measured far from the diamond. (b) Estimation of the NV fluorescence according to the distance Z between the diamond and the tip (difference between the red and black curves).

Figure 5.17 shows the measured correlation function $C(\Delta t)$ of a single nanocrystal (ND 2). We first acquire $C(\Delta t)$ in absence of the tip at an excitation power

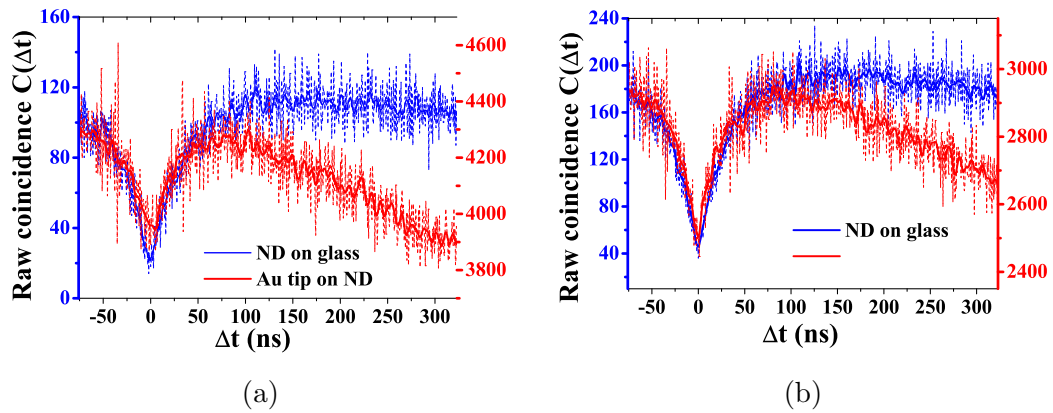


Figure 5.17: a) Coincidence $C(\Delta t)$ functions acquired with a metal coated tip put on a nanodiamond NV center. The tip is coated with gold in (a) and silver in (b). Excitation power is $P_{exc} = 30\mu\text{W}$. The blue curves correspond to measurements without tip and is taken as references for comparisons.

$P_{exc} = 30\mu\text{W}$. The antibunching time is $\tau_{AB} = 29$ ns in agreement with previous measurements (Fig. 5.9b).

Then, we approach the metal tip at the proximity of the particle. In order to increase the signal to noise ratio between NV fluorescence and metal photoluminescence, we approach the tip at a few hundred of nanometer from the side of the diamond. Figures 5.17b and 5.17a depict acquisitions performed with a gold and a silver tip, respectively. Unfortunately, the luminescence signal is still too high to permit correct normalization and background correction of the auto-correlation function (see Eq. 5.6 and 5.7). Nevertheless, the different behaviour with and without the tip let us think that the intercoupling rate to the triplet state $|3\rangle$ is increased in presence of the tip. We therefore perform qualitative fit with Eq. 5.9 (and an arbitrary offset). Table 5.2 reports the results of the fitting procedures. Two exponential components are required because bunching effects occur (see Eq. 5.9). However, the tip luminescence is too strong to achieve quantitative analysis so that tip optimization is needed. We have tried the plasmonic tips presented in Fig. 5.18 (realized by E. Dujardin, CEMES, Toulouse) but were not able to perform reproducible measurement due to the tip fragility. Similar configuration has been recently theoretically discussed for highly efficient single photon emission into an optical fiber [Chang 2006, Chen 2009].

Table 5.2: Results of the fitting procedures applied on $C(\Delta t)$ red curves (Fig. 5.17) exhibiting bunching effects.

Tip coating	τ_1 (ns)	τ_2 (ns)
Gold	56	170
Silver	42	270

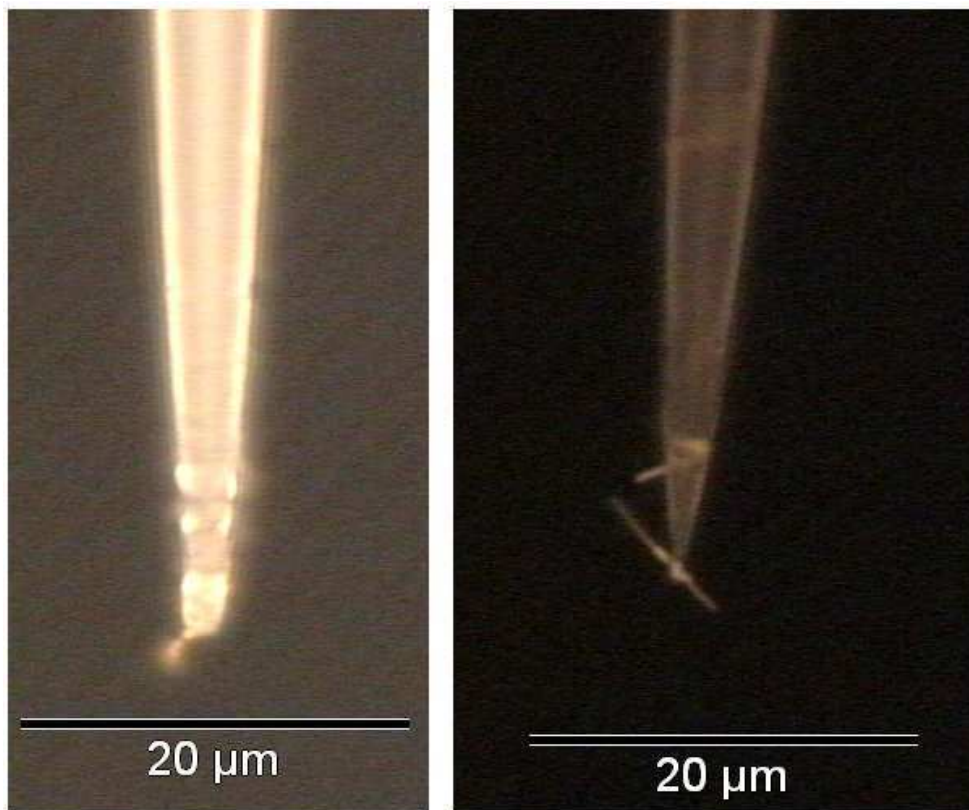


Figure 5.18: Optical micrograph of plasmonic tips engineered in CEMES, Toulouse (S. Viarbitskaya and E. Dujardin). An individual gold nanowire is glued on the taper of an optical fiber.

5.5 Conclusion

We have presented preliminary studies on the fluorescence NV centers in a surface-tip junction. We observe modification of the single photon source emission, for a small distance between the tip and the nanocrystal. However we were not able to quantitatively characterize the photodynamics of the coupled system due to bad signal-to-background ratio that originates from the tip luminescence. Nevertheless, the full set-up is now ready to investigate more efficient plasmonic tip. It will be done in a very near future (collaboration with E. Dujardin from CEMES, Toulouse).

Conclusion and perspectives

In this thesis manuscript, we have studied the control of fluorescence emission by utilizing plasmonic nanostructures. Contrary to bulk-optical cavities, a plasmonic system supports modes with poor quality resonances (low Q factors), but, have a spatial extension squeezed at the nanoscale (mode volume $V < (\lambda/n)^3$).

As seen in Chapter 2, it is possible to transpose the principle of an optical cavity (as a Fabry-Perot or a photonic crystal cavity) to an in-plane plasmonic cavity. The system studied allows to confine surface plasmons of a flat metal film by placing two SPP reflectors at the borders of the cavity. We have probed the local density of state (LDOS) of the cavity surface waves by measuring the fluorescence lifetime of dye molecules placed inside the cavity and estimate a maximum decay rate enhancement of 7 with a $\lambda_{SPP}/2$ sized cavity whereas the quantum yield remains close to unity. However, the quality factor remains weak since our SPP reflectors were metal gratings so that they have a large spectral bandwidth. This is of interest for emission control at room temperature.

In Chapter 3, we have investigated metal nanoparticles and the characteristics of localized surface plasmon (LSP). We used the quasi-static approximation on a Drude metal particle in order to express LSPs mode volume with a clear physical understanding. Then, we investigate quantitatively the characteristics of individual modes. The dipolar mode quality factor decreases with the size of the particle because radiation losses increase. On the other hand, the quadrupolar mode has a quality factor which remains constant ($Q \sim 40$) since its losses are limited by absorption. For the computation of the mode volumes, we have used a definition based on the Purcell factor expression. Furthermore, we have compared these results with a definition of the mode volume which is based on the energy confinement. We found that the two definitions do not match, in despite of our efforts for discriminating the near field and the far field coupling. Nevertheless, a recent work reconciles the two definitions by considering a mode volume as a complex number. Mode volume definition is helpful in designing original structures such as the spaser or structures leading to strong coupling regime.

But, Purcell factor includes both radiative and non-radiative channels. For a plasmonic system (metal nanoparticles, film or plasmonic crystals), the Purcell factor rigorously corresponds to an emitter in contact to the metal surface, where the fluorescence quenches. In Chapter 4, Purcell factor has not been taken as the relevant parameter for optimizing the fluorescence enhancement. In fact, we obtained significant emission enhancements by increasing the excitation and the radiative processes, also optimal coupling distances were estimated. We have simulated the fluorescence enhancement of Rh6G dye molecules inside a silver core-shell particle. Enhancement was optimized by tuning the LSP dipolar reso-

nance near the excitation and the emission wavelengths because Rh6G molecules exhibit a low Stokes-shift. Then, we have considered silver- Eu^{3+} core-shell. Eu^{3+} ions have a large stokes-shift, the dipolar particle resonance has to be tuned to the excitation wavelength. It is also possible to couple the excitation wavelength to the quadrupolar particle mode and emission to the dipolar mode. Global exaltation of about 10 is achievable by engineering the particle shape, size and material.

Additionally, we have reported in Chapter 5, our preliminary experiments with a plasmonic tip put nearby a nanodiamond NV center. We used gold and silver coated optical fibers with an apex radius of roughly 150 nm. We observed that $g^2(\Delta t)$ functions exhibited a pronounced metastable state meaning an increase of the k_{23}/k_{32} ratio. Our metal coated tips generate huge photoluminescence so that other experiments are required. In particular, we have not studied the coupling of the fluorescence emission inside the coated tapered fiber which is of key interest for efficient control of a single photon source.

APPENDIX A

Appendix 1

In this appendix, we derive the expression of mode quality factor and effective volume for a spherical particle embedded in homogeneous background of optical index $n_B = \sqrt{\varepsilon_B}$. For a better description of the metal optical properties, we include the contributions of the bound electrons into the metal dielectric constant

$$\varepsilon_m = \varepsilon_\infty - \frac{\omega_p^2}{\omega^2 + i\Gamma_{abs}\omega}. \quad (\text{A.1})$$

A.1 Effective polarisability associated to n^{th} SPP mode

The n^{th} multipole tensor moment of the metallic particle is given by

$$\mathbf{p}^{(n)} = \frac{4\pi\varepsilon_0\varepsilon_B}{(2n-1)!!} \alpha_n \nabla^{n-1} \mathbf{E}_0, \quad (\text{A.2})$$

$$\alpha_n = \frac{n(\varepsilon_m - \varepsilon_B)}{n\varepsilon_m + (n+1)\varepsilon_B} R^{(2n+1)}, \quad (\text{A.3})$$

The resonance angular frequency is then $\omega_n = \omega_p \sqrt{n/[n\varepsilon_\infty + (n+1)\varepsilon_B]}$ ($\omega_\infty = \omega_p/\sqrt{\varepsilon_\infty + \varepsilon_B}$). Finally, the effective polarisability, including finite size effects write [Colas des Francs 2009a]:

$$\alpha_n^{eff} = \left[1 - i \frac{(n+1)k_B^{2n+1}}{n(2n-1)!!(2n+1)!!} \alpha_n \right]^{-1} \alpha_n. \quad (\text{A.4})$$

with $k_B = n_B k$ the wavenumber in the background medium.

Considering a Drude metal, we achieve a simple approximated expression for α_n^{eff} near a resonance

$$\begin{aligned} \alpha_n^{eff} &\underset{\omega_n}{\sim} \frac{(2n+1)\varepsilon_B}{n\varepsilon_\infty + (n+1)\varepsilon_B} \frac{\omega_n}{2(\omega_n - \omega) - i\Gamma_n} R^{2n+1}, \\ \Gamma_n &= \Gamma_{abs} + \Gamma_n^{rad}, \\ \Gamma_n^{rad} &= \frac{(2n+1)\varepsilon_B}{n\varepsilon_\infty + (n+1)\varepsilon_B} \omega_n \frac{(n+1)(k_B R)^{2n+1}}{n(2n-1)!!(2n+1)!!}, \end{aligned} \quad (\text{A.5})$$

So that the quality factor expression $Q = \omega_n/\Gamma_n$ remains valid but with the corrected expressions for resonance frequency ω_n and total dissipation rate Γ_n .

A.2 Effective volumes

The total coupling strength of a dipolar emitter to the spherical metallic particle, embedded in n_B medium expresses [Colas des Francs 2008, Colas des Francs 2009a]:

$$\frac{\gamma_{tot}^\perp}{n_B \gamma_0} \approx \frac{3}{2} \frac{1}{(k_B z_0)^3} \sum_{n=1}^{\infty} \frac{(n+1)^2}{z_0^{(2n+1)}} \text{Im}(\alpha_n^{eff}), \quad (\text{A.6})$$

$$\frac{\gamma_{tot}^\parallel}{n_B \gamma_0} \approx \frac{3}{4} \frac{1}{(k_B z_0)^3} \sum_{n=1}^{\infty} \frac{n(n+1)}{z_0^{(2n+1)}} \text{Im}(\alpha_n^{eff}). \quad (\text{A.7})$$

The coupling strength to the n^{th} mode is

$$\frac{\gamma_n^\perp}{n_B \gamma_0} \approx \frac{3}{2} \frac{1}{(k_B z_0)^3} \frac{(n+1)^2}{z_0^{(2n+1)}} \text{Im}(\alpha_n^{eff}), \quad (\text{A.8})$$

$$\approx \frac{3}{\omega_n} \left(\frac{\lambda}{n_B} \right)^3 \frac{R^{2n+1}}{4\pi z_0^3} \frac{(2n+1)\varepsilon_B}{n\varepsilon_\infty + (n+1)\varepsilon_B} \frac{(n+1)^2}{z_0^{(2n+1)}} Q_n.$$

$$\frac{\gamma_n^\parallel}{n_B \gamma_0} \approx \frac{3}{4} \frac{1}{(k_B z_0)^3} \frac{n(n+1)}{z_0^{(2n+1)}} \text{Im}(\alpha_n^{eff}), \quad (\text{A.9})$$

$$\approx \frac{3}{\omega_n} \left(\frac{\lambda}{n_B} \right)^3 \frac{R^{2n+1}}{8\pi z_0^3} \frac{(2n+1)\varepsilon_B}{n\varepsilon_\infty + (n+1)\varepsilon_B} \frac{n(n+1)}{z_0^{(2n+1)}} Q_n,$$

and the mode effective volume is deduced from comparison to the Purcell factor (Eq. 3.35)

$$V_n^\perp = \frac{n\varepsilon_\infty + (n+1)\varepsilon_B}{(2n+1)\varepsilon_B} \frac{4\pi z_0^{2n+4}}{(n+1)^2 R^{2n+1}}, \quad (\text{A.10})$$

$$V_n^\parallel = \frac{n\varepsilon_\infty + (n+1)\varepsilon_B}{(2n+1)\varepsilon_B} \frac{8\pi z_0^{2n+4}}{n(n+1) R^{2n+1}}. \quad (\text{A.11})$$

Finally, we define the mode volume as

$$\frac{1}{V_n} = \frac{1}{3V_n^\perp(R)} + \frac{2}{3V_n^\parallel(R)}, \quad (\text{A.12})$$

$$V_n = \frac{n\varepsilon_\infty + (n+1)\varepsilon_B}{(2n+1)\varepsilon_B} \frac{9}{(2n+1)(n+1)} V_0. \quad (\text{A.13})$$

All the expressions obtained in this appendix reduce to the simple analytical case discussed in the main text for $\varepsilon_\infty = 1$ (bound electrons contribution neglected) and $\varepsilon_B = 1$ (background medium is air).

Bibliography

- [Agió 2012] Mario Agió. *Optical antennas as nanoscale resonators*. *Nanoscale*, vol. 4, no. 3, pages 692–706, February 2012. (Cited on page 52.)
- [Akimov 2007] A V Akimov, A Mukherjee, C L Yu, D E Chang, A S Zibrov, P R Hemmer, H Park and M D Lukin. *Generation of single optical plasmons in metallic nanowires coupled to quantum dots*. *Nature*, vol. 450, pages 402–406, 2007. (Cited on pages 15 and 77.)
- [Anger 2006] Pascal Anger, Palash Bharadwaj and Lukas Novotny. *Enhancement and Quenching of Single-Molecule Fluorescence*. *Phys. Rev. Lett.*, vol. 96, no. 11, page 113002, 2006. (Cited on pages 15 and 67.)
- [Armani 2003] D K Armani, T J Kippenberg, S M Spillane and K J Vahala. *Ultra-high-Q toroid microcavity on a chip*. *Nature*, vol. 421, no. 6926, pages 925–8, February 2003. (Cited on page 8.)
- [Asano 2006] Takashi Asano, Bong-Shik Song and Susumu Noda. *Analysis of the experimental Q factors (~ 1 million) of photonic crystal nanocavities*. *Optics Express*, vol. 14, no. 5, page 1996, March 2006. (Cited on page 9.)
- [Aslan 2007] Kadir Aslan, Meng Wu, Joseph R Lakowicz and Chris D Geddes. *Fluorescent Core-Shell Ag@SiO₂ Nanocomposites for Metal-Enhanced Fluorescence and Single Nanoparticle Sensing Platforms*. *J. Am. Chem. Soc.*, vol. 129, pages 1524–1525, 2007. (Cited on pages 67 and 71.)
- [Baffou 2008] G Baffou, C Girard, E Dujardin, G. Colas des Francs and O Martin. *Molecular quenching and relaxation in a plasmonic tunable nanogap*. *Physical Review B*, vol. 77, page 121101(R), 2008. (Cited on page 73.)
- [Balasubramanian 2008] Gopalakrishnan Balasubramanian, I Y Chan, Roman Kolesov, Mohammad Al-Hmoud, Julia Tisler, Chang Shin, Changdong Kim, Aleksander Wojcik, Philip R Hemmer, Anke Krueger, Tobias Hanke, Alfred Leitenstorfer, Rudolf Bratschitsch, Fedor Jelezko and Jörg Wrachtrup. *Nanoscale imaging magnetometry with diamond spins under ambient conditions*. *Nature*, vol. 455, no. 7213, pages 648–51, October 2008. (Cited on page 80.)
- [Ban] <http://www.bangslabs.com>. (Cited on pages 21 and 26.)
- [Bär 2010] S Bär, A Chizhik, R Gutbrod, F Schleifenbaum and A Meixner. *Microcavities: tailoring the optical properties of single quantum emitters*. *Anal Bioanal Chem*, vol. 396, pages 3–14, 2010. (Cited on page 4.)

- [Barnes 1998] W L Barnes. *Fluorescence near interfaces: the role of photonic mode density*. Journal of Modern Optics, vol. 45, pages 661–699, 1998. (Cited on page 12.)
- [Barnes 2003] William L Barnes, Alain Dereux and Thomas W Ebbesen. *Surface plasmon subwavelength optics*. Nature, vol. 424, no. 6950, pages 824–30, August 2003. (Cited on page 10.)
- [Barthes 2011] J Barthes, G Colas des Francs, A Bouhelier, J-C. Weeber and A Dereux. *Purcell factor for a point-like dipolar emitter coupling to a 2D-plasmonic waveguide*. Physical Review B (Brief Reports), vol. 84, page 73403, 2011. (Cited on pages 27, 32 and 35.)
- [Barthes 2013] Julien Barthes, Alexandre Bouhelier, Alain Dereux and Gérard Colas des Francs. *Coupling of a dipolar emitter into one-dimensional surface plasmon*. Scientific reports, vol. 3, page 2734, September 2013. (Cited on page 32.)
- [Beams 2013] Ryan Beams, Dallas Smith, Timothy W Johnson, Sang-Hyun Oh, Lukas Novotny and A Nick Vamivakas. *Nanoscale Fluorescence Lifetime Imaging of an Optical Antenna with a Single Diamond NV Center*. Nano letters, vol. 13, no. 8, pages 3807–11, August 2013. (Cited on page 77.)
- [Benson 2006] T Benson, S Boriskina, P Sewell, A Vukovic, S Greedy and A Nosich. Frontiers in planar lightwave circuit technology, chapitre Micro-opti, pages 39–70. Springer (Berlin), 2006. (Cited on page 4.)
- [Bergman 2003] David J Bergman and Mark I Stockman. *Surface Plasmon Amplification by Stimulated Emission of Radiation: Quantum Generation of Coherent Surface Plasmons in Nanosystems*. Physical Review Letters, vol. 90, page 27402, 2003. (Cited on pages 16 and 48.)
- [Beveratos 2000] A. Beveratos, R. Brouri, J. P. Poizat and P. Grangier. *Bunching and antibunching from single NV color centers in diamond*. page 7, October 2000. (Cited on page 84.)
- [Beveratos 2002] Alexis Beveratos. *Réalisation expérimentale d’une source de photons uniques par fluorescence de centres colorés individuels dans le diamant ; application à la cryptographie quantique*. PhD thesis, Université Paris Sud - Paris XI, December 2002. (Cited on pages 80, 81 and 85.)
- [Bharadwaj 2007a] Palash Bharadwaj, Pascal Anger and Lukas Novotny. *Nanoplasmonic enhancement of single-molecule fluorescence*. Nanotechnology, vol. 18, no. 4, page 044017, January 2007. (Cited on page 67.)
- [Bharadwaj 2007b] Palash Bharadwaj and Lukas Novotny. *Spectral dependence of single molecule fluorescence enhancement*. Optics Express, vol. 15, pages 14266–14274, 2007. (Cited on page 71.)

- [Bharadwaj 2009] P Bharadwaj, B Deutsch and L Novotny. *Optical antennas*. Adv. Opt. Phot., vol. 1, pages 438–483, 2009. (Cited on page 11.)
- [Biteen 2005] Julie S Biteen, Domenico Pacifici, Nathan S Lewis and Harry A Atwater. *Enhanced radiative emission rate and quantum efficiency in coupled silicon nanocrystal-nanostructured gold emitters*. Nano letters, vol. 5, no. 9, pages 1768–73, September 2005. (Cited on page 13.)
- [Bohren 1983] Craig F. Bohren and Donald R. Huffman. *Absorption and scattering of light by small particles*. 1983. (Cited on pages 54 and 59.)
- [Bonod 2010] N Bonod, A Devilez, B Rolly, S Bidault and B Stout. *Ultracompact and unidirectional metallic antennas*. Physical Review B, vol. 82, page 115429, 2010. (Cited on pages 67 and 68.)
- [Bouhelier 2003] A Bouhelier, J Renger, M R Beversluis and L Novotny. *Plasmon-coupled tip-enhanced near-field optical microscopy*. Journal of Microscopy, vol. 210, pages 220–224, 2003. (Cited on page 77.)
- [Bouzigues 2011] Cedric Bouzigues, Thierry Gacoin and Antigoni Alexandrou. *Biological applications of rare-earth based nanoparticles*. ACS nano, vol. 5, no. 11, pages 8488–505, November 2011. (Cited on page 74.)
- [Buck 2003] J. Buck and H. Kimble. *Optimal sizes of dielectric microspheres for cavity QED with strong coupling*. Physical Review A, vol. 67, no. 3, page 033806, March 2003. (Cited on page 8.)
- [Bünzli 2007] Jean-Claude G. Bünzli, Steve Comby, Anne-Sophie Chauvin and Caroline D.B. Vandevyver. *New Opportunities for Lanthanide Luminescence*. Journal of Rare Earths, vol. 25, no. 3, pages 257–274, 2007. (Cited on page 57.)
- [Busson 2012a] M Busson, B Rolly, B Stout, J Wenger N. Bonod and S Bidault. *Photonic Engineering of Hybrid Metal-Organic Chromophores*. Angew. Chem. Int. Ed., vol. 51, pages 11083–11087, 2012. (Cited on page 15.)
- [Busson 2012b] Mickaël P Busson, Brice Rolly, Brian Stout, Nicolas Bonod and Sébastien Bidault. *Accelerated single photon emission from dye molecule-driven nanoantennas assembled on DNA*. Nature communications, vol. 3, page 962, January 2012. (Cited on pages 15 and 77.)
- [Carminati 2006] R. Carminati, J.-J. Greffet, C. Henkel and J.M. Vigoureux. *Radiative and non-radiative decay of a single molecule close to a metallic nanoparticle*. Optics Communications, vol. 261, no. 2, pages 368–375, May 2006. (Cited on pages 39 and 41.)
- [Castanié 2010] E Castanié, M Boffety and R Carminati. *Fluorescence quenching by a metal nanoparticle in the extreme near-field regime*. Optics letters, vol. 35, no. 3, pages 291–3, February 2010. (Cited on page 62.)

- [Celebrano 2010] M Celebrano, R Lettow, P Kukura, M Agio, A Renn, S Göttinger and V Sandoghdar. *Efficient coupling of single photons to single plasmons*. *Optics express*, vol. 18, no. 13, pages 13829–35, June 2010. (Cited on page 15.)
- [Chang 2006] D E Chang, A S Sørensen, P R Hemmer and M D Lukin. *Quantum Optics with Surface Plasmons*. *Physical Review Letters*, vol. 97, page 53002, 2006. (Cited on pages 77 and 91.)
- [Chen 2009] Xue-Wen Chen, Vahid Sandoghdar and Mario Agio. *Highly Efficient Interfacing of Guided Plasmons and Photons in Nanowires*. *Nano Letters*, vol. 9, pages 3756–3761, 2009. (Cited on pages 77 and 91.)
- [Chew 1987] H Chew. *Transitions rates of atoms near spherical surfaces*. *Journal of Chemical Physics*, vol. 87, pages 1355–1360, 1987. (Cited on page 61.)
- [Chu 1948] L J Chu. *Physical Limitations of OmniDirectional Antennas*. *Journal of Applied Physics*, vol. 19, page 1163, 1948. (Cited on page 52.)
- [Colas des Francs 2002] G Colas des Francs, C Girard and A Dereux. *Theory of near-field optical imaging with a single molecule as a light source*. *Journal of Chemical Physics*, vol. 117, pages 4659–4666, 2002. (Cited on page 68.)
- [Colas des Francs 2005] G Colas des Francs, C Girard, M Juan and A Dereux. *Energy transfer in near-field optics*. *Journal of Chemical Physics*, vol. 123, page 174709, 2005. (Cited on page 41.)
- [Colas des Francs 2008] G Colas des Francs, A Bouhelier, E Finot, J.-C. Weeber, A Dereux, C.Girard and E Dujardin. *Fluorescence relaxation in the near-field of a mesoscopic metallic particle: distance dependence and role of plasmon modes*. *Optics Express*, vol. 16, pages 17654–17666, 2008. (Cited on pages 15, 41, 45, 52, 64 and 96.)
- [Colas des Francs 2009a] G Colas des Francs. *Molecule non-radiative coupling to a metallic nanosphere: an optical theorem treatment*. *International Journal of Molecular Science*, vol. 10, pages 3931–3936, 2009. (Cited on pages 44, 45, 95 and 96.)
- [Colas des Francs 2009b] G Colas des Francs, J Grandidier, S Massenot, A Bouhelier, J.-C. Weeber and A Dereux. *Integrated plasmonic waveguides: a mode solver based on density of states formulation*. *Physical Review B*, vol. 80, no. 11, page 115419, 2009. (Cited on page 27.)
- [Cucho 2010] Aurélien Cucho, Oriane Mollet, Aurélien Drezet and Serge Huant. *‘Deterministic’ quantum plasmonics*. *Nano Letters*, vol. 10, pages 4566–4570, November 2010. (Cited on page 77.)

- [Davies 1976] G. Davies and M. F. Hamer. *Optical Studies of the 1.945 eV Vibronic Band in Diamond*. Proceedings of the Royal Society A: Mathematical, Physical and Engineering Sciences, vol. 348, no. 1653, pages 285–298, February 1976. (Cited on page 80.)
- [Deng 2011] Wei Deng, L Sudheendra, Jiangbo Zhao, Junxiang Fu, Dayong Jin, Ian M Kennedy and Ewa M Goldys. *Upconversion in NaYF₄:Yb, Er nanoparticles amplified by metal nanostructures*. Nanotechnology, vol. 22, no. 32, page 325604, August 2011. (Cited on page 67.)
- [Descrovi 2005] E Descrovi, V Paeder, L Vaccaro and H.-P. Herzig. *A virtual optical probe based on localized Surface Plasmon Polaritons*. Opt. Express, vol. 13, no. 18, pages 7017–7027, September 2005. (Cited on page 19.)
- [Djordjev 2002] K. Djordjev and R.D. Dapkus. *Microdisk tunable resonant filters and switches*. IEEE Photonics Technology Letters, vol. 14, no. 6, pages 828–830, June 2002. (Cited on page 8.)
- [Dräbenstedt 1999] A. Dräbenstedt, L. Fleury, C. Tietz, F. Jelezko, S. Kilin, A. Nizovtzev and J. Wrachtrup. *Low-temperature microscopy and spectroscopy on single defect centers in diamond*. Physical Review B, vol. 60, no. 16, pages 11503–11508, October 1999. (Cited on page 81.)
- [Drexhage 1970] K H Drexhage. *Influence of a dielectric interface on fluorescence decay time*. J. Lumin., vol. 1/2, pages 693–701, 1970. (Cited on page 12.)
- [Drezet 2008] A Drezet, A Hohenau, D Koller, A Stepanov, H Ditlbacher, B Steinberger, F R Aussenegg, A Leitner and J R Krenn. *Leakage radiation microscopy of surface plasmon polaritons*. Materials Science and Engineering B, vol. 149, pages 220–229, 2008. (Cited on page 14.)
- [Eghlidi 2009] Hadi Eghlidi, Kwang Geol Lee, Xue-Wen Chen, Stephan Götzinger and Vahid Sandoghdar. *Resolution and enhancement in nanoantenna-based fluorescence microscopy*. Nano letters, vol. 9, no. 12, pages 4007–11, December 2009. (Cited on page 15.)
- [Etchegoin 2010] Pablo G Etchegoin and Eric C Le Ru. *Resolving single molecules in surface-enhanced Raman scattering within the inhomogeneous broadening of Raman peaks*. Analytical chemistry, vol. 82, no. 7, pages 2888–92, April 2010. (Cited on page 14.)
- [Etchegoin 2011] Pablo G Etchegoin, Eric C Le Ru and A Fainstein. *Bi-analyte single molecule SERS technique with simultaneous spatial resolution*. Physical chemistry chemical physics : PCCP, vol. 13, no. 10, pages 4500–6, March 2011. (Cited on page 14.)
- [Faklaris 2009] Orestis Faklaris, Damien Garrot, Vandana Joshi, Jean-Paul Boudou, Thierry Sauvage, Patrick A. Curmi and François Treussart. *Comparison of*

- the photoluminescence properties of semiconductor quantum dots and non-blinking diamond nanoparticles. Observation of the diffusion of diamond nanoparticles in living cells.* Journal of the European Optical Society: Rapid Publications, vol. 4, page 09035, July 2009. (Cited on page 80.)
- [Fausto 2011] Rossi Fausto. Theory of Semiconductor Quantum Devices. 2011. (Cited on page 77.)
- [Feigenbaum 2007] E Feigenbaum and M Orenstein. *Modeling of Complementary (Void) Plasmon Waveguiding.* J. Lightwave Technol., vol. 25, no. 9, pages 2547–2562, September 2007. (Cited on page 27.)
- [Fort 2008] Emmanuel Fort and Samuel Grésillon. *Surface enhanced fluorescence.* Journal of Physics D: Applied Physics, vol. 41, no. 1, page 013001, January 2008. (Cited on pages 9 and 12.)
- [Gali 2009] Adam Gali. *Theory of the neutral nitrogen-vacancy center in diamond and its application to the realization of a qubit.* Physical Review B, vol. 79, no. 23, page 235210, June 2009. (Cited on page 81.)
- [Garcia-Vidal 2009] Francisco J Garcia-Vidal and Esteban Moreno. *Applied physics: Lasers go nano.* Nature, vol. 461, no. 7264, pages 604–5, October 2009. (Cited on pages 16 and 17.)
- [Gayral 1999] B. Gayral, J. M. Gerard, A. Lematre, C. Dupuis, L. Manin and J. L. Pelouard. *High-Q wet-etched GaAs microdisks containing InAs quantum boxes.* Applied Physics Letters, vol. 75, no. 13, page 1908, September 1999. (Cited on page 8.)
- [Gérard 1998] J. Gérard, B. Sermage, B. Gayral, B. Legrand, E. Costard and V. Thierry-Mieg. *Enhanced Spontaneous Emission by Quantum Boxes in a Monolithic Optical Microcavity.* Physical Review Letters, vol. 81, no. 5, pages 1110–1113, August 1998. (Cited on page 8.)
- [Girard 1995] C Girard, O J F Martin and A Dereux. *Molecular lifetime changes induced by nanometer scale optical fields.* Physical Review Letters, vol. 75, pages 3098–3111, 1995. (Cited on page 15.)
- [Girard 2005] Christian Girard. *Near fields in nanostructures.* Reports on Progress in Physics, vol. 68, no. 8, pages 1883–1933, August 2005. (Cited on pages 68 and 73.)
- [Girard 2008] C Girard, E Dujardin, G Baffou and R Quidant. *Shaping and manipulation of light fields with bottom-up plasmonic structures.* New Journal of Physics, vol. 10, page 105016 (22pp), 2008. (Cited on page 73.)
- [Gong 2009] Y Gong, J Lu, S Cheng, Y Nishi and Jelena Vuckovic. *Plasmonic enhancement of emission from Si-nanocrystals.* Applied Physics Letters, vol. 94, page 13106, 2009. (Cited on pages 19 and 20.)

- [González 2006] M U González, J.-C. Weeber, A.-L. Baudrion, A Dereux, A L Stepanov, J R Krenn, E Devaux and T W Ebbesen. *Design, near-field characterization, and modeling of 45 surface-plasmon Bragg mirrors*. Phys. Rev. B, vol. 73, no. 15, page 155416, 2006. (Cited on pages 22 and 24.)
- [González 2007] M U González, A L Stepanov, J.-C. Weeber, A Hohenau, A Dereux, R Quidant and J R Krenn. *Analysis of the angular acceptance of surface plasmon Bragg mirrors*. Optics Letters, vol. 32, pages 2704–2706, 2007. (Cited on page 23.)
- [Grandidier 2010] J Grandidier, G Colas des Francs, S Massenot, A Bouhelier, L Markey, J-C Weeber and A Dereux. *Leakage radiation microscopy of surface plasmon coupled emission: investigation of gain-assisted propagation in an integrated plasmonic waveguide*. Journal of microscopy, vol. 239, no. 2, pages 167–72, August 2010. (Cited on pages 14 and 20.)
- [Greffet 2010] Jean-Jacques Greffet, Marine Laroche and Francois Marquier. *Impedance of a Nanoantenna and a Single Quantum Emitter*. Physical Review Letters, vol. 105, page 117701, 2010. (Cited on page 41.)
- [Greffet 2013] Jean-Jacques Greffet, Cherif Belacel, Benjamin Habert, Florian Bigourdan, François Marquier, Jean-Paul Hugonin, Stefan Michaelis De Vasconcelos, Xavier Lafosse, Laurent Coolen, Catherine Schwob, Clémentine Javaux, Benoît Dubertret, Pascale Senellart and Agnès Maître. *Nanoantennas for single photon emission*. In 4th International Topical Meeting on Nanophotonics and Metamaterials, January 2013. (Cited on page 77.)
- [Grinberg 2012] P Grinberg, K Bencheikh, M Brunstein, A M Yacomotti, Y Dumeige, I Sagnes, F Raineri, L Bigot and J A Levenson. *Enhancement of a nano cavity lifetime by induced slow light and nonlinear dispersions*. Optics express, vol. 20, no. 24, pages 27403–10, November 2012. (Cited on page 9.)
- [Grosjean 2013] T Grosjean, M Mivelle, G W Burr and F I Baida. *Optical horn antennas for efficiently transferring photons from a quantum emitter to a single-mode optical fiber*. Optics express, vol. 21, no. 2, pages 1762–72, January 2013. (Cited on page 77.)
- [Gryczynski 2004a] Ignacy Gryczynski, Joanna Malicka, Zygmunt Gryczynski and Joseph R Lakowicz. *Radiative decay engineering 4. Experimental studies of surface plasmon-coupled directional emission*. Analytical biochemistry, vol. 324, no. 2, pages 170–182, January 2004. (Cited on page 13.)
- [Gryczynski 2004b] Ignacy Gryczynski, Joanna Malicka, Zygmunt Gryczynski and Joseph R Lakowicz. *Surface Plasmon-Coupled Emission with Gold Films*. The journal of physical chemistry. B, vol. 108, no. 33, pages 12568–12574, July 2004. (Cited on page 13.)

- [Härtling 2007] T Härtling, P Reichenbach and L M Eng. *Near-field coupling of a single fluorescent molecule and a spherical gold nanoparticle*. *Optics Express*, vol. 15, pages 12806–12817, 2007. (Cited on page 69.)
- [Hood 2000] C. J. Hood, T. W. Lynn, A. C. Doherty, A. S. Parkins and H. J. Kimble. *The Atom-Cavity Microscope: Single Atoms Bound in Orbit by Single Photons*. *Science*, vol. 287, no. 5457, pages 1447–1453, February 2000. (Cited on page 8.)
- [Hoogenboom 2009] J P Hoogenboom, G Sanchez-Mosteiro, G des Francs, D Heinis, G Legay, A Dereux and N F van Hulst. *The Single Molecule Probe: Nanoscale Vectorial Mapping of Photonic Mode Density in a Metal Nanocavity*. *Nano Letters*, vol. 9, no. 3, pages 1189–1195, 2009. (Cited on pages 28, 29 and 32.)
- [Imura 2006] Kohei Imura, Hiromi Okamoto, Mohammad K Hossain and Masahiro Kitajima. *Visualization of Localized Intense Optical Fields in Single Gold Nanoparticle Assemblies and Ultrasensitive Raman Active Sites*. *Nano Letters*, vol. 6, no. 10, pages 2173–2176, 2006. (Cited on page 14.)
- [Jackson 1998] J D Jackson. *Classical electrodynamics*. John Wiley & Sons, Hoboken, third édition, 1998. (Cited on page 39.)
- [Johnson 1972] P B Johnson and R W Christy. *Optical constants of the noble metals*. *Phys. Rev. B*, vol. 6, pages 4370–4379, 1972. (Cited on pages 40, 43, 45, 49, 53, 59 and 65.)
- [Kassab 2010] L Kassab, D da Silva and C de Araújo. *Influence of metallic nanoparticles on electric-dipole and magnetic-dipole transitions of Eu^{3+} doped germanate glasses*. *Journal of Applied Physics*, vol. 107, page 113506, 2010. (Cited on page 67.)
- [Khurgin 2009] J B Khurgin and G Sun. *Enhancement of optical properties of nanoscaled objects by metal nanoparticles*. *J. Opt. Soc. Am. B*, vol. 26, pages B83—B95, 2009. (Cited on pages 43, 46 and 54.)
- [Kim 1988] Young Sik Kim, Leung P T and George T F ;. *Classical decay rates for molecules in the presence of a spherical surface: a complete treatment*. *Surface science*, vol. 195, pages 1–14, 1988. (Cited on pages 52, 61 and 68.)
- [Kim 2008] Hyunmin Kim, Chengxiang Xiang, Aleix G Guñell, Reginald M Penner and Eric O Potma. *Tunable Two-Photon Excited Luminescence in Single Gold Nanowires Fabricated by Lithographically Patterned Nanowire Electrodeposition*. *The Journal of Physical Chemistry C*, vol. 112, no. 33, pages 12721–12727, 2008. (Cited on page 30.)
- [Kippenberg 2004] T. J. Kippenberg, S. M. Spillane and K. J. Vahala. *Demonstration of ultra-high- Q small mode volume toroid microcavities on a chip*.

- Applied Physics Letters, vol. 85, no. 25, page 6113, December 2004. (Cited on page 9.)
- [Kneipp 1997] K Kneipp, Y Wang, H Kneipp, I Itzkan, R R Dasary and M S Feld. *Single molecule detection using surface enhanced Raman scattering (SERS)*. vol. 78, page 1667, 1997. (Cited on page 14.)
- [Kneipp 1998] K Kneipp, H Kneipp, V B Kartha, and R. Manohran, G Deinum, I Itzkan, R R Dasary and M S Feld. *Detection and identification of a single DNA base molecule using surface enhanced Raman scattering (SERS)*. vol. 57, pages R6281—R6284, 1998. (Cited on page 14.)
- [Koenderink 2010] A F Koenderink. *On the use of Purcell factors for plasmon antennas*. Optics Letters, vol. 35, pages 4208–4210, 2010. (Cited on pages 47, 52 and 54.)
- [Kolwas 2009] K Kolwas, A Derkachova and M Shopa. *Size characteristics of surface plasmons and their manifestation in scattering properties of metal particles*. Journal of Quantitative Spectroscopy and Radiative Transfer, vol. 110, pages 1490–1501, 2009. (Cited on page 49.)
- [Kreiter 2002] M. Kreiter, M. Prummer, B. Hecht and U. P. Wild. *Orientation dependence of fluorescence lifetimes near an interface*. The Journal of Chemical Physics, vol. 117, no. 20, page 9430, 2002. (Cited on page 67.)
- [Kühn 2006] Sergei Kühn, Ulf Håkanson, Lavinia Rogobete and Vahid Sandoghdar. *Enhancement of Single-Molecule Fluorescence Using a Gold Nanoparticle as an Optical Nanoantenna*. Physical Review Letters, vol. 97, no. 1, page 17402, 2006. (Cited on pages 15 and 67.)
- [Kurtsiefer 2000] Christian Kurtsiefer, Sonja Mayer, Patrick Zarda and Harald Weinfurter. *Stable Solid-State Source of Single Photons*. Physical Review Letters, vol. 85, no. 2, pages 290–293, July 2000. (Cited on pages 81 and 84.)
- [Kuttge 2009] M Kuttge, E J R Vesseur and A Polman. *Fabry-Pérot resonators for surface plasmon polaritons probed by cathodoluminescence*. Applied Physics Letters, vol. 94, page 183104, 2009. (Cited on page 19.)
- [Lakowicz 2004] Joseph R Lakowicz. *Radiative decay engineering 3. Surface plasmon-coupled directional emission*. Analytical biochemistry, vol. 324, no. 2, pages 153–169, January 2004. (Cited on pages 12 and 13.)
- [Laurent 2005] S. Laurent, S. Varoutsis, L. Le Gratiet, A. Lematre, I. Sagnes, F. Raineri, A. Levenson, I. Robert-Philip and I. Abram. *Indistinguishable single photons from a single-quantum dot in a two-dimensional photonic crystal cavity*. Applied Physics Letters, vol. 87, no. 16, page 163107, October 2005. (Cited on page 9.)

- [Le Moal 2009] Eric Le Moal, Sandrine Lévêque-Fort, Marie-Claude Potier and Emmanuel Fort. *Nanoroughened plasmonic films for enhanced biosensing detection*. *Nanotechnology*, vol. 20, no. 22, page 225502, June 2009. (Cited on page 12.)
- [Lecamp 2007] G Lecamp. *Contrôle de l'émission spontanée et application aux microcavités*. PhD thesis, University Paris X I- Orsay, 2007. (Cited on page 54.)
- [Leray 2012] A Leray, C Spriet, D Trinel, Y Usson and L Héliot. *Generalization of the polar representation in time domain fluorescence lifetime imaging microscopy for biological applications: practical implementation*. *Journal of microscopy*, vol. 248, no. 1, pages 66–76, October 2012. (Cited on page 31.)
- [Lévêque 2006] G Lévêque and O J F Martin. *Optimization of finite diffraction gratings for the excitation of surface plasmons*. *Journal of Applied Physics*, vol. 100, no. 12, page 124301, 2006. (Cited on page 27.)
- [Liaw 2010] Jiunn-Woei Liaw, Chuan-Li Liu, Wei-Min Tu, Chieh-Sheng Sun and Mao-Kuen Kuo. *Average enhancement factor of molecules-doped coreshell (Ag@SiO₂) on fluorescence*. *Optics Express*, vol. 18, pages 12788–12797, 2010. (Cited on page 67.)
- [Liaw 2012] Jiunn-Woei Liaw and Hsiao-Yen Tsai. *Theoretical investigation of plasmonic enhancement of silica-coated gold nanorod on molecular fluorescence*. *Journal of Quantitative Spectroscopy and Radiative Transfer*, vol. 113, pages 470–479, 2012. (Cited on page 73.)
- [Lieb 2004] M A Lieb, J Zavislan and L Novotny. *Single-molecule orientations determined by direct emission pattern imaging*. vol. 21, pages 1210–1215, 2004. (Cited on page 67.)
- [Lu 2012] Yu-Jung Lu, Jisun Kim, Hung-Ying Chen, Chihhui Wu, Nima Dabidian, Charlotte E Sanders, Chun-Yuan Wang, Ming-Yen Lu, Bo-Hong Li, Xiang-gang Qiu, Wen-Hao Chang, Lih-Juann Chen, Gennady Shvets, Chih-Kang Shih and Shangjr Gwo. *Plasmonic nanolaser using epitaxially grown silver film*. *Science (New York, N.Y.)*, vol. 337, no. 6093, pages 450–3, July 2012. (Cited on page 16.)
- [Ma 2009] Zhi Ya Ma, Dosi Dosev and Ian M Kennedy. *A microemulsion preparation of nanoparticles of europium in silica with luminescence enhancement using silver*. *Nanotechnology*, vol. 20, no. 8, page 85608, 2009. (Cited on page 67.)
- [Maier 2006] S Maier. *Plasmonic field enhancement and SERS in the effective mode volume picture*. *Optics Express*, vol. 14, pages 1957–1964, 2006. (Cited on page 46.)
- [Mallek-Zouari 2010] I Mallek-Zouari, S Buil, X Quelin, B Mahler, B Dubertret and J.-P. Hermier. *Plasmon assisted single photon emission of CdSe/CdS*

- nanocrystals deposited on random gold film*. Applied Physics Letters, vol. 97, page 53109, 2010. (Cited on page 35.)
- [Marques 2007] Ana C. Marques and Rui M. Almeida. *Er photoluminescence enhancement in Ag-doped solgel planar waveguides*. Journal of Non-Crystalline Solids, vol. 353, no. 27, pages 2613–2618, August 2007. (Cited on page 67.)
- [Marty 2010] R Marty, A Arbouet, V Paillard, C Girard and G. Colas des Francs. *Photon antibunching in the optical near-field*. Physical Review B, vol. 82, page 081403(R), 2010. (Cited on pages 15, 77 and 78.)
- [Marty 2012] R Marty, C Girard, A Arbouet and G Colas des Francs. *Near-field coupling of a point-like dipolar source with a thin metallic film: Implication for STM plasmon excitations*. Chemical Physics Letters, vol. 532, no. 0, pages 100–105, 2012. (Cited on page 27.)
- [Meijer 2005] J. Meijer, B. Burchard, M. Domhan, C. Wittmann, T. Gaebel, I. Popa, F. Jelezko and J. Wrachtrup. *Generation of single color centers by focused nitrogen implantation*. Applied Physics Letters, vol. 87, no. 26, page 261909, December 2005. (Cited on page 80.)
- [Mertens 2006] H Mertens and A Polman. *Plasmon-enhanced erbium luminescence*. Applied Physics Letters, vol. 89, page 211107, 2006. (Cited on page 67.)
- [Mertens 2009] H Mertens and A Polman. *Strong luminescence quantum-efficiency enhancement near prolate metal nanoparticles: Dipolar versus higher-order modes*. Journal of applied physics, vol. 105, page 44302, 2009. (Cited on pages 62, 73 and 74.)
- [Mita 1996] Yoshimi Mita. *Change of absorption spectra in type-Ib diamond with heavy neutron irradiation*. Physical Review B, vol. 53, no. 17, pages 11360–11364, May 1996. (Cited on page 80.)
- [Mivelle 2010] M Mivelle, I A Ibrahim, F Baida, G W Burr, D Nedeljkovic, D Charraut, J-Y Rauch, R Salut and T Grosjean. *Bowtie nano-aperture as interface between near-fields and a single-mode fiber*. Optics express, vol. 18, no. 15, pages 15964–74, July 2010. (Cited on page 77.)
- [Mivelle 2012] Mathieu Mivelle, Thomas S van Zanten, Lars Neumann, Niek F van Hulst and Maria F Garcia-Parajo. *Ultrabright bowtie nanoaperture antenna probes studied by single molecule fluorescence*. Nano letters, vol. 12, no. 11, pages 5972–8, November 2012. (Cited on page 77.)
- [Moal 2007] E Le Moal, E Fort, S Lévêque-Fort, F P Cordelières, M-P Fontaine-Aupart and C Ricolleau. *Enhanced fluorescence cell imaging with metal-coated slides*. Biophysical journal, vol. 92, no. 6, pages 2150–61, March 2007. (Cited on page 12.)

- [Mochalin 2012] Vadym N Mochalin, Olga Shenderova, Dean Ho and Yury Gogotsi. *The properties and applications of nanodiamonds*. Nature nanotechnology, vol. 7, no. 1, pages 11–23, January 2012. (Cited on page 80.)
- [Moskovits 1985] M Moskovits. *Surface-enhanced Raman spectroscopy*. vol. 57, pages 783–826, 1985. (Cited on page 14.)
- [Neu 2012] Elke Neu, Mario Agio and Christoph Becher. *Photophysics of single silicon vacancy centers in diamond: implications for single photon emission*. Optics express, vol. 20, no. 18, pages 19956–71, August 2012. (Cited on page 77.)
- [Nie 1997] S Nie and S R Emory. *Probing Single Molecules and Single Nanoparticles by Surface Enhanced Raman Scattering*. Science, vol. 275, pages 1102–1106, 1997. (Cited on page 14.)
- [Noginov 2009] M A Noginov, G Zhu, A M Belgrave, R Bakker, V M Shalaev, E E Narimanov, S Stout, E Herz, T Suteewong and U Wiesner. *Demonstration of a spaser-based nanolaser*. Nature, vol. 460, pages 1110–1112, 2009. (Cited on pages 16 and 37.)
- [Novotny 2006] Lukas Novotny and Bert Hecht. *Principles of Nano-Optics*. Cambridge University Press, 2006. (Cited on pages 59, 78 and 79.)
- [Orrit 2002] Michel Orrit. *Photon statistics in single molecule experiments*. vol. 3, page 255, 2002. (Cited on page 78.)
- [Pic 2010] *8th European short Course on Principles and Applications of Time-Resolved Fluorescence Spectroscopy*. 2010. (Cited on page 30.)
- [Pillonnet 2012] A Pillonnet, A Berthelot, A Pereira, O Benamara, S Derom, G Colas des Francs and A-M. Jurdyc. *Coupling distance between Eu³⁺ emitters and Ag nanoparticles*. Applied Physics Letters, vol. 100, page 153115, 2012. (Cited on page 70.)
- [Prawer 2008] Steven Prawer and Andrew D Greentree. *Diamond for quantum computing*. Science (New York, N.Y.), vol. 320, no. 5883, pages 1601–2, June 2008. (Cited on page 80.)
- [Press 2007] David Press, Stephan Götzinger, Stephan Reitzenstein, Carolin Hoffmann, Andreas Löffler, Martin Kamp, Alfred Forchel and Yoshihisa Yamamoto. *Photon Antibunching from a Single Quantum-Dot-Microcavity System in the Strong Coupling Regime*. Phys. Rev. Lett., vol. 98, no. 11, page 117402, March 2007. (Cited on page 9.)
- [Protsenko 2005] I. Protsenko, A. Uskov, O. Zaimidoroga, V. Samoiloov and E. O'Reilly. *Dipole nanolaser*. Physical Review A, vol. 71, no. 6, page 063812, June 2005. (Cited on pages 16 and 37.)

- [Purcell 1946] E M Purcell. *Spontaneous Emission Probabilities at Radio Frequencies*. In Physical Review, editeur, Proceedings of the American Physical Society - Minutes of the Spring Meeting At Cambridge, April 25-27, volume 69, page 681, 1946. (Cited on page 3.)
- [Rabiei 2002] P. Rabiei, W.H. Steier and L.R. Dalton. *Polymer micro-ring filters and modulators*. Journal of Lightwave Technology, vol. 20, no. 11, pages 1968–1975, November 2002. (Cited on page 8.)
- [Raether 1988] H Raether. Surface Plasmons on Smooth and Rough Surfaces and on Gratings, volume 111 of *Springer Tracts in Modern Physics*. Springer, Berlin, 1988. (Cited on page 10.)
- [Reineck 2013] Philipp Reineck, Daniel Gómez, Soon Hock Ng, Matthias Karg, Toby Bell, Paul Mulvaney and Udo Bach. *Distance and Wavelength Dependent Quenching of Molecular Fluorescence by Au@SiO₂ Core-Shell Nanoparticles*. ACS nano, vol. 7, no. 8, pages 6636–48, August 2013. (Cited on page 57.)
- [Reithmaier 2004] J P Reithmaier, G Sek, A Löffler, C Hofmann, S Kuhn, S Reitzenstein, L V Keldysh, V D Kulakovskii, T L Reinecke and A Forchel. *Strong coupling in a single quantum dot-semiconductor microcavity system*. Nature, vol. 432, no. 7014, pages 197–200, November 2004. (Cited on page 9.)
- [Reitzenstein 2007] S. Reitzenstein, C. Hofmann, A. Gorbunov, M. Strauß, S. H. Kwon, C. Schneider, A. Löffler, S. Hofling, M. Kamp and A. Forchel. *AlAs-GaAs micropillar cavities with quality factors exceeding 150,000*. Applied Physics Letters, vol. 90, no. 25, page 251109, June 2007. (Cited on page 9.)
- [Rivera 2012] V.A.G. Rivera, Y. Ledemi, S.P.A. Osorio, D. Manzani, Y. Messaddeq, L.A.O. Nunes and E. Marega. *Efficient plasmonic coupling between Er³⁺:(Ag/Au) in tellurite glasses*. Journal of Non-Crystalline Solids, vol. 358, no. 2, pages 399–405, 2012. (Cited on page 67.)
- [Rolly 2011] Brice Rolly, Brian Stout, Sebastien Bidault and Nicolas Bonod. *Crucial role of the emitter particle distance on the directivity of optical antennas*. Optics Letters, vol. 36, pages 3368–3370, 2011. (Cited on page 15.)
- [Ruppin 1982] R Ruppin. *Decay of an excited molecule near a small sphere*. J. Chem. Phys., vol. 76, pages 1681–1684, 1982. (Cited on page 61.)
- [Santori 2002] Charles Santori, David Fattal, Jelena Vučković, Glenn S. Solomon and Yoshihisa Yamamoto. *Indistinguishable photons from a single-photon device*. Nature, vol. 419, no. 6907, pages 594–597, October 2002. (Cited on page 9.)
- [Sauvan 2013] C. Sauvan, J. P. Hugonin, I. S. Maksymov and P. Lalanne. *Theory of the Spontaneous Optical Emission of Nanosize Photonic and Plasmon Resonators*. Physical Review Letters, vol. 110, no. 23, page 237401, June 2013. (Cited on page 56.)

- [Savasta 2010] Salvatore Savasta, Rosalba Saija, Alessandro Ridolfo, Omar Di Stefano, Paolo Denti and Ferdinando Borghese. *Nanopolaritons: Vacuum Rabi Splitting with a Single Quantum Dot in the Center of a Dimer Nanoantenna*. ACS Nano, vol. 11, pages 6369–6376, 2010. (Cited on page 37.)
- [Schietinger 2009] Stefan Schietinger, Michael Barth, Thomas Aichele and Oliver Benson. *Plasmon-enhanced single photon emission from a nanoassembled metal-diamond hybrid structure at room temperature*. Nano letters, vol. 9, no. 4, pages 1694–1698, April 2009. (Cited on pages 15, 16 and 77.)
- [Shalaev 2007] V.M. Shalaev, S. Kawata, M.A. Noginov, G. Zhu and V.P. Drachev. *Surface plasmons and gain media*. In Nanophotonics with Surface Plasmons, chapitre 5, pages 141–169. 2007. (Cited on page 57.)
- [Sinzig 1994] J Sinzig and M Quinten. *Scattering and Absorption by Spherical Multilayer Particles*. Applied Physics A, vol. 58, pages 157–162, 1994. (Cited on page 68.)
- [Som 2011] Tirtha Som and Basudeb Karmakar. *Nano silver:antimony glass hybrid nanocomposites and their enhanced fluorescence application*. Solid State Sciences, vol. 13, no. 5, pages 887–895, May 2011. (Cited on page 67.)
- [Song 2005] Bong-Shik Song, Susumu Noda, Takashi Asano and Yoshihiro Akahane. *Ultra-high-Q photonic double-heterostructure nanocavity*. Nature Materials, vol. 4, no. 3, pages 207–210, February 2005. (Cited on pages 8 and 9.)
- [Sonnichsen 2002] C Sonnichsen and Others. *Drastic reduction of plasmon damping in gold nanorods*. vol. 89, page 77402, 2002. (Cited on page 41.)
- [Srinivasan 2003] Kartik Srinivasan, Paul E. Barclay, Oskar Painter, Jianxin Chen, Alfred Y. Cho and Claire Gmachl. *Experimental demonstration of a high quality factor photonic crystal microcavity*. Applied Physics Letters, vol. 83, no. 10, page 1915, September 2003. (Cited on page 8.)
- [Srinivasan 2004] Kartik Srinivasan, Paul Barclay, Matthew Borselli and Oskar Painter. *Optical-fiber-based measurement of an ultrasmall volume high-Q photonic crystal microcavity*. Physical Review B, vol. 70, no. 8, page 081306, August 2004. (Cited on page 9.)
- [Stefani 2007] Fernando D Stefani, Krasimir Vasilev, Noelia Bocchio, Frank Gaul, Andrea Pomozi and Maximilian Kreiter. *Photonic mode density effects on single-molecule fluorescence blinking*. New Journal of Physics, vol. 9, no. 2, pages 21–21, February 2007. (Cited on page 12.)
- [Steiner 2008] M Steiner, A Failla, A Hartschuh, F Schleifenbaum, C Stupperich and A Meixner. *Controlling molecular broadband-emission by optical confinement*. New Journal of Physics, vol. 10, page 123017, 2008. (Cited on page 28.)

- [Stockman 2010] Mark I Stockman. *The spaser as a nanoscale quantum generator and ultrafast amplifier*. *Journal of Optics*, vol. 12, page 024004 (13pp), 2010. (Cited on pages 16, 37, 48 and 56.)
- [Stout 2008] Brian Stout, J C Auger and Alexis Devilez. *Recursive T matrix algorithm for resonant multiple scattering: applications to localized plasmon excitations*. *J. Opt. Soc. Am. A*, vol. 25, pages 2549–2557, 2008. (Cited on page 68.)
- [Taminiau 2007] T H Taminiau, R J Moerland, F B Segerink, L Kuipers and N F van Hulst. *$\lambda/4$ resonance of an optical monopole antenna probed by single molecule fluorescence*. *Nano Lett.*, vol. 7, pages 28–33, 2007. (Cited on page 77.)
- [Tanabe 2007] Takasumi Tanabe, Akihiko Shinya, Eiichi Kuramochi, Shingo Kondo, Hideaki Taniyama and Masaya Notomi. *Single point defect photonic crystal nanocavity with ultrahigh quality factor achieved by using hexapole mode*. *Applied Physics Letters*, vol. 91, no. 2, page 021110, July 2007. (Cited on page 9.)
- [Tanaka 2008] Yoshinori Tanaka, Takashi Asano and Susumu Noda. *Design of Photonic Crystal Nanocavity With Q-Factor of 10^9* . *J. Lightwave Technol.*, vol. 26, no. 11, pages 1532–1539, 2008. (Cited on page 9.)
- [Thompson 2013] J D Thompson, T G Tiecke, N P de Leon, J Feist, A V Akimov, M Gullans, A S Zibrov, V Vuletić and M D Lukin. *Coupling a single trapped atom to a nanoscale optical cavity*. *Science (New York, N.Y.)*, vol. 340, no. 6137, pages 1202–5, June 2013. (Cited on page 77.)
- [Timmerman 2008] D. Timmerman, I. Izeddin, P. Stallinga, I. N. Yassievich and T. Gregorkiewicz. *Space-separated quantum cutting with silicon nanocrystals for photovoltaic applications*. *Nature Photonics*, vol. 2, no. 2, pages 105–109, January 2008. (Cited on page 74.)
- [Trügler 2008] Andreas Trügler and Ulrich Hohenester. *Strong coupling between a metallic nanoparticle and a single molecule*. *Physical Review B*, vol. 77, no. 11, page 115403, March 2008. (Cited on page 37.)
- [Vahala 2003] Kerry J Vahala. *Optical microcavities*. *Nature*, vol. 424, pages 839–846, 2003. (Cited on pages 8, 19 and 46.)
- [van Wijngaarden 2011] J. T. van Wijngaarden, M. M. van Schooneveld, C. de Mello Donegá and A. Meijerink. *Enhancement of the decay rate by plasmon coupling for Eu^{3+} in an Au nanoparticle model system*. *Europhysics Letters*, vol. 93, no. 5, page 57005, March 2011. (Cited on pages 67 and 71.)
- [Varoutsis 2005] S. Varoutsis, S. Laurent, P. Kramper, A. Lemaître, I. Sagnes, I. Robert-Philip and I. Abram. *Restoration of photon indistinguishability*

- in the emission of a semiconductor quantum dot.* Physical Review B, vol. 72, no. 4, page 041303, July 2005. (Cited on page 9.)
- [Vernooy 1998] D. W. Vernooy, V. S. Ilchenko, H. Mabuchi, E. W. Streed and H. J. Kimble. *High-Q measurements of fused-silica microspheres in the near infrared.* Optics Letters, vol. 23, no. 4, page 247, February 1998. (Cited on page 8.)
- [Vielma 2007] Jason Vielma and P T Leung. *Nonlocal optical effects on the fluorescence and decay rates for admolecules at a metallic nanoparticle.* The Journal of chemical physics, vol. 126, no. 19, page 194704, May 2007. (Cited on page 62.)
- [Wang 2008] Qingyan Wang, Jia Wang and Shulian Zhang. *A nano-confined source based on surface plasmon Bragg reflectors and nanocavity.* Optics Express, vol. 16, pages 19882–19890, 2008. (Cited on page 19.)
- [Wang 2011] Chao Wang, Huiquan Tao, Liang Cheng and Zhuang Liu. *Near-infrared light induced in vivo photodynamic therapy of cancer based on upconversion nanoparticles.* Biomaterials, vol. 32, no. 26, pages 6145–6154, 2011. (Cited on page 74.)
- [Weeber 2007a] J.-C. Weeber, a. Bouhelier, G. Colas des Francs, S. Massenot, J. Grandidier, L. Markey and a. Dereux. *Surface-plasmon hopping along coupled coplanar cavities.* Physical Review B, vol. 76, no. 11, page 113405, September 2007. (Cited on page 19.)
- [Weeber 2007b] J.-C. Weeber, A Bouhelier, G des Francs, L Markey and A Dereux. *Submicrometer In-Plane Integrated Surface Plasmon Cavities.* Nano Letters, vol. 7, no. 5, pages 1352–1359, 2007. (Cited on pages 19, 20, 26 and 28.)
- [Winter 2008] G Winter, W A Murray, S Wedge and W L Barnes. *Spontaneous emission from within a metal-clad cavity mediated by coupled surface plasmon-polaritons.* J. Phys.: Condens. Matter, vol. 20, page 304218, 2008. (Cited on page 20.)
- [Wokaun 1982] A Wokaun, J P Gordon and P F Liao. *Radiation Damping in Surface-Enhanced Raman Scattering.* Physical Review Letters, vol. 48, pages 957–960, 1982. (Cited on page 38.)
- [Worthing 2001] P T Worthing, J A E Wasey and W L Barnes. *Rate and efficiency of spontaneous emission in metal-clad microcavities.* Journal of Applied Physics, vol. 89, no. 1, pages 615–625, 2001. (Cited on pages 12, 28 and 29.)
- [Wrachtrup 2006] Jörg Wrachtrup and Fedor Jelezko. *Processing quantum information in diamond.* Journal of Physics: Condensed Matter, vol. 18, no. 21, pages S807–S824, May 2006. (Cited on page 80.)

-
- [Yablonovitch 1987] E Yablonovitch. *Inhibited Spontaneous Emission in Solid-State Physics and Electronics*. prl, vol. 58, page 2059, 1987. (Cited on page 4.)
- [Yokoyama 1992] H Yokoyama. *Physics and device applications of optical microcavities*. Science (New York, N.Y.), vol. 256, no. 5053, pages 66–70, April 1992. (Cited on page 8.)
- [Young 2009] A Young, C Y Hu, L Marseglia, J P Harrison, J L O’Brien and J G Rarity. *Cavity enhanced spin measurement of the ground state spin of an NV center in diamond*. New Journal of Physics, vol. 11, no. 1, page 013007, January 2009. (Cited on page 80.)
- [Zheng 2010] Dingwei Zheng. *Study and manipulation of photoluminescent NV color center in diamond*. October 2010. (Cited on pages 80 and 81.)